WAVE TRANSFORMATION AND ALONGSHORE SEDIMENT TRANSPORT DUE TO OBLIQUELY ORIENTED SHOREFACE-CONNECTED RIDGES

A Thesis
Presented to
The Academic Faculty

by

Tongtong Xu

In Partial Fulfillment
of the Requirements for the Degree
Master of Science in the
School of Civil and Environmental Engineering

Georgia Institute of Technology
December 2015

WAVE TRANSFORMATION AND ALONGSHORE SEDIMENT TRANSPORT DUE TO OBLIQUELY ORIENTED SHOREFACE-CONNECTED RIDGES

Approved by:

Dr. Kevin Haas, Advisor
School of Civil and Environmental Engineering
Georgia Institute of Technology

Dr. Jeffrey List
U.S. Geological Survey
Coastal and Marine Geology Program

Dr. Hermann Fritz
School of Civil and Environmental Engineering
Georgia Institute of Technology

Date Approved: December 11, 2015

ACKNOWLEDGEMENTS

The present work is funded by the United States Geological Survey Hurricane Sandy, Fire Island Physical Processes Study under project number 2006V38. I want to thank my advisor, Dr. Kevin Haas, for giving me the chance to join his research team, supporting me with my work, teaching me patiently, giving me advice in every aspect and for repeatedly reviewing my thesis. The past year has been a big change for me, and Dr. Haas understood me, believed me and gave me so many opportunities to improve myself and achieve what I want to accomplish in both my work and my life. I also thank my committee members, Dr. Jeffrey List and Dr. Hermann Fritz, for their advice on my thesis and the idea to improve my work. Thank you to Dr. Jeffrey List and Dr. Ilgar Safak for discussing my research monthly, sharing insights and keeping me organized to finally complete this work. Thank you to Dr. Xiufeng Yang for the preparation and background work before I joined this project.

Thank you to Donghua Cai for sharing information about tricks and useful tools in Matlab and in Linux language. Also, thank you and Runze Miao for all the time we spent together, classes we took and exams we prepared together. I thank my roommate, Wen Xu, for helping me through all the difficult time and for preparing dinner for me when I am busy. Thank you to my father and my mother, who have been very supportive of my choice, encouraging me and portraying a prosperous future that they believe I am capable of living.

TABLE OF CONTENTS

LIST OF FIGURES

SUMMARY

The inner continental shelf off the western half of the barrier island Fire Island, NY, is characterized by a series of obliquely oriented shoreface-connected ridges. The long-term historic shoreline record shows persistent undulations in shoreline shape at an alongshore scale similar to the alongshore scale of the ridges. This suggests that the ridges affect the wave transformation, alongshore sediment transport and corresponding shoreline change. These processes are investigated by utilizing the SWAN (Simulating WAves Nearshore) model, forced with realistic wave parameters, on a simplified, synthetic bathymetry replicating the scales of the shoreface-connected ridges. Results indicate that the relative magnitude of alongshore variations of modeled waves, alongshore transport, and the corresponding shoreline change are highly correlated with the relative orientation of the incoming waves to the ridges. Alongshore variations in both wave height and direction along the breaker line are much stronger when the predominant wave direction is along the main axis of the ridges rather than perpendicular to the ridge crests. This pattern of wave height variation is further explained by evaluating the directional energy spectrum and using a reverse ray-tracing technique. The gradients of the alongshore sediment transport, which lead to shoreline change, also appear to be stronger for waves with an angle of incidence similar to the ridge orientation. These results help explain the relationship between the oblique shoreface-connected ridges and the corresponding shoreline changes and shed light on the connection between the inner-shelf ridges and persistent shoreline undulations for the Western portion of Fire Island.

CHAPTER I

INTRODUCTION

Wave transformation is a dominant process in the nearshore zone that is affected by the bottom topography, characterized by friction, wave shoaling, refraction, diffraction and breaking. This process can be divided into two stages: a pre-breaking stage where the waves are propagating while steepening with nonlinear interactions outside the surf zone and a second process including a rather chaotic appearance during wave breaking turning into a turbulent bore within the surf zone (Beji and Battjes, 1993). During wave propagation, wave energy will focus or converge around headlands and deltas, and diverge or spread through bays and canyons (Buonaiuto Jr et al., 2011).

As waves dynamically interact with the complex topography, feedback from waves will profoundly modify the distribution of sediment transport and further influence the bathymetric evolution, long and short term shoreline change, and inlet migration. Due to these significant impacts on coastal morphology, accurate estimates of the spatial and temporal variability of wave parameters in the nearshore zone is critical and imperative for coastal engineering.

The characteristics, behaviors and mechanisms behind wave transformation have been studied under many scenarios. Most of them are conducted through experiments, numerical simulation and field studies of wave propagation over mild sloping bottom with submerged structures, such as an alongshore uniform bar. The focus of the present study is on the characteristics of wave transformation and patterns of sediment transport influenced by shoreface-connected ridges that extend offshore from the west coastline of Fire Island and orient obliquely to the shoreline.

1.1 Fire Island morphology

Fire Island, a 50-km-long barrier island located at the south shore of Long Island (Figure 1), New York and bounded by Fire Island Inlet to the west and Moriches Inlet to the east, acts as a natural barrier for the heavily populated mainland against storms, is an essential habitat for wildlife and is a well-known attraction for tourism and coastal communities. All of these functions are potentially under the threat of coastal erosion, which is a typical problem controlled by waves and currents along Fire Island. Thus, it is important to illustrate the historical Fire Island morphology and the connection to coastal erosion.

Previous studies reveal that Fire Island has migrated landward from a location near the present 18-m contour line over the past 8000 years (Leatherman, 1985; Schwab et al., 2000; Swift and Moslow, 1982; Williams, 1976). Classified by stability, the eastern section migrates a fairly large distance in the landward direction, the western section is a typical example of spit elongation, while the middle section between Point O'Woods and Watch Hill is relatively stable (Schwab et al., 2013). The sediment balance deficit between Moriches Inlet and Fire Island Inlet can be greater than $370,000\ m^3/y$ in the highest estimate (Hapke et al., 2010). Some suggest that the missing sediment transport comes from natural erosion along the shoreline or in the ebb-tidal deltas and ineffectiveness of the beach nourishment project (Kana, 1995; Kana et al., 2011; Rosati et al., 1999). However, others propose that the adjacent inner continental shelf actually acts as a sediment source during sediment transport processes (Batton, 2003; Hapke et al., 2010; McCormack and Toscano, 1981; Williams and Meisburger, 1987; Wolff, 1982). Regardless of the true mechanism, the situation of coastal erosion along Fire Island cannot be neglected.

All these previous studies have been concentrated on resolving sediment response to oceanographic and geologic processes, addressing the source of the imbalance and explaining the deficiency (Schwab et al., 2000, 2013). Some of these researchers

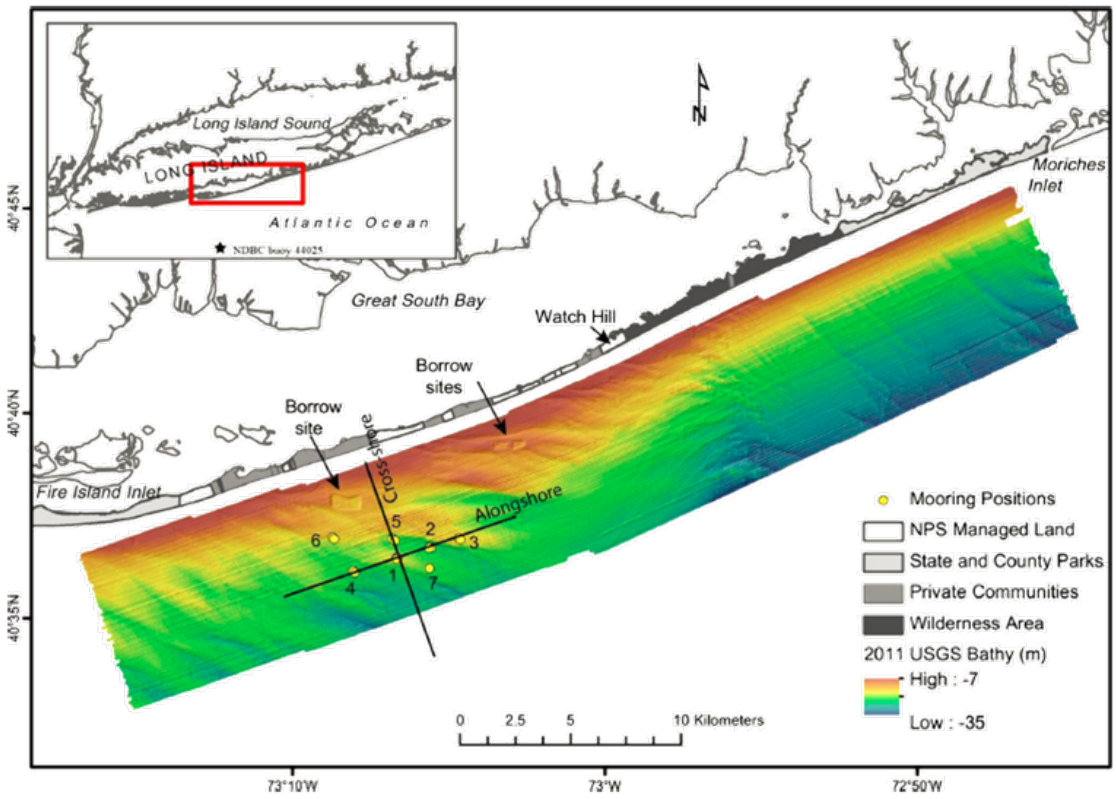

Figure 1: Site map of study area. Insert shows Long Island, NY, and location of NDBC buoy 44025. Main map identifies several features along Fire Island with color shading of recent bathymetry (Warner et al., 2014) showing the shoreface-attached ridges on the western side and a more planar shelf on the eastern side.

analyzed the morphology of a distinct feature in the inner-continental shelf of Fire Island-a set of ridges and troughs oriented roughly 60^o to the shore normal. Separated by Watch Hill, the inner continental shelf of Fire Island consists of a relatively steep gradient shelf east to the Watch Hill and a more gently sloping shelf to the west that is covered by a series of progressive thinning shoreface-connected sand ridges, which is developed and maintained by alongshore sediment transport from the outwash lobe of the Watch Hill over the past 300-500 years (Schwab et al., 2013). These ridges and troughs are spaced approximately every 2 to 3 km alongshore and occupy a total length about 14 km in the cross-shore direction with an average crest to trough height of 2 m relative to the bottom of bathymetry.

These obliquely-oriented shoreface-connected sand ridges have been under scrutiny

since the pioneer work conducted along Middle Atlantic Bight of the U.S. Atlantic shelf (Smith and Veatch, 1939). They exist sporatically from Long Island to Florida on North American Atlantic Shelf with maximum expression on the Delmarva peninsula (Swift et al., 1978). Such sand ridge topography is also exhibited in the adjacent continental shelf along the coast of Argentina, Uruguay, and Southern Brazil (Urien and Ewing, 1974), Guiana Shelf (Allersma, 1971), German Bight (Houbolt, 1968) and central Dutch coast (Van de Meene et al., 1996), Canadian Continental Shelf (Hoogendoorn and Dalrymple, 1986), etc.

Since the nearshore zone is usually under the most intense utilization of the sea floor, the features, formation and effect of the shoreface-connected ridges becomes a matter of increasing interest to coastal engineers. The first and most popular theory of their characteristics and evolution is documented by Duane et al. (1972), Swift et al. (1972) and Swift et al. (1978). They summarize attributes in common among these shoreface-connected ridges: (a) shoreline-oblique orientation, (b) angle opening into the direction of predominant storm flow, major tidal currents or wind-driven waves. Previously published hypotheses for the origin of sand ridges can be divided into two broad categories. The first is that the ridges are relict, pre-transgressive features and remnants of the Holocene transgression (McClennan and McMaster, 1971). The second is considered to be the so-called morphodynamic self-organization between shelf processes and hydraulic regime. As for the formation of sand ridges along Fire Island in particularly, a predominant theory illuminates the connection to the occurrences of strong storms and mixed-energy wave-driven currents. The maintenance mechanism, discussed by Warner et al. (2014), is generated by offshore deflected flows over ridge crests and onshore in the troughs.

For decades, researchers have been devoting effort to connecting the Fire Island shoreface-connected ridges to the shoreline response at the alongshore scale of these ridges. The decadal shoreline change from 1979 to 1994 (Allen and LaBash, 1997)

shows that the shoreline response in the western half of Fire Island has a distinctly longer length scale than the eastern half. However, Allen and LaBash (1997) did not link the distinctive pattern change to the shoreface-connected ridges. Instead, the reason they presented is related to a beach nourishment program. However, Schwab et al. (2000) noticed the potential link of the shoreline change to shoreface-connected ridges. They proposed that either the storm waves shoaling over sand ridges and focusing energy on certain segments of the shoreline or the interaction of sand ridges with some surf zone bars were the reason behind the distinct erosion and accretion pattern on the western half of Fire Island. Afterwards, Hapke et al. (2010) tested the a long time shoreline response of Fire Island, based on the hypothesis that patterns of shoreline change should maintain distinct spatial characteristics over long periods of time, if shoreline is affected by the shoreface-connected ridges. Although they concluded that the scale of the long time shoreline change is consistent (2-4km) with the alongshore length scale of the shoreface-connected ridges, their results showed no scale difference in shoreline change between the western and the eastern Fire Island. Thus, the relation of the shoreline change to the shoreface-connected ridges is not evident.

1.2 Wave-topography interaction

As stated in previous section, the wave-driven forcing is crucial in evaluating the evolution and maintenance of shoreface-connected ridge topography along Fire Island. However, the interaction between the wave field and topography is a two-way process.

Fire Island with its continental shelf and sand ridges is constantly affected and reshaped by hydrodynamic forces, such as regional wave fields generated by tropical storms and frequent intense midlatitude winter cyclones (Buonaiuto Jr et al., 2011). These systems usually result in heavy rain or snow with winds strong enough to produce a wave condition comparable to a hurricane. During the destructive tropical

superstorm event Hurricane Sandy (Blake et al., 2013), extensive storm surge inundated almost the entire Fire Island barrier system, leaving destroyed or washed-away houses, uncountable marine economic-related damage and severe population loss behind. Three places had been breached along Fire Island and one is still open as in 2015, modifying the barrier system abruptly. Besides the jeopardy in breaching, local wave setup along the coast induced by breaking waves can be upward of 20% of the deep water wave height, forcing additional water into the bays and elevating local sea level (Komar, 1998). In addition to the shoreline morphology changes, the complicated bathymetric system is formed with features like a series of obliquely-oriented shoreface-connected ridges that extend from the inner continental shelf to the surf zone.

In return, feedback from complex bed forms can also impact wave transformation, especially when waves propagate from deep water zones to intermediate, shallow water zones along with the increasing ratio of wave amplitude to water depth. Wave transformation over a simple alongshore uniform barred beach and over a large scale shoreface-connected ridges has been studied in many coastal engineering institutes for decades. These studies range from experimental to field and numerical aspects, devoted to discovering wave patterns and spectral variation when waves encounter submerged obstacles. Obstacles may be nearshore bars, reefs, breakwaters or as specific as a series of shoreface-connected ridges. Johnson et al. (1951) noted that energy was transmitted as a multiple crest system over natural reefs. After that, a large number of studies noted the generation of higher harmonics with shorter wave lengths (Dattatri et al., 1978; Drouin and Ouellet, 1988; Kojima et al., 1990) in different experimental setting. Beji and Battjes (1993) conducted a thorough investigation of the mechanism behind higher harmonics and revealed that the phenomena of deshoaling and wave decomposition take place in the deepening regions of the shoal. During wave propagation, the long waves gradually lose vertical symmetry, generate

a saw-toothed shape and break into waves with different wave lengths over the bar, while short waves evolve with increasing amplitudes, retaining vertical symmetry and a much milder wave decomposition. The existence of the uphill bar leads waves into breaking process and the deepening region helps preserve the higher harmonics. As for the energy spectrum, part of the energy from a typical narrow-banded frequency spectrum is transfered to higher frequencies, creating a rather broad spectrum. By performing tests for both breaking and non-breaking waves in monochromatic and irregular wave conditions, this paper also identifies the role of wave breaking as a secondary effect by merely re-scaling the wave spectrum through overall energy dissipation.

Field investigations (Byrne, 1969), on the other hand, presented visual observations of narrowband swell shoaling over a barred beach and the formation of secondary waves controlled by the wave height to water depth ratio. Elgar et al. (1997) ascribed the evolution of shoaling surface waves and its associated spectrum to variable depth, nonlinear interactions, reflection from the beach face and dissipation. Nonlinear interactions can be expressed as the relation between two primary wave components (in frequencies ω and wave number k) and excited secondary wave ($\omega_1+\omega_2=\omega_3, k_1+k_2=k_3$ or $\omega_1-\omega_2=\omega_3, k_1-k_2=k_3$). It is the nonlinear interaction that causes energy to be transferred into harmonic frequencies and generates a doubling in the number of wave crests. Masselink (1998) not only summarized the mechanisms behind the generation of secondary waves as the result of a highly nonlinear wave entering a less nonlinear environment, but also pointed out the so-called blue-shifting of the nearshore wave spectrum. After that, Sénéchal et al. (2002) found that role of wave breaking is weakening energy in primary waves and strengthening nonlinear coupling instead of simply redistributing energy among different frequencies as indicated in Beji and Battjes (1993)'s experiment. As for the effect of shoreface-connected ridges to wave transformation, the direct role of wave action (aside from currents generated by storm

or fair-weather waves) appears to have been entirely neglected in the literature (Hayes and Nairn, 2004). Warner et al. (2014) relates the shoreface-connected ridges to the consistent wind observations and analyzes the pattern of sediment transport through currents with a surface stress of 0.4 Pa.

Theoretically, the phenomenon of wave transformation caused by bottom variation has been explained using nonlinear equations for shallow water waves or a prototype of Boussinesq equation and its improved versions. Beginning from the 1960s, scientists have been devoted to developing numerical models for simulating the process of wave transformation using the Boussinesq equations (Abbott et al., 1973; Schaper and Sielke, 1984). After that, improvements for Boussinesq models have been made, such as the inclusion of improved dispersion characteristics (Witting, 1984) or additional third-order derivatives as compared to the conventional equations for flat bottom (Madsen et al., 1991) and mildly sloping bottom (Madsen and Sørensen, 1992). Using the technique suggested by Madsen and Sørensen (1992), Beji and Battjes (1994) carried out a numerical simulation in a wave flume with a sloping bottom and a submerged trapezoidal bar, which is the same as the experimental setting in Beji and Battjes (1993). The performance of the model has been tested and compared with measured data.

Nowadays, with the availability of high performance computation system, large numbers of studies concentrate on improving numerical methods with an ultimate goal to duplicate the natural wave propagation process. Okamoto et al. (2009) compared the performance of a multi-layered Boussinesq model and a Reynolds Averaged Navier-Stokes equation model on a bar-trough profile beach. Wave breaking in the former model is computed as an extra momentum term in the momentum equation. Thus, although the two models both show relatively good agreement with measurement results, the Boussinesq-based model failed to predict wave fields after wave breaking. Jabbari et al. (2013) utilized an improved Boussinesq-type model with

a finite element scheme, which is shown to be more efficient than finite difference methods. Also, this study aimed to and actually improved the nonlinearity and dispersion of waves shoaling on a constant slope beach and waves propagating over a barred beach, respectively. But the model is one dimensional, which does not allow it to predict wave propagation characteristics in the transverse direction. Furthermore, Christensen (1998) stated that shallow water and Boussinesq-based model is usually good at forecasting wave deformation due to shoaling but lack of accuracy in computing wave breaking. Thus, Kamath et al. (2015) validated the effectiveness of the three dimensional Computational Fluid Dynamics model REEF3D for wave transformation.

Vis-Star et al. (2007) studied the effect of a sloping bottom with a series of shoreface-connected ridges, accounting for the interaction between waves and the shoreface-connected ridges as the interactive terms between currents, waves and bed load. Although the research area is the shoreface-connected ridges along the Long Island, the seabed topography setting is different such that the bathymetry starts from a certain depth h_0 from the shoreline and, thus, the phenomenon of wave breaking does not appear in this situation. This paper identifies a significance convergence of wave rays at the upstream side of the ridges, which is due to bed form-induced wave refraction. Warner et al. (2014) utilizes the Regional Ocean Modeling System (ROMS) on a similar subject but focuses on the wind input and the interaction with the shoreface-connected ridges to the pattern of currents. They conclude that the alongshore flows driven by a surface stress westward develop an offshore-directed flow on the ridge crests and onshore in the troughs.

Overall, the interaction between wave transformation and bottom topography cannot be separated and together they dramatically affect the shoreline morphology. As indicated by Gravens (1999), shoreline undulations may be excited by specific environmental forcing conditions (waves from a particular direction) and their location

controlled by irregularities in the offshore bathymetry.

1.3 Spectral model comparison

All of the numerical models in the previous section resolve wave transformation in the nearshore zone with shallow water or Boussinesq equation system, which is computed via the time domain. Another significant branch of numerical simulation is spectral wave modeling through the frequency domain. Their respective generation levels can be divided into first, second, and more recently, third generation.

Starting from as early as the 1940's during World War II, wave forecasting was related to execution of military operations (CETN, 1994). At first, the model was based on statistical arguments, the significant wave method (Sverdrup and Munk, 1947). Further theoretical studies, mostly through the energy balance equation, revealed the role of significant wave height and period as indispensable in wave transformation. Pierson et al. (1955) revised the model into a spectral approach, which was the basis of spectral modeling for decades.

First-generation spectral models were developed successfully during 1960's, when the governing equation was the energy balance and the input could account for atmospheric input, nonlinear wave-wave interaction and frequency dissipation. Examples such as Ocean Data Gathering Program model (Cardone et al., 1975), the Spectral Ocean Wave Model (Pierson, 1982) or Global Spectral Ocean Wave Model (Clancy et al., 1986) are all first-generation spectral models. However, some of the terms were not properly represented. Dissipation was expressed as an assumed universal upper limit of the spectral densities and wave generation used simple empirical expressions (Booij et al., 1999). The effect of wave-wave interaction was overlooked or diminished, replaced by enhancing the wave growth (Ewing, 1971).

Second-generation models utilized a coupled linear system between atmospheric input and dissipation term, which explained energy transfer between frequency bands

and migration of spectral peak towards lower frequencies (CETN, 1994). The significance of nonlinear wave-wave interaction and the impact on wave spectrum were finally proven and accepted due to the solution of Boltzmann integrals (Hasselmann, 1962) and field experiment by Hasselmann et al. (1973). The relation between wind input and nonlinear wave-wave interaction could be summarized as the former one controlling energy transmission into the system, the latter one responsible for the exchange of energy in between the systems. Although second-generation models realized the dramatic effect from wave-wave interaction, these models could only parameterize these interactions (Young, 1988) instead of actually solving it. Another drawback of these models lay in the discrepancy in degrees of freedom between the energy input terms and the actual spectrum, which might lead to unrealistic spectral redistribution and make it necessary to select an appropriate limit for the spectrum in order to avoid this situation (Resio, 1993). Furthermore, these models contained empirical parameters, as many as five, which generated higher uncertainty to modeling results. Examples of second-generation models include Shallow-water wave (SHALWV) model (Hughes and Jensen, 1986) and Wave Information Studies (WIS) Wave Model (Hubertz, 1992).

In third-generation models, all processes are represented explicitly without a priori restrictions on the shape of the spectrum (Booij et al., 1999). They are defined discretely in the frequency or direction domain instead of formulated in a parametric or empirical framework. The degree of freedoms is consistent between input terms and the actual spectrum. Prior to the formulation of the first third-generation model, Hasselmann and Hasselmann (1985) developed the discrete interaction approximation (DIA) method to account for quadruplet wave-wave interactions, which is an explicit expression for nonlinear interactions. Using the whitecapping formulation by Komen et al. (1984), the problem is closed and waves driven by wind field propagating in the deep ocean can be well predicted. Examples include WAM (Group, 1988),

WAVEWATCH (Tolman, 1989) or Nedwam (Burgers, 1990), etc. Nevertheless, it is unrealistic to directly apply these third-generation models to coastal region, where processes like wave shoaling and breaking, triad wave-wave interactions are important but not included, and where computation is rather expensive due to high resolution requirements.

Simulating WAve Nearshore (SWAN) (Booij et al., 1999) is the first third-generation model designed for nearshore applications. This model not only incorporates features that are typical and dominant in deep water zones, such as wind input, nonlinear quadruplet wave-wave interaction, whitecapping and bottom friction, but also adds on processes like depth-induced breaking and nonlinear triad wave-wave interaction, which are indispensable in the nearshore zone. Furthermore, previous third-generation models implement explicit numerical schemes, which depends on Courant criterion for model stability. This is acceptable for wave modeling in the deep ocean, where the number of grid points is much less than in coastal region. In contrast, as waves are highly affected by rapidly varied bottom topography and by irregular shoreline morphology in nearshore region, the grid size and time steps have to be much smaller in order to satisfy the stability criterion. Thus, one of the most significant advances in SWAN is the removal of Courant stability criterion and implementation of implicit numerical schemes. After that, models like WAVEWATCH III (Van der Westhuysen and Tolman, 2011) and WWM II (Roland, 2008) have also been improved and adapted with implicit numerical schemes.

Nowadays, improvements of SWAN or other third-generation models have been continuously concentrated on increasing accuracy of refraction/diffraction computation (Lin, 2013). Studies apply different models to compare the performance and sensitivity regarding different coastal regions (Mortlock et al., 2014), to identify the effect of wave-topography interaction (Belibassakis et al., 2013) or to understand the connection between wave energy and beach morphologic change (Eshleman et al.,

2007). The objective of this thesis is to implement the SWAN model in order to study the specific type of wave-topography interaction: the connection between wave transformation and shoreface-connected ridges.

1.4 Outline of the pesent work

As stated in the previous sections, although the effect of a submerged bar in experimental tanks or in natural nearshore has been observed, analyzed and simulated numerically for decades, the majority of these studies focus on the effect of alongshore uniform bars to wave transformation. In reality, the nearshore bottom topography is much more complicated and features like a series of obliquely-oriented shoreface-connected ridges are rather typical and common along coastlines. The aim of the present study is to develop a better understanding of the effect of shoreface-connected ridges on wave transformation and the corresponding shoreline response driven by the associated alongshore sediment transport on a synthetic bathymetry similar to Fire Island while neglecting all other processes such as wind, tides and cross-shore transport.

In Chapter 2, the model setup is presented, including the model formulation in SWAN explaining the physical mechanism behind the action balance equation and different forcing terms, the development and verification of synthetic Fire Island bathymetry, numerical scheme comparison between regular and curvilinear grid, spectrum resolution improvement, approach of running SWAN and the associated boundary conditions. The choice of chosen wave parameters is evaluated by analysis of wave buoy data.

In Chapter 3 the effect of the ridges on wave transformation is studied. Contents consist of quantifying the wave field for different wave directions relative to the orientation of ridges, identifying the dominant mechanism, analyzing the energy spectrum and wave rays and finalizing the connection to wave breaking properties.

In Chapter 4 the alongshore sediment transport and shoreline change is presented by utilizing the CERC and GENESIS equations and continuity equation governing shoreline change through the alongshore gradient of sediment transport. Also, the relation between alongshore sediment transport and ridge orientation is investigated.

In Chapter 5 the sensitivity analysis focuses on the model performance and distribution changes in wave properties using different wave parameters along the southern boundary or different directional spreading. All previous model runs exclude bottom friction. Thus, the effect of bottom friction is identified by running an additional set of model runs including bottom friction.

The final chapter summarizes the work presented and provides the conclusions drawn from the study.

CHAPTER II

MODEL SETUP

Wave transformation is complex due to the combination of all the physical processes involved, even when using the convenient and effective SWAN model. Therefore, in order to understand how each process and the combined effect is implemented in SWAN, a brief introduction of the SWAN model formulation is presented in the first section. This project concentrates on identifying the effect of shoreface-connected ridges on wave transformation and the corresponding shoreline response. A feasible synthetic bathymetry replicating Fire Island is generated and verified in the second section. This is followed by a description of the scheme implementation including the procedure of running SWAN, evaluation of the spectral resolution and finally identification of energy leakage for extreme angles. Last, the wave parameters from hourly buoy data from National Data Buoy Center (NDBC) near Long Island is analyzed for their frequency of occurrence and used to determine the range of wave parameters in the numerical simulation.

2.1 Model formulation in SWAN

SWAN is a third-generation model developed by the Delft University of Technology to compute wave propagation in both time and space, shoaling, refraction due to current and depth, diffraction, reflection, wave generation by wind, nonlinear wave-wave interactions, whitecapping, depth- and steepness-induced breaking. Unlike traditional wave ray models, SWAN formulates the wave evolution in terms of a spectral energy balance, which is free of any priori limitations and represented explicitly in a discrete spectral formulation for all relevant physical processes. It is one of the most widely used and flexible wave refraction models, with the ability to be nested with

global-scale wave models or driven by offshore wave observations (Booij et al., 1999, 2000).

2.1.1 Action balance equation

In SWAN, wave properties are combined and stored in the wave energy density $E(\sigma, \theta)$, distributing wave energy over frequencies σ and propagation directions θ (the direction normal to the wave crest of each spectral component) (Booij et al., 2000). But the evolution of wave spectra is described by action density $N(\vec{x}, t; \sigma, \theta)$ in space $\vec{x}$ and time t. This is due to the capability of conservation in $N = E/\sigma$ during propagation in the presence of current, whereas energy density E is not conserved.

The evolution of the action density N is governed by the action balance equation as follows (e.g. Hasselmann et al. (1973)):

$$\frac{\partial}{\partial t}N + \frac{\partial}{\partial x}(C_x N) + \frac{\partial}{\partial y}(C_y N) + \frac{\partial}{\partial \sigma}(C_\sigma N) + \frac{\partial}{\partial \theta}(C_\theta N) = \frac{S_{tot}}{\sigma}, \tag{1}$$

where C_x, C_y, C_σ and C_θ are the wave propagation velocities in x, y, σ, θ space, respectively; S_{tot} is the source/sink term. The first term on the left-hand side represents the time rate of change of the action density. The second and third terms denote the propagation of wave energy in two-dimensional geographical space. The fourth term corresponds to the effect of the shifting of the radian frequency due to variations in depth and mean currents. The fifth term represents depth-induced and current-induced refraction. The term on the right hand side represents all physical processes which generate, dissipate, or redistribute wave energy. In shallow water, six processes contribute to S_{tot}:

$$S_{tot} = S_{wind} + S_{nl4} + S_{nl3} + S_{wcap} + S_{bot} + S_{wb}. \tag{2}$$

These terms denote, (S_{wind}) wave growth by the wind, nonlinear transfer of wave energy through (S_{nls}) three-wave and (S_{nl4}) four-wave interactions and wave decay due to (S_{wcap}) whitecapping, (S_{bot}) bottom friction and (S_{wb}) depth-induced wave breaking, which will be explained in greater detail in the following section.

2.1.2 Forcing terms

2.1.2.1 Wind input (S_{wind})

Wind input is incorporated based on a resonance mechanism (Phillips, 1957) and a feed-back mechanism (Miles, 1957). It is described as the sum of linear and exponential growth:

$$S_{wind}(\sigma, \theta) = A + BE(\sigma, \theta), \tag{3}$$

in which A and B depend on wave frequency and its direction and wind speed and direction. The linear growth term A eliminates wave growth at frequencies lower than the Pierson-Moskowitz frequency through a filter developed by Tolman (1992). The exponential growth term B can be expressed by two different methods: Komen et al. (1984) and Janssen (1989). In this thesis, this term is not included.

2.1.2.2 Quadruplet interaction (S_{nl4})

Quadruplet interaction is important for spectral evolution in the deep ocean, which causes energy transfer from the spectral peak to lower and to higher frequencies. The latter part of energy will eventually be dissipated due to whitecapping. Discovered by Phillips (1960) and Hasselmann (1962), waves exchange energy among resonant frequencies, which makes the computation accounting for this effect feasible.

The first method in SWAN is the Discrete Interaction Approximation (DIA) of Hasselmann and Hasselmann (1985). This method is effective in developing a wave spectrum but not valid for uni-directional waves. The second method is called XNL (van Vledder and Bottema, 2002), which calculates the Boltzmann integral precisely with the same prototype by Resio et al. (2001). In SWAN, quadruplet is automatically activated when SWAN runs in third generation mode (GEN3). Thus, quadruplet forcing is included in this thesis.

2.1.2.3 Triad interaction (S_{nl3})

In shallow water, triad interaction dominates energy transfer from lower frequency to higher frequency, causing the higher harmonics in the spectrum and wave height time series (Beji and Battjes, 1993). Experimental, field and numerical studies have been conducted regarding the triad interaction or wave transformation over a submerged bar as introduced in the previous chapter. SWAN utilizes the Lumped Triad Approximation (LTA) from Eldeberky (1996) to account for this three-wave interaction. In this thesis, this term is not activated.

2.1.2.4 Whitecapping (S_{wcap})

Whitecapping, primarily controlled by the steepness of waves, is expressed by the pulse-based model of Hasselmann (1974) and reformulated using the wave number instead of frequency as

$$S_{wcap}(\sigma,\theta) = -\Gamma\tilde{\sigma}\frac{k}{\tilde{k}}E(\sigma,\theta), \tag{4}$$

in which $\tilde{\sigma}$ and $\tilde{k}$ represent mean frequency and mean wave number. Γ is a coefficient describing the overall wave steepness. Since Γ is related to wind input and two formulations are listed for wind input, two expressions for Γ are necessary: Komen et al. (1984) and Janssen (1991). An alternative approach for representing whitecapping is a saturation-based model developed by Van der Westhuysen (2007). In this thesis, this term is not activated.

2.1.2.5 Bottom friction (S_{bot})

When waves propagate in shallow water, the orbital motions of water particles can reach to the bottom, which induces the interaction between wave and topography. The dominant mechanism of wave-bottom interaction is bottom friction represented as

$$S_{bot} = -C_b\frac{\sigma^2}{g^2\sinh^2 kd}E(\sigma,\theta), \tag{5}$$

where C_b is a bottom friction coefficient. Although the majority of studies accept this formulation, their conclusions differ in the expression of C_b. Hasselmann et al. (1973) suggested to use a constant as 0.038 m^2/s^3 in order to match with his experiments for JONSWAP spectrum. Bouws and Komen (1983) rederived the energy balance equation through deep-water dissipation and came up with 0.067 m^2/s^3 for wind sea in the North Sea. Collins (1972) and Madsen et al. (1988) both have a different expression for C_b. These four methods are all available in SWAN. In this thesis, this term is mostly unactivated except for the sensitivity analysis in Chapter 5.

2.1.2.6 Depth-induced wave breaking (S_{wb})

When waves propagate closer to the shoreline, the wave height increases due to shoaling while the water depth decreases, which makes the ratio of wave height over water depth increasing until it finally reaches a limit, leading to an instability, wave breaking and rapid energy dissipation. However, direct computation of energy dissipation due to wave breaking is not available. Eldeberky and Battjes (1995) came up with a bore-based model based on Battjes and Janssen (1978), which accounts for this effect by multiplying the ratio of the mean rate of energy dissipation due to wave breaking over the total energy dissipation with energy density

$$S_{wb}(\sigma,\theta) = \frac{D_{tot}}{E_{tot}} E(\sigma,\theta), \tag{6}$$

in which E_{tot} is the total wave energy and D_{tot} is the rate of depth-induced wave-breaking energy dissipation. An alternative model developed by Thornton et al. (1983) is also available, which is a replacement of Battjes and Janssen (1978)'s model to account for D_{tot}. In the model, Battjes and Janssen (1978)'s model is included.

2.2 Bathymetry generation and verification

As indicated in Chapter 1 and shown in Figure 1, the continental shelf of Fire Island is separated by the Watch Hill, with a series of obliquely-oriented shoreface-connected

ridges to the west and a rather steep gradient shelf to the east. In Figure 2 (a) the rectangle with a white edge color marks the area of interest, which corresponds to the relatively stable section of shoreline where the nearshore seabed contains shoreface-connected ridges. This is the prototype for constructing an idealized bathymetry with the obliquely-oriented repeated ridges. With a 12^o rotation in the clockwise direction, the shoreline of the study area becomes reasonably horizontal (Figure 2 (b)). The enlarged study area has a dimension of 30 km in the alongshore (y) direction and 15 km in the cross-shore (x) direction. From now on, the offshore direction is negative; 0 km in the cross-shore direction denotes the location of shoreline; distance offshore is negative from the shoreline. The angle of shore normal waves is 0^o, with negative values from the southeast direction and positive values from the southwest direction. Thus, the ridges angle in the study area orients nearly -60^o from shore normal.

In order to quantify the wave transformation due to the shoreface-connected ridges, a synthetic bathymetry of Fire Island which catches the major features of these ridges and the average slope is presented in Figure 2 (c). A bathymetry with five troughs is constructed with an alongshore trough to trough wavelength of 4 km. Thus, the ridge field in the alongshore direction begins from a ridge to a trough and ends with a ridge, with 6 ridges and 5 troughs in total. Considering y' as the distance starting from the left of the ridge field in the alongshore direction, the alongshore variation of the ridge field is expressed as

$$z_1 = A_r \sin(\frac{2\pi}{L_r} y'), \tag{7}$$

in which A_r denotes the ridge amplitude and L_r represents the ridge wave length.

Considering the total length of the ridge field in the cross-shore direction as b and the distance starting from the south of the ridge field as x', the variation along the length of the ridge field is calculated by a symmetric hyperbolic tangent function (a

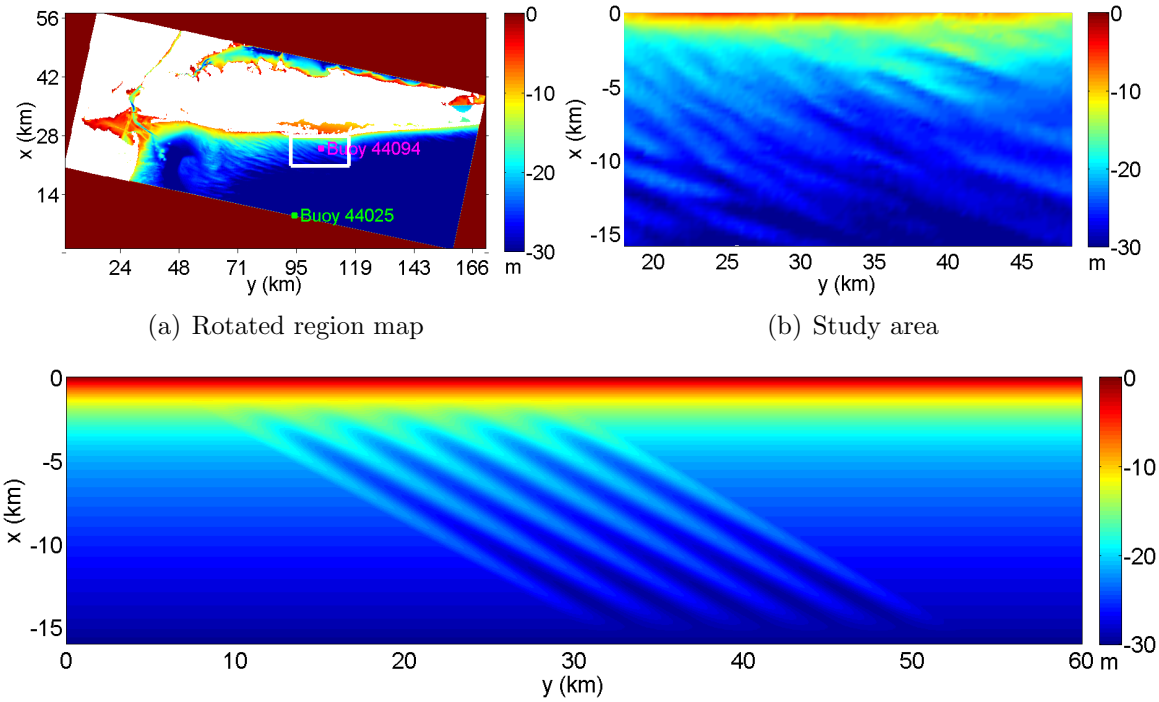

(a) Rotated region map

(b) Study area

(c) Synthetic bathymetry

Figure 2: (a) The seabed topography map of the Atlantic ocean near Long Island rotated by 12^o clockwise. The region of interest is marked by a rectangle with a white edge color. (b) Seabed topography for the study area extracted from the rectangle in the rotated region map and enlarged. (c) Synthetic seabed topography of the study area.

piecewise function):

$$z_2 = \begin{cases} \tanh^2\left(\frac{8.4}{b} \cdot x'\right), & \text{if } 0 \le x' \le \frac{5}{12}b; \\ 1, & \text{if } \frac{5}{12}b < x' < \frac{7}{12}b; \\ \tanh^2\left((b - x') \cdot \frac{8.4}{b}\right), & \text{if } \frac{7}{12}b \le x' \le b. \end{cases} \tag{8}$$

This is designed to smooth the beginning and ending of the ridge field along the long axis of the ridges. It represents a beginning of ridge field at x = -15.5 km and an ending at x = -1.1 km allowing for a uniform offshore boundary, and ends when the bottom depth is -9 m, which is generally offshore of the location for wave breaking. Moreover, ridges are rotated 60^o in the counterclockwise direction and scaled to 2 m for the ridge amplitude, A_r. The ridge width $L_r/2$ in the alongshore direction is 2 km, and the dimension of this synthetic bathymetry is 60 km in the alongshore direction

and 16 km in the cross-shore direction. The reason for extending the dimension in the alongshore direction is to avoid the significant east and west boundary effect, which will reduces wave heights dramatically for regions near these boundaries.

To further justify the reasonableness of this synthetic Fire Island, it is beneficial to compare the synthetic profile with the natural bathymetry for their ridge angles, the average slope and the magnitude of ridges in individual cross-sections. In Figure 3, the residual ridges are computed by subtracting the alongshore mean from the natural topography. The magenta lines specify angles of -60^o. The maximum magnitude of the ridges or troughs is 4 m. And most importantly, the angle of -60^o is reasonably consistent with the orientation of the natural ridge field and acceptable within $\pm 10^o$ deviation from the natural ridges.

Figure 4 (a) presents the alongshore mean bathymetry of the natural and the synthetic Fire Island. In general, the alongshore averaged natural profile is well reproduced by the alongshore mean synthetic profile. The synthetic profile from -1 to 0 km is extended until it reaches to bottom depth of 0 m.

Figure 4 (b) shows the cross-shore variation of the alongshore standard deviation (STD) for the natural and the synthetic bathymetry. The alongshore STD of the natural bathymetry varies from 0.8 to 2 m, with the stronger fluctuation located closer to the offshore boundary or shoreline boundaries. This larger peak in STD is the result of other coastal features not related to the ridges. In order to avoid the underestimation of alongshore STD for the synthetic bathymetry, these values are calculated within the ridge field only. As a result, the synthetic STD share a similar magnitude with the natural bathymetry. Near the south boundary, the variation of ridges are set to be smoothly decreased to 0 in order to maintain a uniform boundary condition. Close to the shoreline, it is also necessary to keep a uniform bathymetry in the surf zone in order to investigate the effect of ridges to wave transformation without the interference from a varying depth.

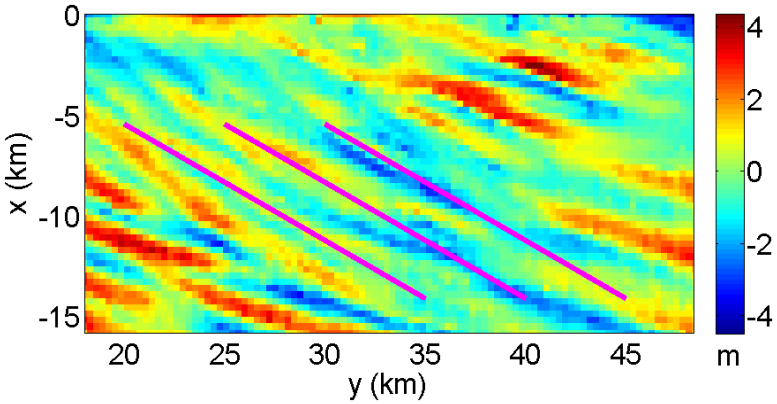

Figure 3: Residual ridges of the study area computed by subtracting the alongshore mean depth from the natural topography. Magenta represents straight lines with an angle of -60^o.

In Figure 4 (c)-(f), the alongshore sections at different cross-shore locations are shown for both the natural and the synthetic bathymetry. On one hand, the magnitude of the synthetic ridges is similar to the natural ones for these four individual alongshore sections, which justifies the usage of 2 m as the amplitude of synthetic ridges and the cross-shore decrease of magnitude close to the shoreline or the offshore boundary. The synthetic ridge width of 2 km in the alongshore direction is also shown to be a reasonable choice, especially in the middle zone as indicated by subplots (d) and (e) of Figure 4.

In summary, the synthetic bathymetry is a reasonable representation of the natural bathymetry in Fire Island.

2.3 Model approach

To reduce the lateral boundary shadow effect along with the associated drop in wave height, and since the periodic boundary condition is only available for a uniform grid, the procedure for running SWAN is divided into two separate simulations. As shown in Figure 5 (a), the first simulation utilizes the bathymetry without the ridge field, which is specified with a regular grid using a periodic boundary condition on the east and the west open boundaries, uniform wave conditions on the south open boundary

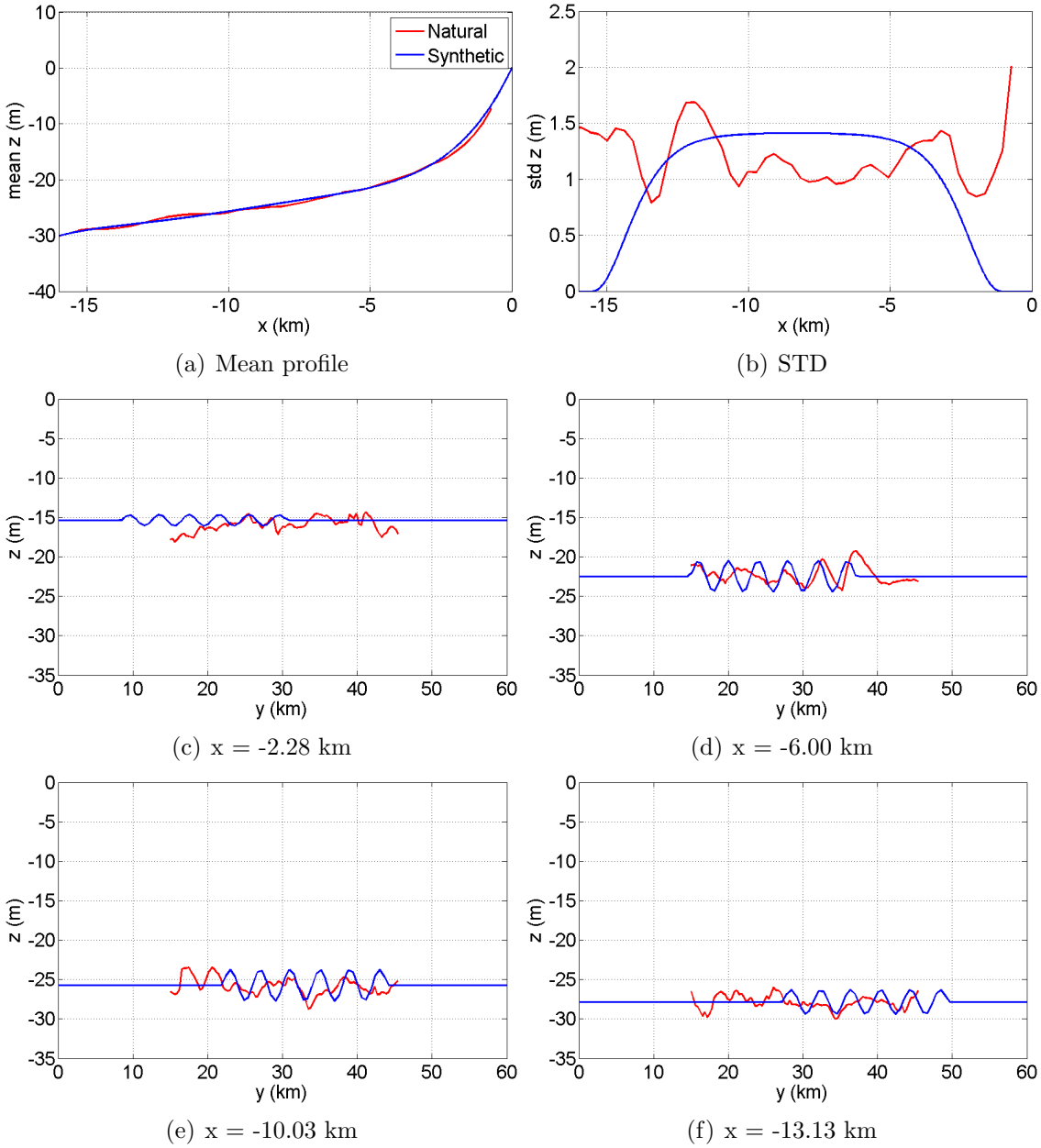

(a) Mean profile

(b) STD

(c) x = -2.28 km

(d) x = -6.00 km

(e) x = -10.03 km

(f) x = -13.13 km

Figure 4: Bathymetry validation through the comparison of (a) alongshore averaged profile; (b) alongshore standard deviation; (c)-(f) different alongshore sections of natural bathymetry (red) and synthetic bathymetry (blue).

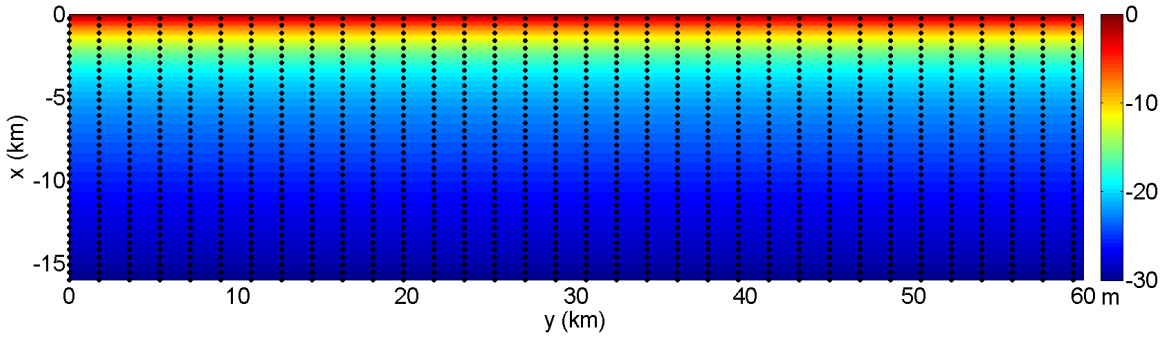

(a) Bathymetry without ridge field by regular grid

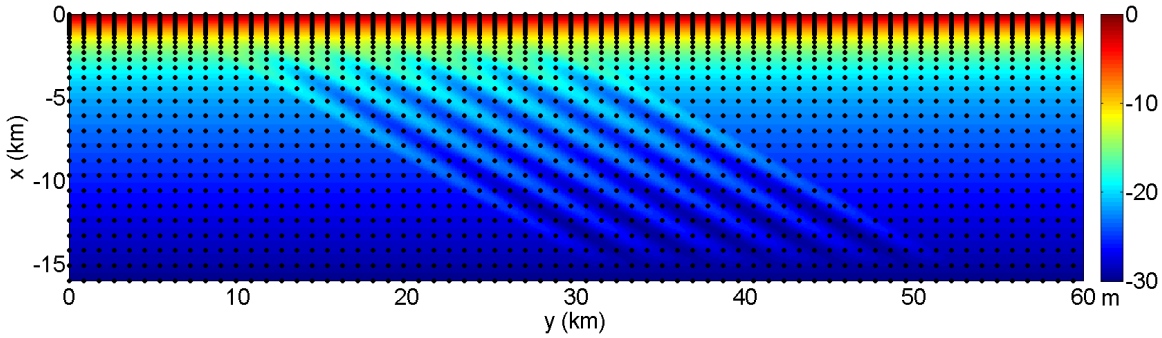

(b) Bathymetry with ridge field by nonuniform grid

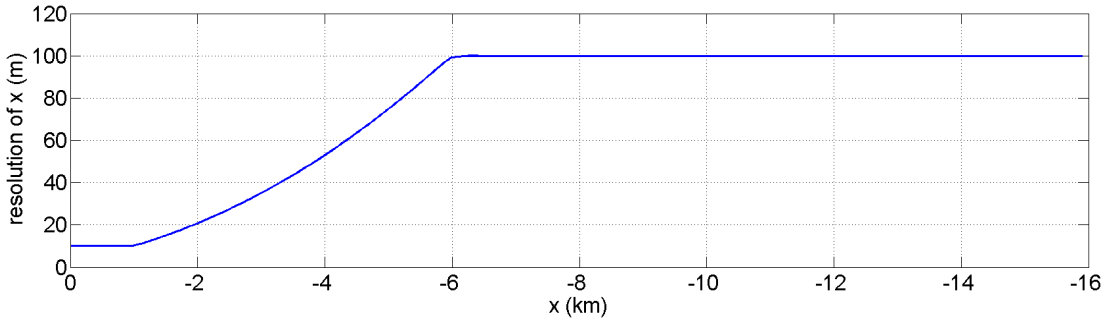

(c) Cross-shore resolution of nonuniform grid

Figure 5: Method for running SWAN. (a) The first SWAN run using bathymetry without ridge field with regular grid. (b) The second SWAN run using bathymetry with ridge field with nonuniform grid. Distance between each grid point is exaggerated for the purpose of presentation. (c) Cross-shore resolution of nonuniform grid.

and no flow condition along the shoreline. The grid spacing is 200 m in the alongshore direction and 50 m in the cross-shore direction, which makes the total number of grid points $301 \times 321 = 96621$. The objective of this SWAN run is to generate the output containing the energy spectra along the four boundary sections.

The output of energy spectrum along the four boundary lines from the first simulation is applied as an input of the second simulation. Figure 5 (b) shows the synthetic bathymetry including ridge field with a nonuniform grid scheme. The resolution of the nonuniform grid is 100 m (601 points) in the alongshore direction, but varies in the cross-shore direction and can be divided into 3 regions as shown in Figure 5 (c): a) in the first 1 km from the shoreline, grid spacing is 10 m uniformly; b) in the intermediate region from 1 to 6 km offshore, grid step smoothly increases from 10 to 100 m; c) from 6 km offshore to 16 km at the south boundary, grid resolution remains as a constant equal to 100 m. Wave breaking causes rapid wave transformation over short distances requiring the high resolution set for the nearshore 1 km. To use a uniform 10 m on a regular grid requires 1601 grid points just along the cross-shore direction and $1601 \times 601 = 962,201$ points in total. However, implementing this nonuniform grid uses just 308 points in the cross-shore direction and $308 \times 601 = 185,108$ points in total. Thus, the nonuniform grid can save substantial computation time. In the alongshore direction, the constant grid spacing of 100 m is enough for capturing variations due to ridges in the alongshore direction, since the alongshore ridge wave length is 2 km.

In summary, the numerical simulation for each condition is completed by first using the regular grid for the bathymetry without the ridge field. The east and west boundaries are subject to the periodic boundary condition, whereas the south boundary has constant wave parameters. Then the second SWAN run is computed using the nonuniform grid for the bathymetry with the ridge field using the boundary conditions from the first run.

Since SWAN calculates wave transformation on the basis of the energy spectrum and the related wave properties are normally quantified as mean or peak values derived from the energy spectrum, it is also important to ensure a sufficient resolution while maintaining computational speed for the energy spectrum. To assess the effect of

spectral resolution, Figure 6 compares the default resolution with a higher resolution used in this thesis. The default setting for spectral resolution is 21 bins for frequencies from 0.04 to 1 Hz and 36 bins for directions from 0 to 360 degree. But improved setting are used for spectral resolution as 32 bins for frequencies from 0.04 to 0.45 Hz and as 120 bins for directions from 0 to 360 degree. Using the default setting, the resolution of directional spectrum is too coarse such that the sharp transition between each angle is seen. In contrast, the directional spectrum using the improved setting is smoother and slightly narrower, with higher double peaks centered around -20^o and -60^o. In the frequency spectrum, the default setting extends the frequency distribution up to 1 Hz, although there is no energy in the higher frequency band from 0.5 Hz to 1 Hz. Thus, this part is cut off and a higher resolution is used to form the improved frequency spectrum. As a result, the peak energy becomes higher. Overall, the resolution in directional space is improved from 10 to 3 degree and the frequency spectrum has a higher resolution with a focus on the lower half frequency band from 0.04 to 0.45 Hz.

One noticeable error for these SWAN simulations is an energy leakage problem for larger incoming wave angles causing an associated decrease in wave properties. For example in Figure 7 (a), the mean incoming wave angle on the offshore boundary is -60^o. However, as waves propagate 200 m (2 grid points) forward, part of the energy related to the larger wave directions from -100^o to -80^o is lost. In this thesis, a larger wave angle refers to more oblique and a smaller wave angle refers to more shore normal. This is because the energy associated with wave angles greater than -90^o on the boundary will not enter the domain, causing the energy leakage problem. If the mean incoming wave direction at the south boundary is set to be a large angle, greater energy will be contained in these extreme angles so that this effect becomes significant.

As shown in Figure 7 (b), in order to diagnose the threshold of energy leakage

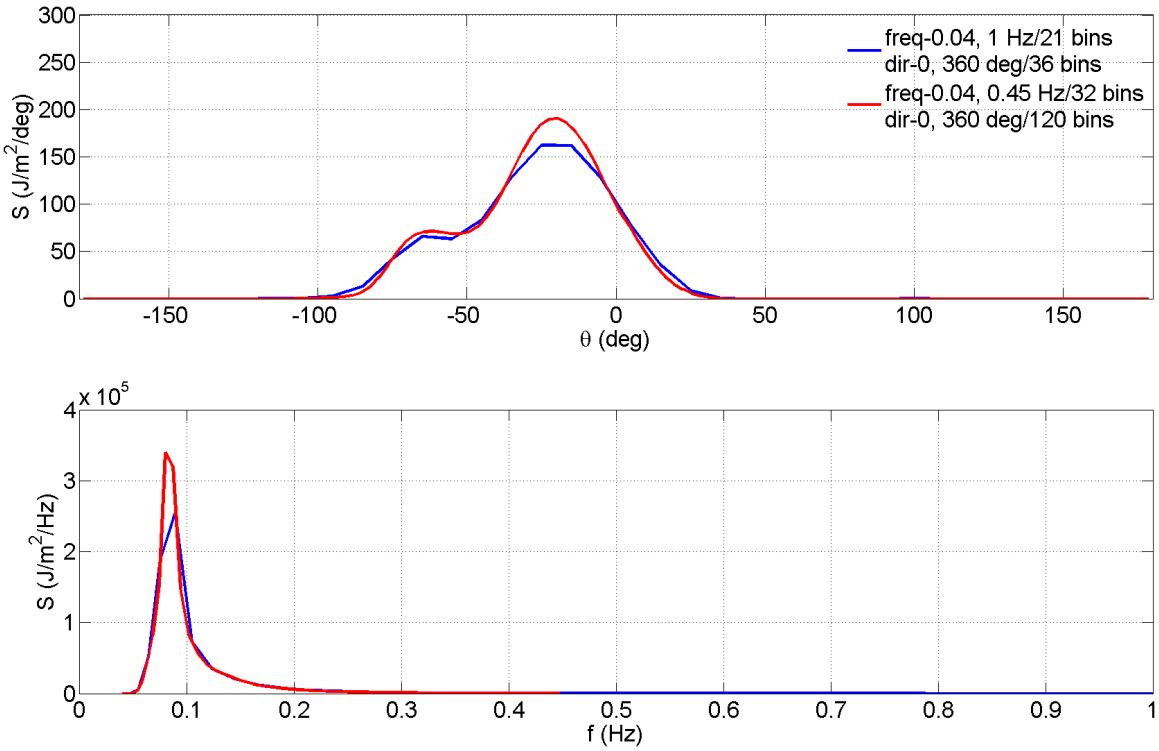

Figure 6: Directional spectra (top) and frequency spectra (bottom) at x = -5 km, y = 30 km with different directional and frequency range and resolution. Incoming wave direction is -30^o.

effect, a range of mean incoming wave angles from -80^o to 45^o is applied in SWAN. The wave height on the south boundary is used to determine the impact range of this effect, since the wave height is set to be a constant of 4 m in the south boundary condition. In other words, if the wave height at the south boundary drops off from 4 m, wave properties are under the influence of this leakage effect. Evidently, the threshold is $\pm 35^o$. Thus, within $\pm 35^o$, the wave properties are independent of leakage effect. Beyond that, wave heights are decreasing with greater angles. As a result, when comparing cases with different incoming wave angles, this effect is considered and a normalization process is used to diminish the variation caused by leakage.

2.4 Selection of wave conditions

In order to identify the proper range of wave parameters, it is beneficial to analyze the wave observations collected by the National Data Buoy Center (NDBC). Measurement

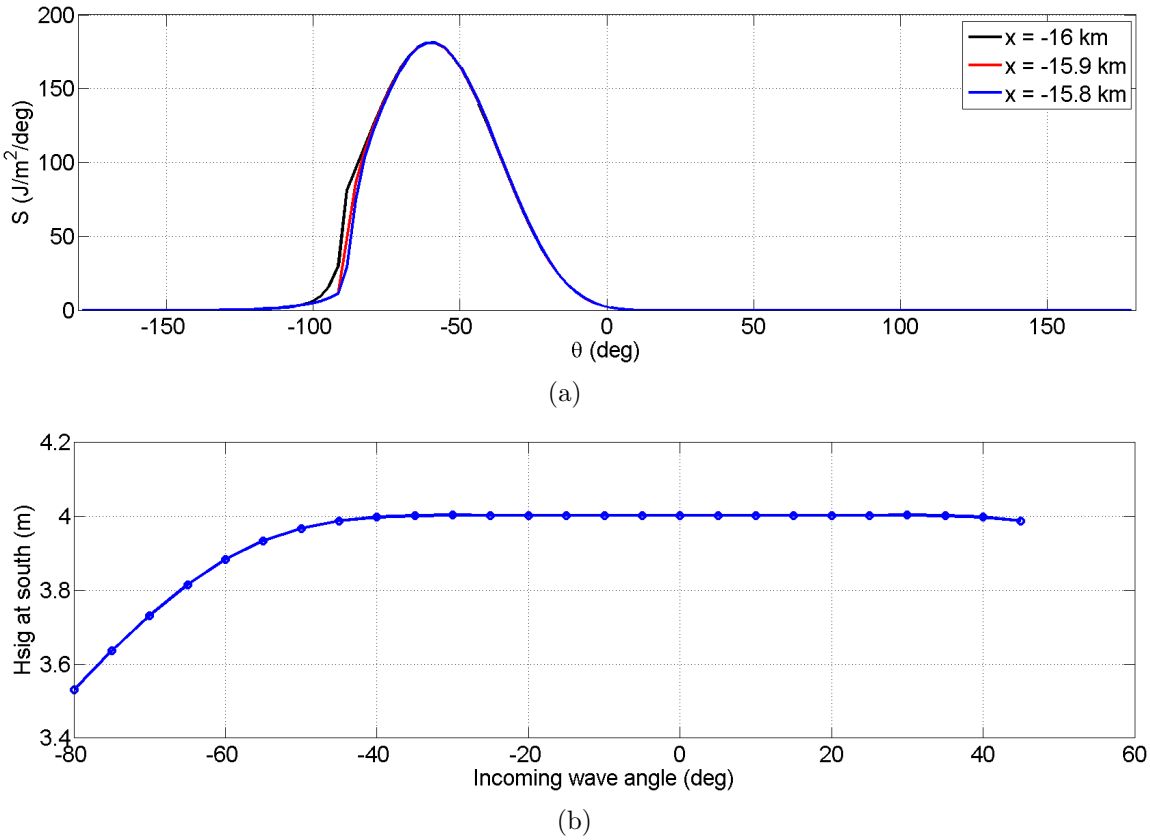

Figure 7: Energy leakage problem. (a) Directional spectrum near south boundary showing the energy leakage within 200 m from the south along the middle line (y = 30 km). The mean incoming wave direction is -60^o. (b) Significant wave heights on the south boundary versus mean incoming wave angles.

locations include nearshore regions (Station 44094 located at 40.59 N, 73.11 W) and intermediate coastal waters (Station 44025 located at 40.25 N, 73.17 W) off the south shore of Fire Island Inlet. Locations of the buoy stations are marked in terms of the Cartesian coordinate in Figure 2.

Station 44094 is a waverider buoy in water depth of 25 m. This buoy has been installed by the USGS in February 2014 and the standard meteorological data start was collected every 30 minutes, updated and submitted monthly by Scripps Institution of Oceanography. The standard meteorological data consist of significant wave height as the average of the highest one-third of all wave heights during 30-min measurement period, dominant wave period with the maximum wave energy, average wave period

during 30-min measurement period, wave direction associated with dominant wave period and sea surface temperature.

Station 44025, which is owned and maintained by NDBC, is a 3-meter discus buoy in 40.8-m depth. Hourly observations have been recorded since October 1975, with a 10-year gap from October 1980 to March 1991. Measurements include standard meteorological data, continuous wind data, spectral wave density data and various ocean observations. Although it is the longest and most reliable record of wave measurements in the Fire Island region, its location is beyond the water-depth range of the study area, which begins at 30 m.

For the convenience of comparing data collections from two stations, Snell's Law is applied to transfer waves from 41-m depth to 25-m depth and the wave-trapped condition is analyzed for offshore-directed waves, which may refract back on shore. Based on Snell's Law, wave direction at one location is evaluated as

$$\frac{\sin\theta}{C} = \frac{\sin\theta_1}{C_1}, \tag{9}$$

where C is the wave celerity and θ is the wave direction. Subscript 1 denotes the location with 25-m water depth. The wave number k is solved from dispersion,

$$\sigma^2 = gk\tanh kh, \tag{10}$$

in which σ is the wave frequency, h is the bottom depth, and the wave celerity C is found as,

$$C = \frac{\sigma}{k}. \tag{11}$$

For all onshore directed wave directions within -90^o to 90^o, it is easy to solve the transfered directions at 25-m depth,

$$\theta_1 = \arcsin\left(\frac{\sin\theta}{C}C_1\right). \tag{12}$$

For offshore directed wave directions within 90^o to 180^o or -90^o to -180^o, waves need to be filtered for wave-trapped condition, where the offshore directed waves will either turn back onshore or escape to deep water.

To evaluate if a wave is trapped, first given the wave period, the wave length in deep water (L_0) is

$$L_0 = \frac{g}{2\pi} T^2. \tag{13}$$

Subscript 0 denotes deep-water properties. The wave number and the wave celerity in deep water are then found as

$$k_0 = \frac{2\pi}{L_0}, \tag{14}$$

$$C_0 = \frac{\omega}{k_0}. \tag{15}$$

If the following statement is true, waves are trapped:

$$\frac{\sin\theta}{C} C_0 > 1. \tag{16}$$

Thus, trapped waves have a new wave angle at the water depth of 40.8 m, as

$$\theta_2 = \begin{cases} 180^o - \theta, & \text{if } \theta > 90^o; \\ -(180^o + \theta), & \text{if } \theta < -90^o. \end{cases} \tag{17}$$

The wave direction at 25-m water depth is computed as

$$\theta_1 = \arcsin\left(\frac{\sin\theta_2}{C} C_1\right). \tag{18}$$

As shown in Figure 8, the polar plot combines information from wave height, wave direction and wave period to a single figure. Based on Figure 8 (a), wave directions cover a large range from -100^o to 60^o. For waves in the negative (from the southeast) directions, wave periods range from as short as 4 s to as long as 16 s. The most rare and highest waves and the most frequently occurring waves all fall in the negative directions. The largest waves happen at -60^o and -30^o with a wave height of 3.9 m and both are around 10-s period. For waves in the positive (northeast) directions, waves are shorter in both height and period. The average wave height is 1 m and the periods cover from 3 to 6 s.

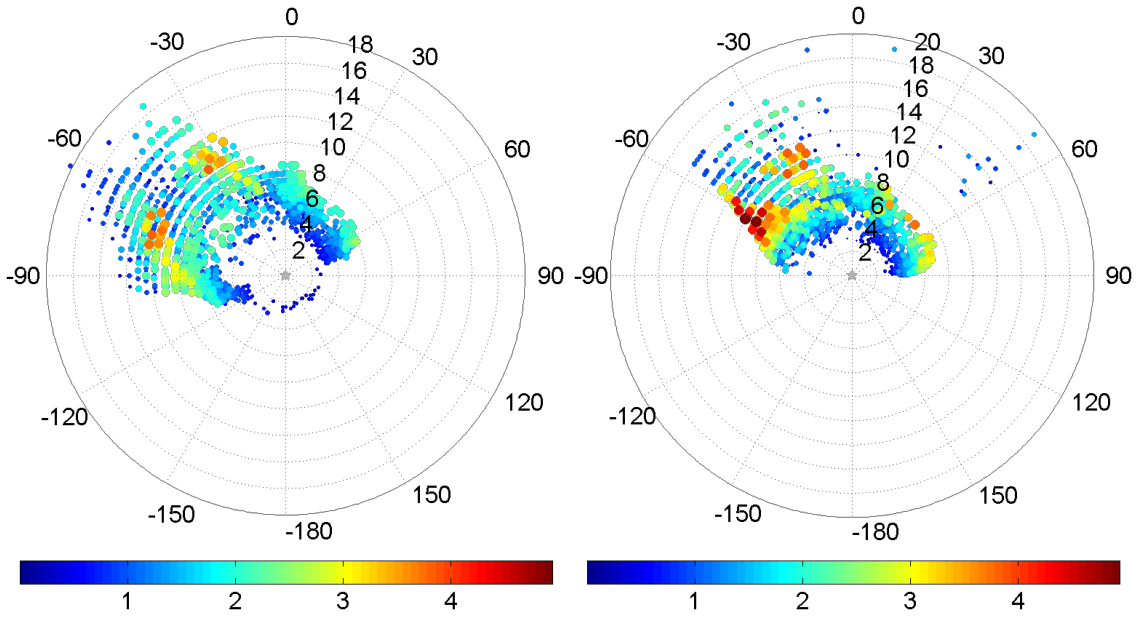

(a) Buoy 44094 (b) Buoy 44025

Figure 8: Scatter polar plot using hourly NDBC (a) buoy 44094 and (b) buoy 44025 data transfered to 25-m water depth from September to December, 2014. Wave direction is relative to shore normal, radius represent wave periods, colors and sizes denote wave heights.

Based on Figure 8 (b), wave directions cover from -60^o to 80^o. Due to Snell's Law and the trapped waves effect, waves with angle greater than -60^o and longer than 10 s have been refracted closer to shore normal. The overall shape is consistent with Figure 8 (a), only with stronger wave conditions. Although the highest wave height is still centered around -60^o and -30^o, the period range is longer from 6 to 11 s and the wave height is higher.

As stated in the previous section, wave properties at the south boundary are selected as input in SWAN. In chapter 3, these parameters are chosen such that the wave height is 4 m, the wave period is 12 s, the directional spread is 20^o and the incoming wave angles vary from -60^o, -30^o, 0^o to 30^o. In chapter 4 and chapter 5, the same wave conditions are used as in chapter 3, except that the incoming wave angles vary from -68^o to 44^o. Another set of wave conditions tested in chapter 5 is 2-m wave height, 9-s period, and the incoming wave angles varying from -68^o to 44^o.

CHAPTER III

EFFECT OF RIDGES ON WAVE TRANSFORMATION

This chapter contains the numerical simulation results and related analysis consisting of description of the general wave field, identification of the dominant mechanisms affecting the behaviors of the wave propagation through the ridges, explanation of ridge-induced phenomena by wave energy spectra analysis and the relation to wave breaking properties. The test case illustrated here is for wave parameters at the south boundary with significant wave height fixed to 4 m, peak wave period 12 s and directional spread as $\pm 20^o$. The angle of the ridges in this chapter is -30^o such that the incoming wave angles can cover a relatively large range on both sides of the ridge. As indicated from the previous chapter, when the mean incoming wave direction is more oblique than $\pm 35^o$, energy leakage causes wave heights to drop and wave directions to be far less oblique within 200 m from south boundary. That is to say, if the mean incoming wave direction is -80^o, that incoming angle will decrease to -68^o within 200 m. In this case, the actual incoming angle shall be -68^o. If the ridge orientation is -60^o, which is the ridge angle relative to the shoreline for Fire Island, not much variation can be captured and analyzed for incoming waves more oblique than the ridge orientation.

3.1 General Wave Field

The wave height variation in the entire simulated domain is plotted in Figure 9, with mean incoming wave direction, θ at the south boundary (a) $\theta = -30^o$, (b) $\theta = 30^o$. The negative or positive angles suggest waves are coming from southeast or southwest, respectively as shown by the arrows. As shown in this figure, the wave height stays relatively large as the waves propagate from the offshore boundary until shallow water

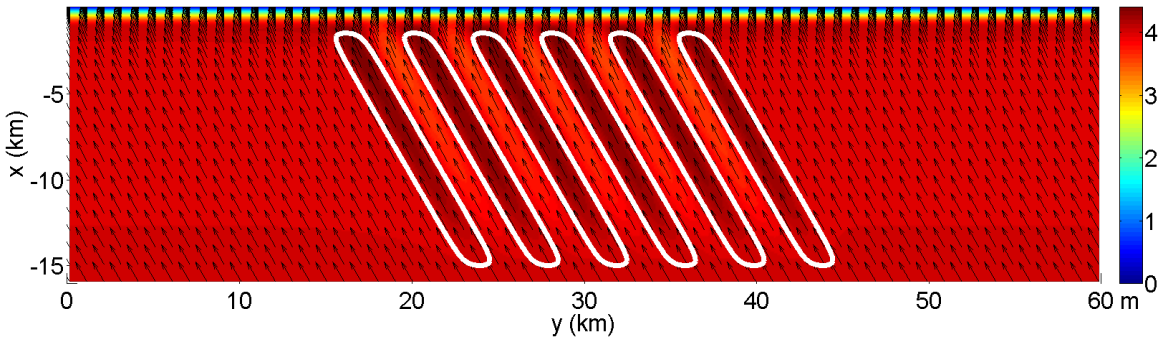

(a) $\theta = -30^o$

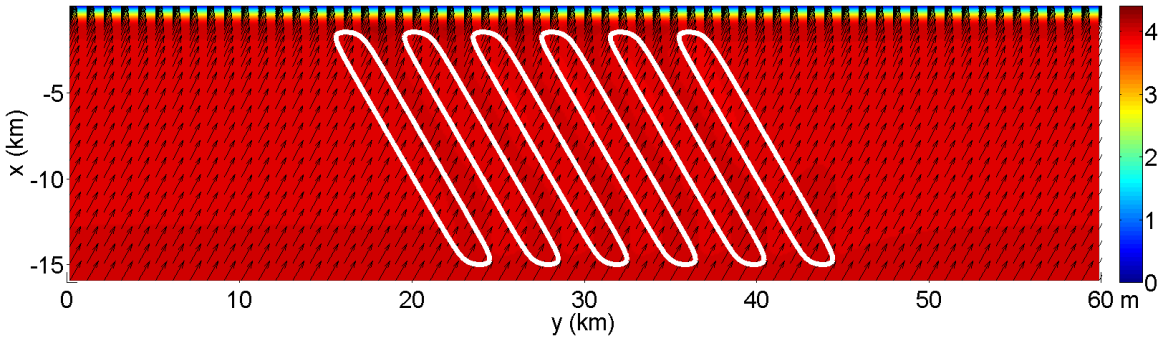

(b) $\theta = 30^o$

Figure 9: Wave heights in color plot with wave directions as quivers. White contours are the outline of ridges. Mean incoming wave angles are (a) $\theta = -30^o$ and (b) $\theta = 30^o$.

where the waves break. After that, the wave height drops from 4 m to 0 m at the shoreline, which appears to be a narrow band on the top. Comparing wave coming from southeast (-30^o) versus southwest (30^o), (i.e. along or relatively perpendicular to the orientation of ridges), the wave height variation is much stronger for waves along the ridges.

This type of comparison is more obvious, when alongshore or cross-shore sections are extracted and plotted on the same figure for $\pm 30^o$ incoming wave angles (Figures 10 and 11). Figure 10 shows the alongshore section of bottom elevation, wave height and wave direction 4 km away from the shoreline. At this particular alongshore section, the average depth is near 20 m with the ridge amplitude equal to 1.8 m. The wave height fluctuation is centered around 3.9 m for both incoming wave angles. However, the magnitude of the fluctuation can be as large as 0.7 m when the waves

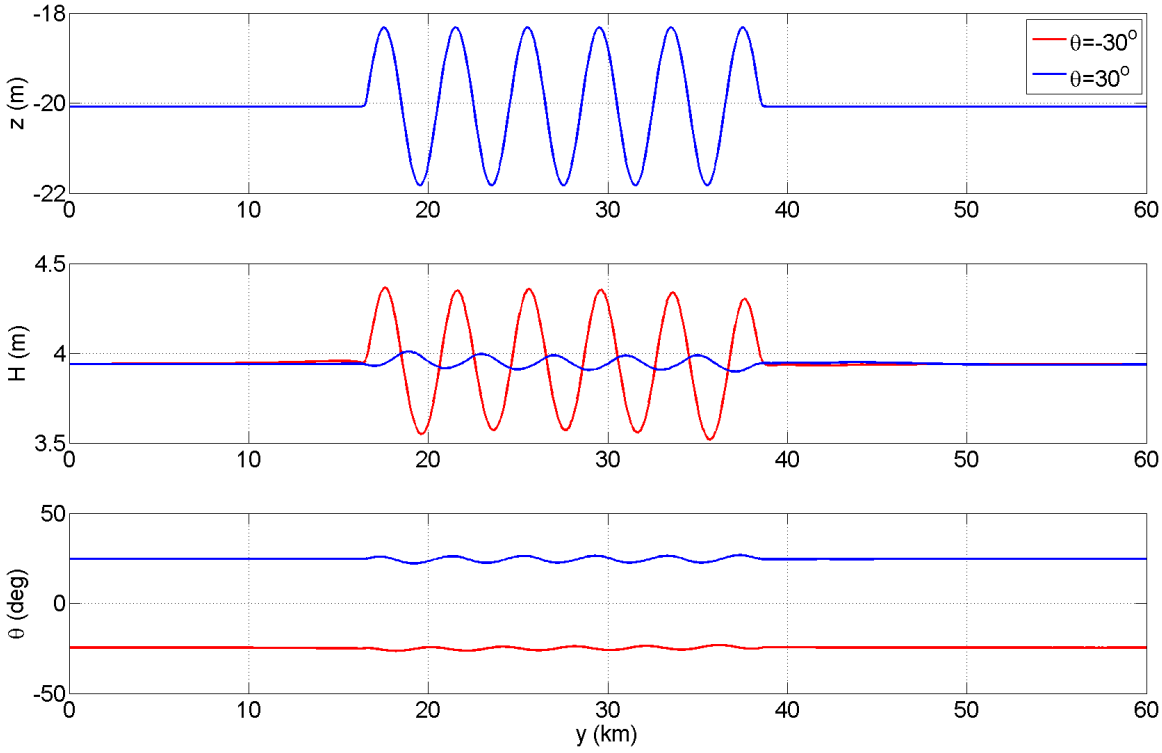

Figure 10: Alongshore sections at x = -4 km for different mean incoming wave angles of (a) bottom elevation, (b) wave height and (c) wave direction.

come along the ridges (-30^o), whereas this variation is only 0.2 m when the waves come from a direction that is more perpendicular to ridges (30^o). This is due to the relatively larger gradients along the wave crests in bottom topography for waves coming down the ridges and, thus, larger modification in the wave heights as wave directions change due to refraction. However, for $\theta = -30^o$, the largest wave height happens on the crest of the ridge field, while it appears to be closer to the right hand side of the ridges for $\theta = 30^o$. The wave direction variation has a similarly small range for both cases, which is explained later in this chapter.

The cross-shore variation in the middle line of the domain of wave height and angle is shown in Figure 11, which displays larger variation of wave height but similar wave direction change for incoming wave angle, $\theta = -30^o$, compared to $\theta = 30^o$. Generally, wave height begins as 4 m as specified by the south boundary condition, fluctuates and increases due to the shoaling effect and the lack of bottom friction,

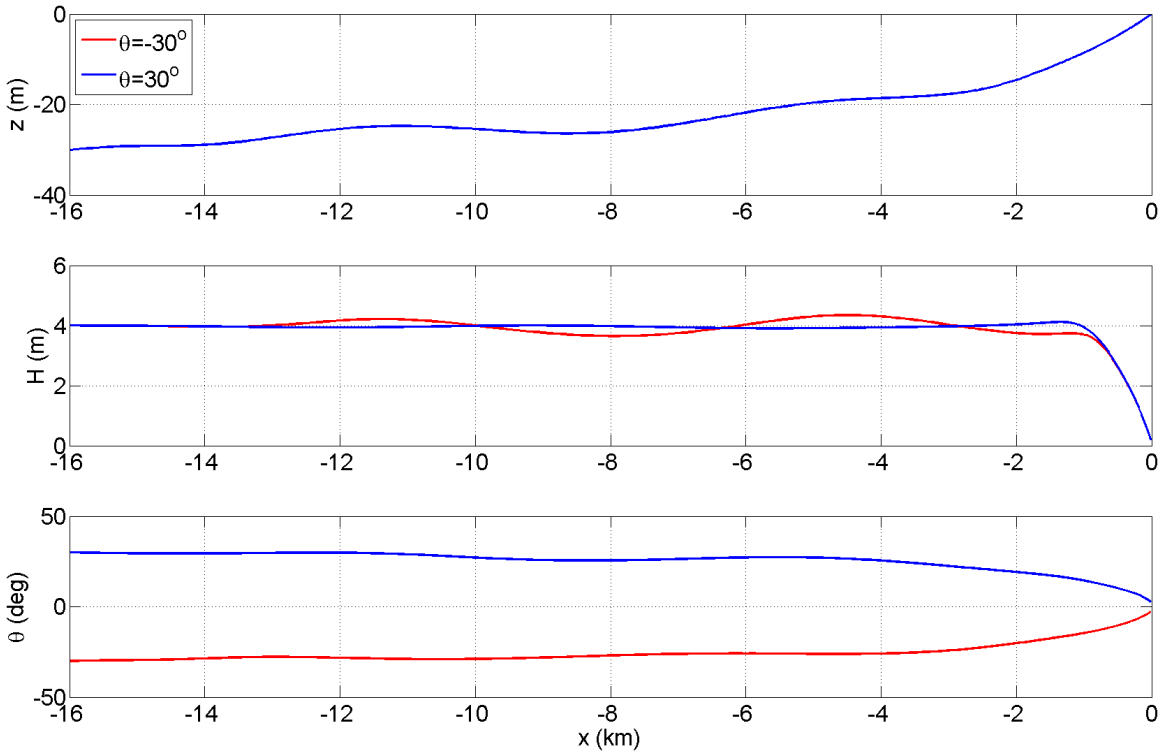

Figure 11: Cross-shore sections at y = 30 km for different mean incoming wave angles of (a) bottom elevation, (b) wave height and (c) wave direction.

and plunges to 0 m after it reaches the threshold for breaking around 1 km from shoreline. Similarly, due to refraction, wave direction begins from -30^o or 30^o, slowly varies and decreases to 0^o from positive or negative side according to the value set at south boundary. Overall, the wave height varies much more for waves coming along ridges, while the wave direction has similar magnitude of fluctuation and the peak values occur at different locations relative to the bottom topography.

3.2 Dominant Wave Transformation Mechanisms

To qualitatively identify the dominant wave transformation mechanisms that account for the ridge effect on wave properties, the difference between wave height with and without the ridge field is displayed in Figure 12. The wave height distribution pattern is different relative to the location of ridge crests for each incoming wave angle.

When $\theta = -60^o$, higher wave heights appear on the left side of the ridge crest,

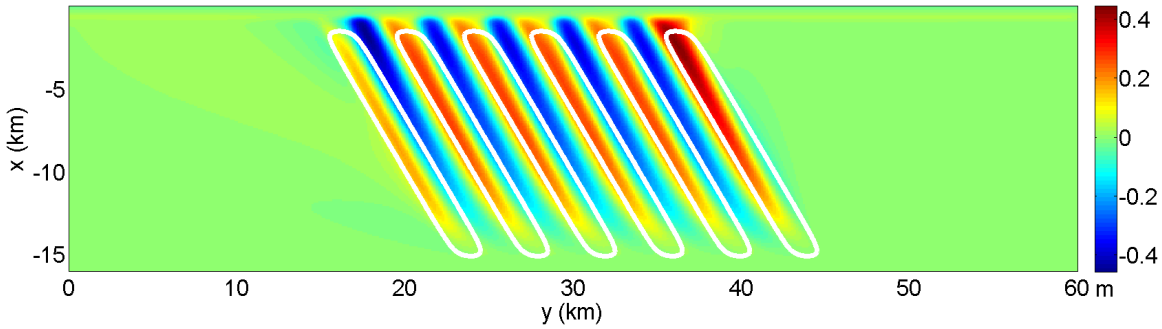

(a) $\theta = -60^o$

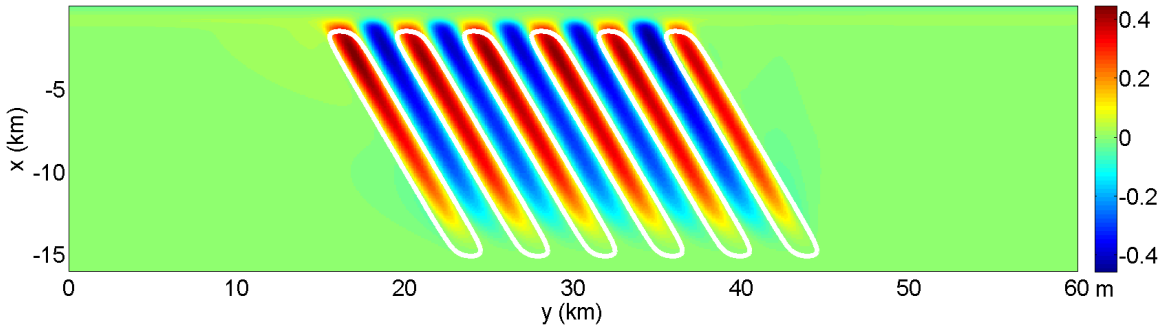

(b) $\theta = -30^o$

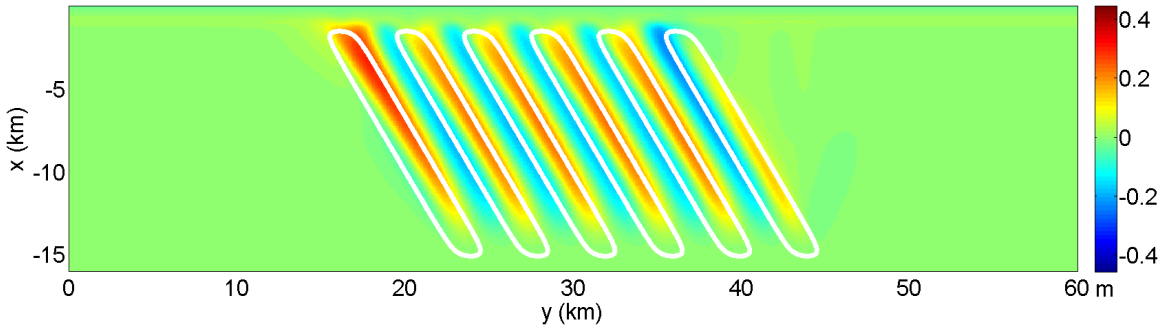

(c) $\theta = 0^o$

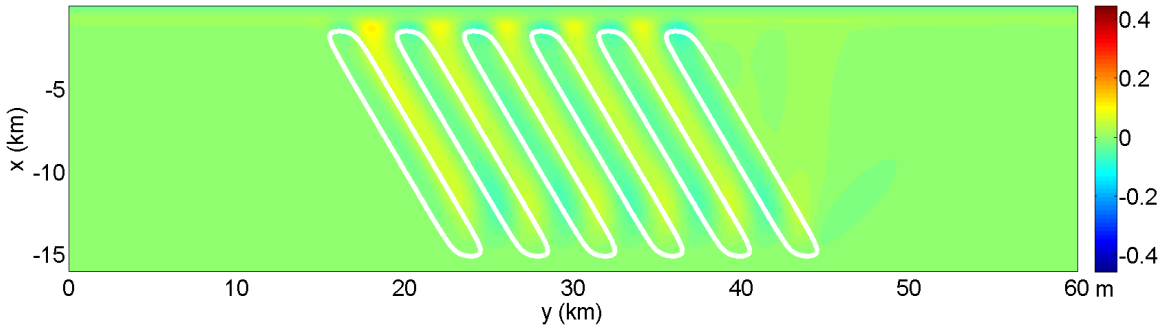

(d) $\theta = 30^o$

Figure 12: Wave height difference for bathymetry with and without ridges. White contours are the outline of ridges. Mean incoming wave angles are from top to bottom (a) $\theta = -60^o$, (b) $\theta = -30^o$, (c) $\theta = 0^o$ and (d) $\theta = 30^o$.

while lower wave heights are around the right side of the ridge crest. When $\theta = -30^o$, the maximum wave heights are on the center line of the ridge crest, with troughs surrounded by minimum values. When $\theta = 0^o$, the pattern is opposite to the situation with $\theta = -60^o$, higher wave heights are now on the right side of the ridge crest. For $\theta = 30^o$, it seems that part of the higher or lower wave height zones also fall in between ridge crests and troughs, but the order of magnitude is one fourth as large as the other three cases. The association between incident wave angle and the degree of wave height variation over the ridges is clear. Although the general pattern that the alongshore variation becomes more significant closer to shore applies for all these cases, the incoming wave angle of -30^o has the strongest fluctuation, followed by -60^o and 0^o, while 30^o has the minimum variation.

It is well-known that waves tend to refract toward shallower regions, causing wave focusing and de-focusing, generating higher or lower wave heights. In addition to refraction, as waves enter shallow water, they also shoal and increases in height and steepness until they break. One would expect that the maximum wave height would fall in the troughs. Therefore, further analysis and discussion is necessary to address why the magnitude and regions for wave converging and diverging change with different incoming wave angles.

Given conservation of energy in a steady-state case, wave height at one location is readily calculated as,

$$H_2 = H_0 \sqrt{\frac{C_{g0}}{C_{g2}}} \sqrt{\frac{\cos\theta_0}{\cos\theta_2}} = H_0 K_s K_r, \tag{19}$$

where C_g is the group velocity, $K_s = \sqrt{C_{g0}/C_{g2}}$ is the shoaling coefficient and $K_r = \sqrt{\cos\theta_0/\cos\theta_2}$ is the refraction coefficient, 0 denotes deep water properties, and 2 denotes any location of interest.

Group velocity is expressed as,

$$C_g = nC, \tag{20}$$

where the ratio of the group velocity to the celerity n is

$$n = \frac{1}{2}\left(1 + \frac{2kh}{\sinh 2kh}\right). \tag{21}$$

The shoaling coefficient, K_s is solved and the problem is closed given dispersion relation in equation (10). Thus, with wave height data for the entire domain, the refraction coefficient can be represented as,

$$K_r = \frac{H_2}{H_0}\frac{1}{K_s}. \tag{22}$$

Shoaling and refraction coefficients for incoming wave angles varying from -60^o to 30^o with 30^o resolution are shown in Figure 13. It is obvious from the definition of the shoaling coefficient, that K_s does not change with different incoming wave angles but is a function of depth, since it depends on group velocity, C_g. Higher K_s happens within the range of ridges, while lower K_s concentrates on troughs. From the south boundary to an alongshore section close to wave breaking, K_s slowly increases. However, the range of variation for K_s is one fourth as large as for the refraction coefficient, K_r.

The refraction coefficient varies in both magnitude and distribution for the different angles. For example, for incoming wave angle of -60^o, higher K_r values focus on the left side of the ridge crests, while lower K_r values appear on the right side of the ridge crests. For incoming wave angle of -30^o, extreme values are produced within the ridge crests or troughs only. When incoming wave angle equals to 0^o, the pattern is opposite to -60^o with higher K_r values focus on the right instead of the left side of the ridge crests, while lower K_r values on the left side of the ridge crests. For incoming wave angle of 30^o, the variation of K_r is much smaller than the other three cases and the extreme values are on the ridge crests or troughs.

This pattern for the refraction coefficient is very similar to the wave height variation in Figure 12, as higher or lower K_r happens in a similar range as higher or

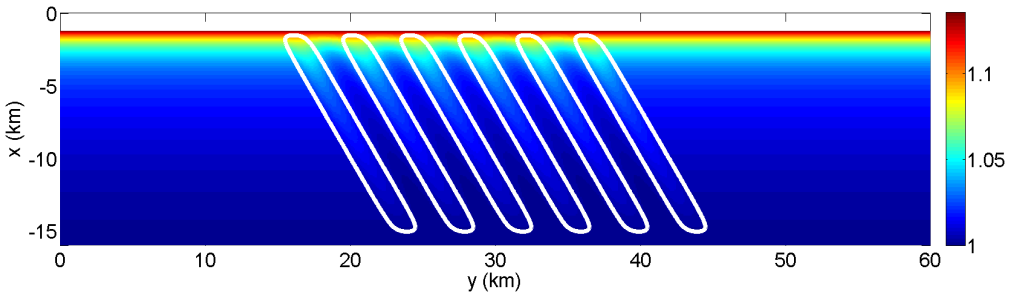

(a) K_s

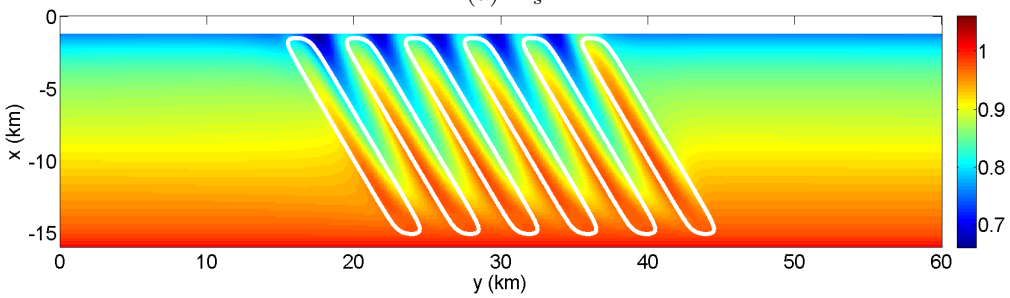

(b) $K_r, \theta = -60^o$

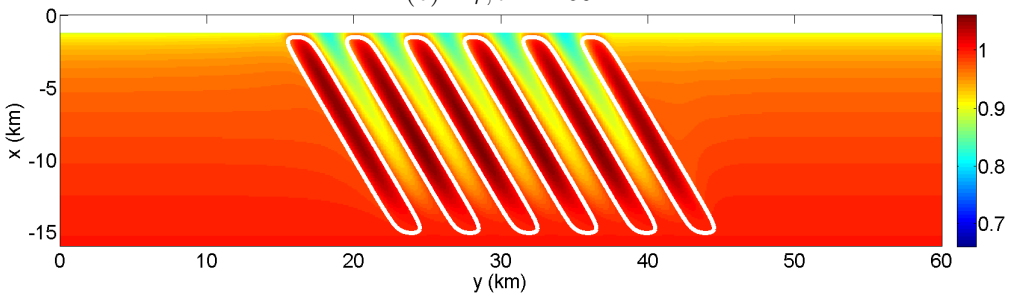

(c) $K_r, \theta = -30^o$

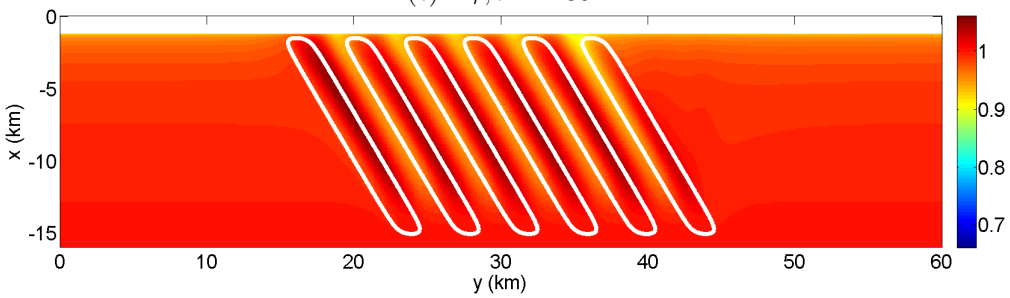

(d) $K_r, \theta = 0^o$

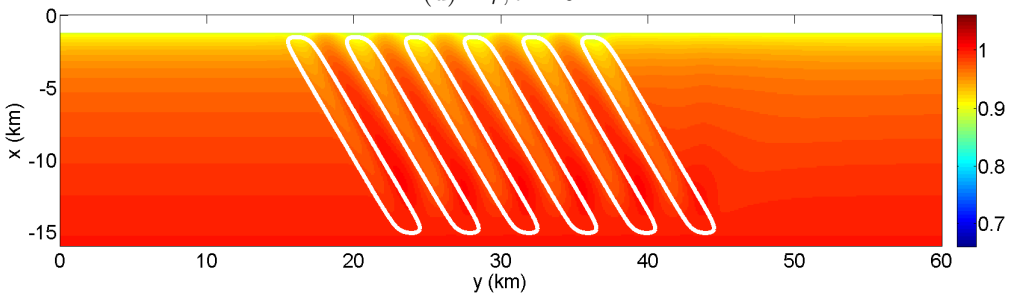

(e) $K_r, \theta = 30^o$

Figure 13: (a) Shoaling coefficient and (b-e) refraction coefficient for incoming wave angles (b) $\theta = -60^o$, (c) $\theta = -30^o$, (d) $\theta = 0^o$ and (e) $\theta = 30^o$ before wave breaking. White contours are the outline of ridges.

lower wave heights. Overall, due to the pattern similarity, it is evident the major mechanism that results in the observed variation of wave height is refraction.

3.3 Wave Rays Analysis

To further investigate how the existence of ridges affects wave propagation primarily through wave refraction, spectral and wave rays analysis is used to explain the energy distribution and the connection to wave height variations.

Figure 14 shows the directional spectra as a function of cross-shore distance along the middle line of the domain (y = 30 km) for different incoming wave angles. The difference between the first and the second column is that the former plots the directional spectra but the latter plots the difference between the spectra with and without ridges. The black dash line defines the incoming wave angle, and it is seen that energy originates around the incoming wave angle, progresses to a direction closer to 0^o by refraction. The gray dash-dot line draws the orientation of the ridges, which is -30^o in this chapter. Obviously, there exists strong fluctuation of energy for waves with angles corresponding the angle of ridges. The white line shows the depth variation with the alongshore mean removed, i.e. the variation of the ridges only. Also, dashed white vertical lines indicate the locations for ridge crests or troughs. The pattern of the directional spectral variation is different for each incoming wave angle but has similarities as energy fluctuation always concentrates around the orientation of ridges.

Using the case with θ equal to 0^o as an example (Figure 14 (e) and (f)), on the ridge crest 5 km from the shoreline, there is an area of energy increasing for angles between -60^o to -30^o. However, the energy is decreasing between angles -30^o to 0^o, but is slightly increasing energy between angles 0^o to 30^o. Furthermore, the energy variation is much smaller on the trough 8.3 km from the shoreline or on the ridge crest 11.6 km from the shoreline. Therefore, the conclusion here is that the combination of orientation of ridges and locations of ridge crests and troughs defines the energy

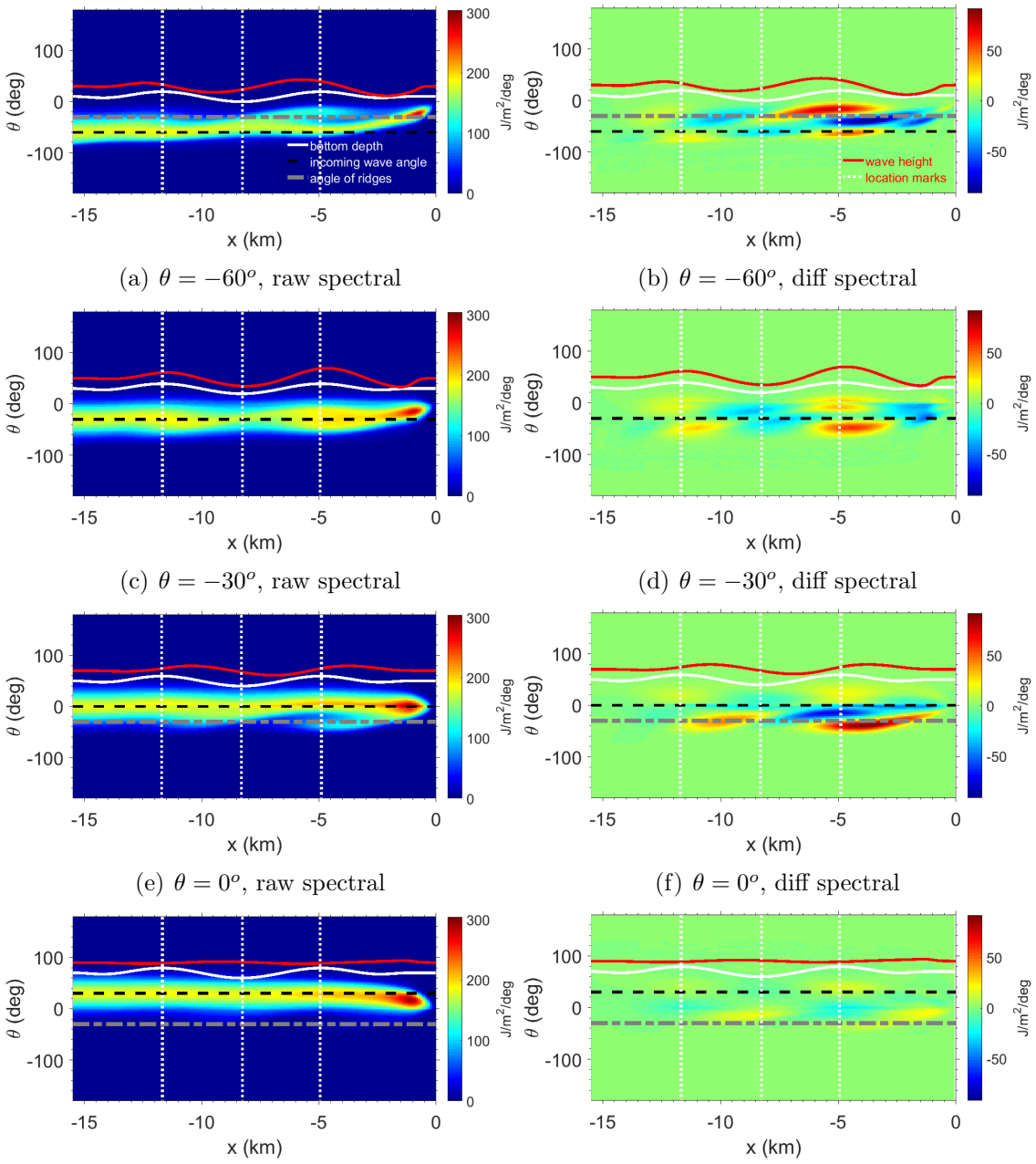

(a) $\theta = -60^o$, raw spectral

(b) $\theta = -60^o$, diff spectral

(c) $\theta = -30^o$, raw spectral

(d) $\theta = -30^o$, diff spectral

(e) $\theta = 0^o$, raw spectral

(f) $\theta = 0^o$, diff spectral

(g) $\theta = 30^o$, raw spectral

(h) $\theta = 30^o$, diff spectral

Figure 14: Directional spectra as a function of cross-shore distance along the middle line of the domain (y = 30 km) with mean incoming wave angles (a) $\theta = -60^o$, (c) $\theta = -30^o$, (e) $\theta = 0^o$ and (g) $\theta = 30^o$. Spectral differences calculated by directional spectra with ridges minuses without ridges are shown in (b) $\theta = -60^o$, (d) $\theta = -30^o$, (f) $\theta = 0^o$ and (h) $\theta = 30^o$. Wave height variation (red) and bathymetric variation (white solid) have their alongshore mean values removed.

distribution.

Another conclusion is that energy can be trapped or forced back to the orientation of the ridges, which explains the strong energy fluctuation around the ridge orientation for incoming angles of -60^o and 0^o. For example in Figure 14 (f), the mean incoming wave angle is 0^o but the largest magnitude of energy fluctuation is shown to be positive on one side of the ridge orientation line and negative on the other. For the case of incoming wave angle of -30^o, the energy is trapped and transfered back and forth around the angle of ridges, which matches the incoming wave angle in this case, and the energy fluctuation on either side of the centerline has a similar magnitude. When the incoming wave angle is 30^o, there is 60^o difference from the orientation of ridges. As a result, even though there is energy fluctuation near the angle of ridges and around the incoming wave angle, the magnitude of the energy variation is minimal.

In addition, the connection to wave height variation is also found by comparing the regions of energy gaining or losing to the red line. To be more specific, higher wave heights always correspond to higher energy gains, while lower wave heights usually have more energy losses. Using the case with the incoming wave angle of -60^o as an example, there is significant energy increasing from -30^o to 0^o and smaller range of energy decreasing from -60^o to -30^o 6 km from the shoreline. This particular directional spectrum is associated with a local maximum for wave height. Using the same location but switching to incoming wave angle of 0^o, dramatic energy loss is found from -30^o to 0^o with smaller energy increasing from -60^o to -30^o. Correspondingly, this is associated with a local minimum for wave height. For the incoming wave angle of -30^o, the situation is more straightforward. Energy is either increasing or decreasing for all directions, which results in higher or lower wave heights, respectively. For the incoming wave angle of 30^o, the variation of energy is minimal such that the wave height does not change as much as the previous cases.

A further illustration of the distinct and dramatic variation in the energy distribution, the directional spectra from the middle of the domain (y = 30 km) on the ridge crest and close to the south boundary, is drawn in Figure 15 for an incoming wave angle of 0^o. The reason for using 0^o as the incoming wave angle here, and in the following ray tracing analysis, is to make the results more straightforward and easy to understand. When the mean incoming wave angle is 0^o, (a) the incoming energy covers from -50^o to 50^o; (b) the closer to 0^o, the higher the associated incoming energy.

Based on Figure 15, as waves propagate from the south boundary to the location of ridge crest with a ridges-excluded topography, the energy spectrum simply becomes narrow banded and the peak energy increases. Induced by refraction, all the wave angles are altered closer and closer to shore normal. In contrast, when the bathymetry includes the ridges, the energy spectrum appears to have a bump from -60^o to -30^o, a pit from -30^o to 0^o and a mild but successive increase from 10^o to 50^o, compared to the spectrum with the ridges excluded. This is consistent with the color directional spectrum on the same location in Figure 14.

Nevertheless, even though the energy is shown to be trapped around the ridge orientation, the specific reason why the shape of the spectra changes has not been well-explained yet. One possible theory is that the higher energy portion of the spectrum originates from an incoming wave angle that contains higher energy. To evaluate this theory, an appropriate approach is to utilize a ray-tracing technique. To perform the ray tracing, a general method is outlined (Dalrymple and Dean, 1991).

In steady state conditions, if the coast has straight and parallel depth contours, the wave direction θ is calculated from Snell's law,

$$\frac{\sin\theta}{C} = \frac{\sin\theta_0}{C_0}. \tag{23}$$

However, offshore contours are usually irregular and vary along a coast, which makes

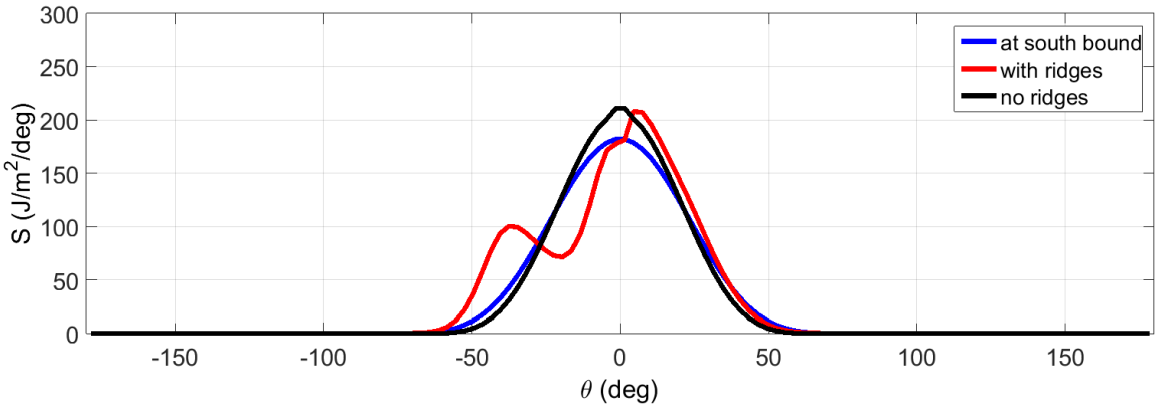

Figure 15: Directional spectra on the ridge crest (x = -4.9 km, y = 30 km; same location with no ridges) and close to the south boundary (x = -15.5 km, y = 30 km) for an incoming wave angle of 0^o.

the alongshore component from the conservation of waves equation indispensable,

$$\frac{\partial k \sin\theta}{\partial x} - \frac{\partial k \cos\theta}{\partial y} = 0 \tag{24}$$

or

$$k\cos\theta\frac{\partial\theta}{\partial x} + k\sin\theta\frac{\partial\theta}{\partial y} = \cos\theta\frac{\partial k}{\partial y} - \sin\theta\frac{\partial k}{\partial x}. \tag{25}$$

The ray-tracing technique treats the path of the waves in a coordinate system **s**,**n** such that **s** is in the wave direction and **n** normal to it, defined as

$$x = \mathbf{s}\cos\theta - \mathbf{n}\sin\theta, \tag{26}$$

$$y = \mathbf{s}\sin\theta + \mathbf{n}\cos\theta. \tag{27}$$

Applying the chain rule yields,

$$\frac{\partial}{\partial s} = \frac{\mathrm{d}x}{\mathrm{d}s}\frac{\partial}{\partial x} + \frac{\mathrm{d}y}{\mathrm{d}s}\frac{\partial}{\partial y} = \cos\theta\frac{\partial}{\partial x} + \sin\theta\frac{\partial}{\partial y}, \tag{28}$$

$$\frac{\partial}{\partial n} = \frac{\mathrm{d}x}{\mathrm{d}n}\frac{\partial}{\partial x} + \frac{\mathrm{d}y}{\mathrm{d}n}\frac{\partial}{\partial y} = -\sin\theta\frac{\partial}{\partial x} + \cos\theta\frac{\partial}{\partial y}. \tag{29}$$

Thus, the equation for ray-tracing is established as

$$\frac{\partial\theta}{\partial s} = \frac{1}{k}\frac{\partial k}{\partial n}. \tag{30}$$

In terms of implementation, the next increment (i+1) in Cartesian coordinate is discretized based on the relation to the (**s**,**n**) coordinate system for the present location (i)

$$x_{i+1} = x_i + \Delta s \cos\theta_i, \tag{31}$$

$$y_{i+1} = y_i + \Delta s \cos\theta_i. \tag{32}$$

Based on the chain rule, the gradient of wave number in the **n** direction is,

$$\frac{\mathrm{d}k_{i+1}}{\mathrm{d}n} = -\sin\theta_i \frac{\mathrm{d}k_{i+1}}{\mathrm{d}x} + \cos\theta_i \frac{\mathrm{d}k_{i+1}}{\mathrm{d}y}. \tag{33}$$

The wave ray equation is discretized as

$$\theta_{i+1} = \theta_i + \Delta s \frac{1}{k_{i+1}} \frac{\mathrm{d}k_{i+1}}{\mathrm{d}n}. \tag{34}$$

Thus, given a small increment Δs in **s** direction, a wave direction and a location in the Cartesian coordinate where the wave ray starts, the wave path is solved numerically.

If a positive increment along a wave ray is applied in the calculation step, this is called forward ray tracing. Whereas if a negative increment is applied, the wave ray is traced backwards and is called reverse ray tracing. Combined, a complete wave ray from the point of origin with a specific angle is obtained. Examples are shown in Figure 16 where the distinction between the magenta and white solid line is two different wave angles specified on the ridge crest.

As previously stated for a mean incoming wave angle of 0^o shown in Figure 15, the closer the associated incoming wave angle is to zero, the higher the wave energy in the local wave spectrum will be. In Figure 16 (a), for a wave angle of -15^o on the ridge crest, the wave ray starts from an angle of -44.09^o. Wave energy in the local spectrum that corresponds to a wave angle of -15^o originates from an angle that contains lower energy. In contrast in Figure 16 (b), the wave angle of -45^o on the ridge crest is generated by an incoming wave angle of -22.05^o, which contains higher

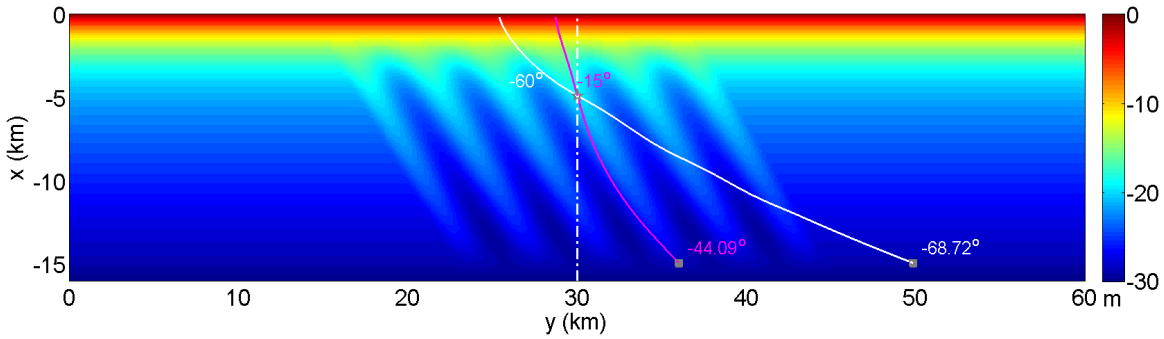

(a) $\theta_1 = -60^o,\ -15^o$

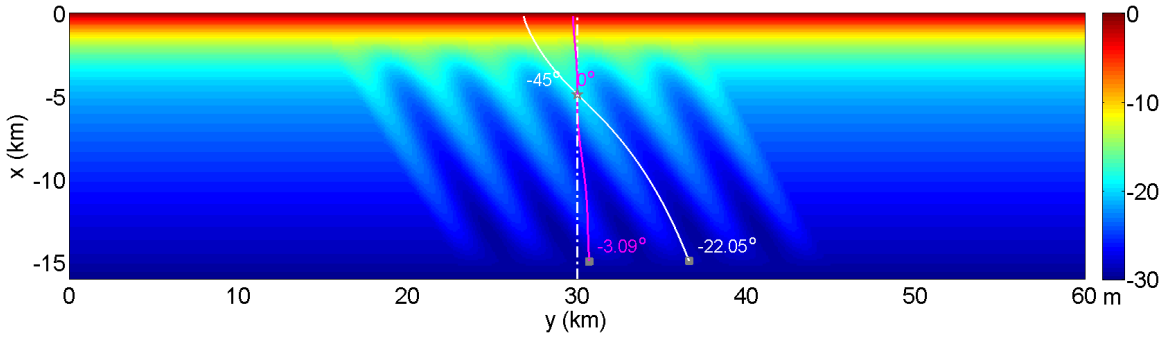

(b) $\theta_1 = -45^o,\ 0^o$

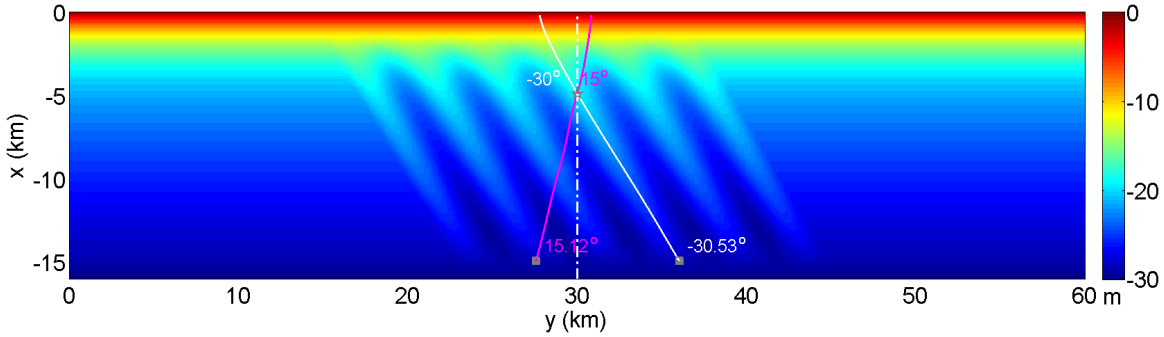

(c) $\theta_1 = -30^o,\ 15^o$

Figure 16: Ray tracing originating on the ridge crest (x = -4.9 km, y = 30 km) with (a) $\theta_1 = -60^o$ (white), -15^o (magenta), (b) $\theta_1 = -45^o$ (white), 0^o (magenta), (c) $\theta_1 = -30^o$ (white), 15^o (magenta). Background color plot represents the bathymetry. White dot-dash line is the middle line of the simulated domain. Values by the square indicate computed wave direction close to south boundary.

energy and causes the wave energy associated with -45^o to be higher. This analysis also provides the explanation for the pit from -30^o to 0^o and the bump from -60^o to -30^o in Figure 15. Similarly, the wave energy associated with 0^o on the ridge crest is slightly decreased, since it begins from -3.09^o close to the south boundary. The wave angle of -30^o on the ridge crest does not change much from its start point, which has an angle of -30.53^o. As shown in Figure 15, minimal energy difference is associated with -30^o in the directional spectra for the bathymetry with or without ridges.

Wave rays using the reverse ray-tracing technique originating on the ridge crest, with angles every 3^o from -60^o to 60^o are shown in Figure 17 (a). As seen from the figure, when wave angles on the ridge crest are within the range of -42^o to -15^o, wave rays are trapped within the ridges. To be more specific, all wave rays within $\pm 15^o$ of the ridge crest orientation refract towards the ridge crest and remain trapped. Whereas the waves approaching with large angles relative to the ridge orientation tend to follow standard Snell's law refraction.

For a different perspective, the computed incoming wave direction is plotted as a function of the wave direction from on top of the ridge crest. To help interpret the results, a dashed line corresponding to Snells Law is plotted (positive sloped dashed line in Figure 17 (b)) as the theoretical offshore angle required to produce each onshore angle. Consider a wave with an angle of -45^o on the ridge crest, according to Snell's law (red dashed lines), it would have a corresponding angle around -55^o at the offshore boundary. However, the actual angle shown by the black curve is -22.05^o, which suggests an energy increase as the smaller source angle contains higher energy. Similarly, a wave with angle of -15^o on the ridge crest corresponds to an offshore angle of -45^o which is much larger than what Snell's law predicts and therefore leads to an energy decrease.

Another dashed line is constructed based on a wave on the ridge crest having a negative (or positive) angle corresponding to a positive (or negative) incoming

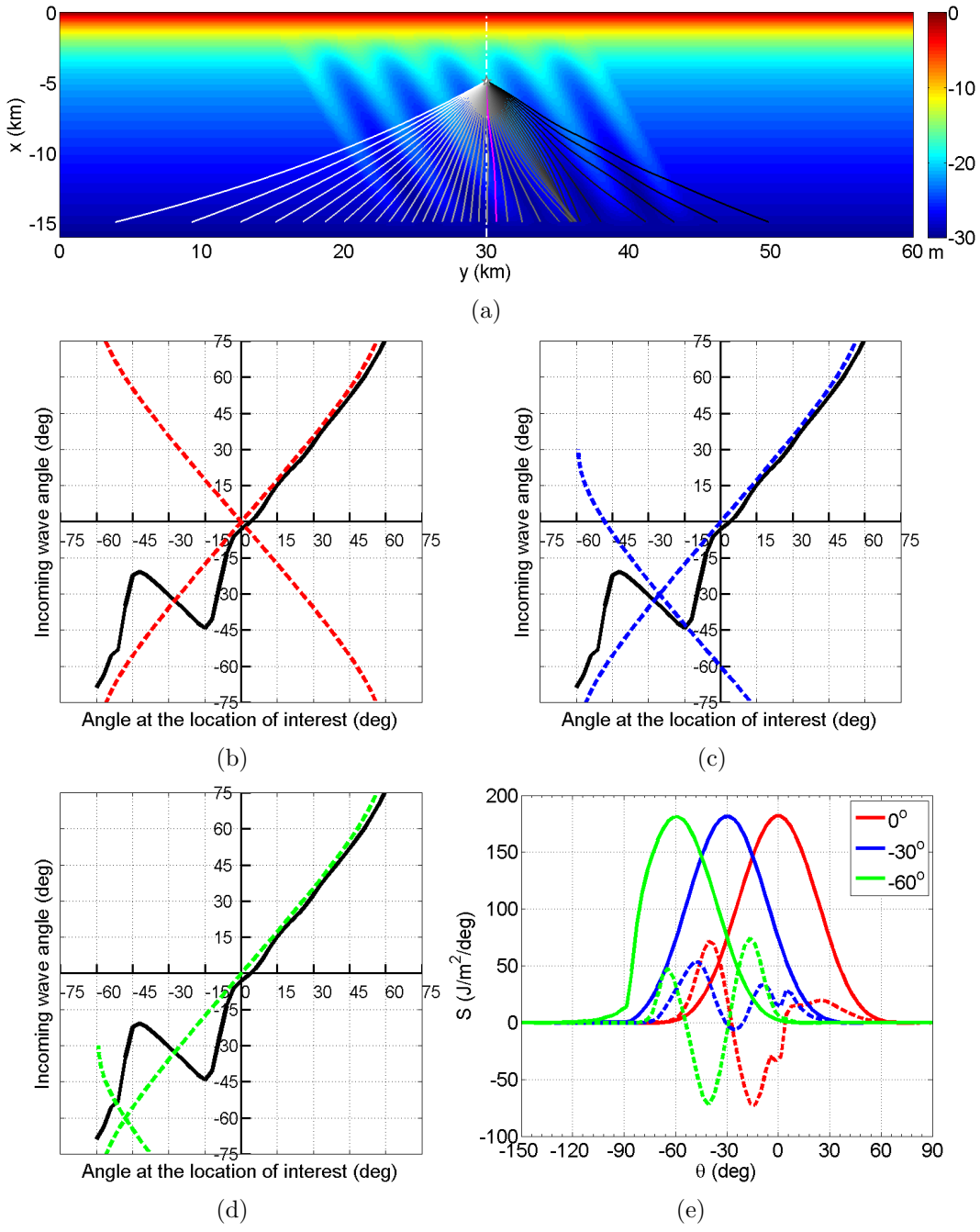

Figure 17: (a) Reverse ray tracing originating on the ridge crest (x = -4.9 km, y = 30 km). Color range of wave rays represents wave angles specified on the ridge crest, from -60^o to 60^o (black to white, magenta is 0^o) with 3^o resolution. Background color plot is the bathymetry, white dot-dash line is the middle line of the simulated domain. (b-d) Computed incoming wave direction close to south boundary as a function of wave directions on the ridge crest by the wave ray equation (solid) and by the Snell's Law (dash). (e) (Solid) Directional spectra close to south boundary. (Dash) The difference in directional spectra between with and without ridges on the ridge crest.

angle. In this case, due to the symmetry of the spectrum about the mean wave direction, any wave on the ridge crest that has a corresponding offshore angle equal to the negative of what is predicted by Snells Law would have no change in energy. Therefore, the second dashed line is constructed using vertical symmetry. This line does not represent waves, but it helps differentiate increase/decrease energy. Thus, separated by the red dashed lines, this figure is divided into four groups: the left and the right sectors represent energy increase, while the top and the bottom sectors indicate energy decrease. With this conclusion, it is obvious in Figure 17 (b) that energy increases for wave angle ranges from -60^o to -30^o, decreases for wave angle ranges from -30^o to 3^o, slightly and mildly increases for wave angle ranges from 3^o to 60^o on the ridge crest. This is also consistent with the analysis for Figure 15 and fits the pattern shown in Figure 17 (e) which presents the directional spectrum 500 m from the south boundary and the difference in directional spectra on the ridge crest with and without ridges for incoming wave angle of -60^o, -30^o and 0^o.

One thing worth mentioning is that in subplots (b-d) of Figure 17 the black solid curve does not change with different incoming mean wave angles as long as the location of interest remains the same, however the energy fluctuation associated with each mean incoming wave angle will be different. Thus, the only change is the dashed lines for reference. Snells Law still applies and the positive sloped dashed line is still used to distinguish when energy stays the same. However, the point of intersection with the negative sloped dashed line changes the mean offshore wave angle and the corresponding inshore point according to Snells Law. Then the line is constructed using vertical symmetry about the mean offshore angle once again. Conveniently, moving the dashed lines by this procedure makes the analysis straightforward such that the left and the right sector always represent energy increase, while the top and the bottom indicate energy decrease.

For the case with -30^o incoming wave angles, the black curve falls in the left

and the right sector almost entirely, which suggests the energy increases for every direction except for -30^o to -15^o. Also, the deviation between the black curve and the blue dashed lines are quite small in the energy-decrease region compared with energy-increase region. This also shares a similar pattern as shown in Figure 17 (e) for the incoming wave angle of -30^o.

When the incoming mean wave angle is -60^o (Figure 17 (d)), it is shown that energy is increasing for angles from -60^o to -50^o, decreasing from -50^o to -30^o and increasing again from -30^o to 0^o. This catches the slight energy increase from -60^o to -53^o, the decrease from -53^o to -30^o and the energy increase from -30^o to 0^o in Figure 17 (c). However, the left bump of the green dashed line in Figure 17 (e) can not be fully explained, since wave angles that are beyond -60^o are not calculable using reverse ray-tracing.

In summary, the ray-tracing technique is an effective and especially helpful approach for explaining the variation in the energy spectrum for different incoming wave angles. Generally speaking, portions of the directional spectrum with decreased energy has waves arriving from directions further from the offshore mean angle. Likewise, an increase implies that energy is transfered from an angle that is closer to the mean incoming wave angle.

It was shown in Figures 12 and 13 that the variability of wave heights relative to the locations of ridges changes for the different incoming wave angles. In order to understand how refraction affects the wave height distribution, the reverse ray-tracing technique is applied to different locations such as the ridge zero-crossings to the left and right side of the crests.

Figure 18 shows reverse ray-tracing results and energy spectra for a location on the ridge zero-crossing to the left side of the crest along the middle line of the domain. Based on Figure 18 (a), wave rays which start from within $\pm 15^o$ of the ridge orientation tend to converge toward the ridge angle. However, this effect is less than for the

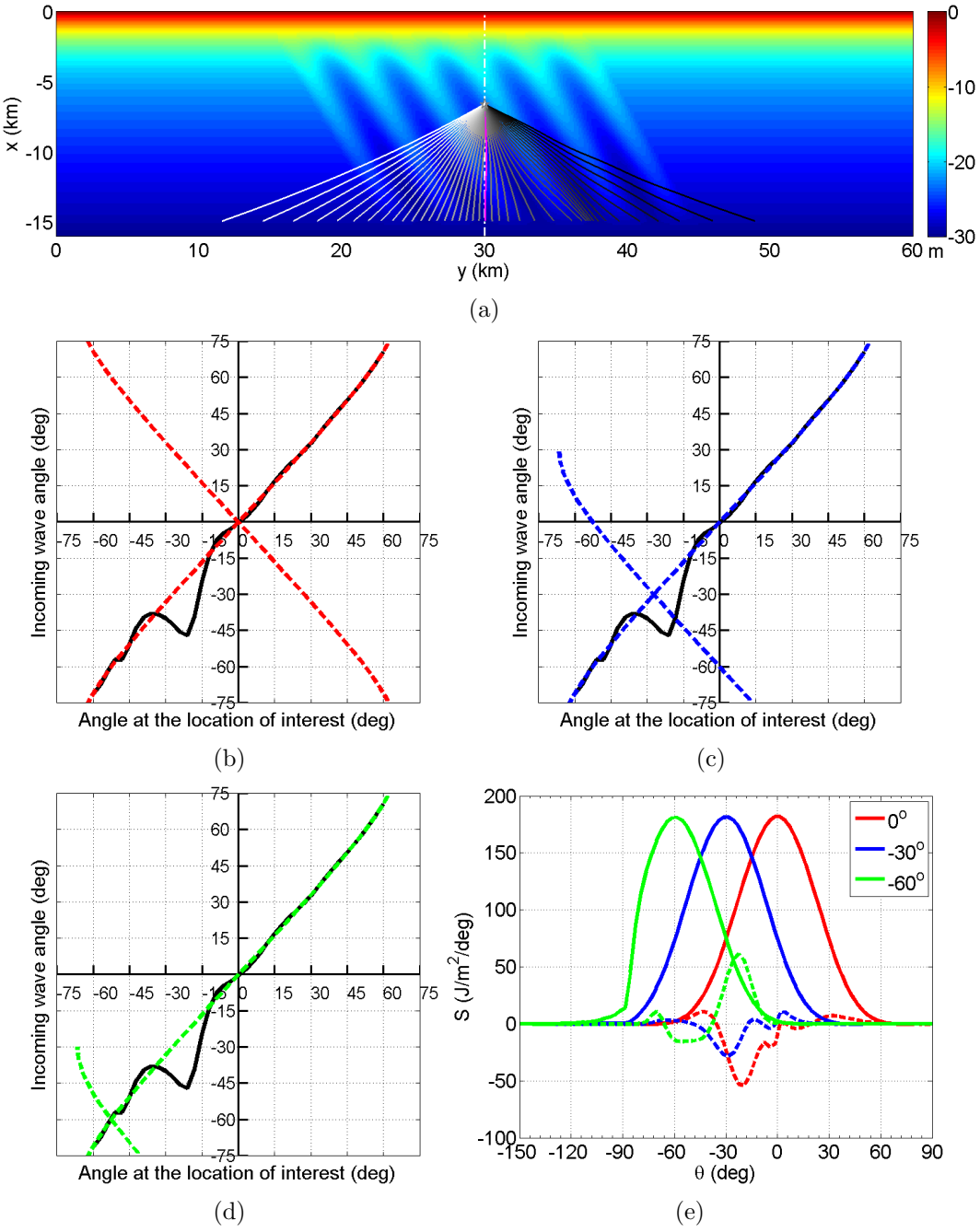

Figure 18: (a) Reverse ray tracing originating on the LHS zero-crossing of the ridge crest (x = -6.6 km, y = 30 km). Color range of wave rays represents wave angles specified on the LHS zero-crossing of ridge crest, from -60^o to 60^o (black to white, magenta is 0^o) with 3^o resolution. Background color plot is the bathymetry, white dot-dash line is the middle line of the simulated domain. (b-d) Computed incoming wave direction close to south boundary as a function of wave directions on the LHS zero-crossing of ridge crest by the wave ray equation (solid) and by the Snell's Law (dash). (e) (Solid) Directional spectra close to south boundary. (Dash) The difference in directional spectra between with and without ridges on the LHS zero-crossing of ridge crest.

wave rays originating on the ridge crest in Figure 17. In general for this location, the angles ranging from -30^o to -15^o are the ones with distinct wave direction changes compared with the incoming wave angles close to the south boundary.

As shown in Figure 18 (b), when the mean incoming wave angle is 0^o, it is clear that wave angles varying from -36^o to -10^o fall in the bottom sector, which represents decreased energy. Also, wave angles varying from -45^o to -36^o are within the range of left sector and, thus, indicate a slight increase in energy. This matches closely with the red dashed line in Figure 18 (e), a small bump for directions from -54^o to -36^o and a strong pit for directions from -36^o to 0^o.

When the mean incoming wave angle is -30^o (Figure 18 (c)), wave angles from -20^o to -10^o are within the right sector due to the change of reference. As a result, for the mean incoming wave angle of -30^o in Figure 18 (e), the energy increases for wave angles from -20^o to -10^o. The decrease from -36^o to -20^o remains strong and explains the negative variation in energy spectrum for the same range of directions.

When the mean incoming wave angle is -60^o (Figure 18 (d)), wave angles from -45^o to -36^o are in the top sector and angles from -36^o to -10^o are in the right sector. Correspondingly, the energy decreases for directions from -45^o to -36^o and increases dramatically for directions from -30^o to -10^o.

For the location on the ridge zero-crossing to the right side of the ridge crests (Figure 19 (a)), more wave rays are trapped by the effect of the ridges. For the mean incoming wave angle of 0^o in Figure 19 (e), there is a huge bump for directions between -60^o to -24^o and a relatively deep pit from -24^o to 0^o. Correspondingly, the black curve in Figure 19 (b) is in the left sector for angles from -57^o to -28^o and in the bottom sector for angles from -28^o to 0^o.

For the incoming wave angle of -30^o in Figure 19 (e), the energy is increased from -72^o to -32^o and from -18^o to -6^o. Similarly, the incoming wave angles are within the left and the right sectors in Figure 19 (c), for these ranges indicating waves

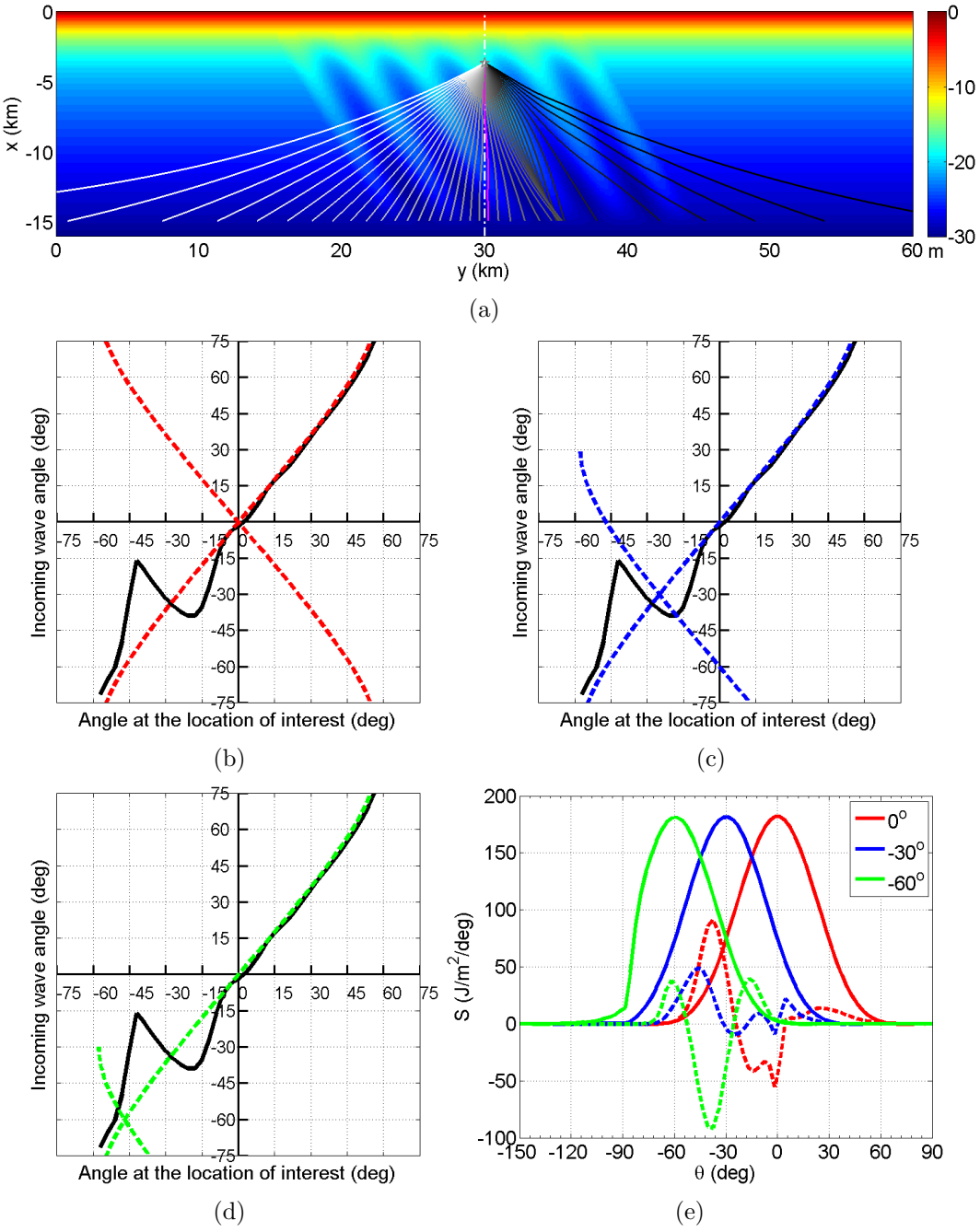

Figure 19: (a) Reverse ray tracing originating on the RHS zero-crossing of the ridge crest (x = -3.7 km, y = 30 km). Color range of wave rays represents wave angles specified on the RHS zero-crossing of ridge crest, from -60^o to 60^o (black to white, magenta is 0^o) with 3^o resolution. Background color plot is the bathymetry, white dot-dash line is the middle line of the simulated domain. (b-d) Computed incoming wave direction close to south boundary as a function of wave directions on the RHS zero-crossing of ridge crest by the wave ray equation (solid) and by the Snell's Law (dash). (e) (Solid) Directional spectra close to south boundary. (Dash) The difference in directional spectra between with and without ridges on the RHS zero-crossing of ridge crest.

arriving from closer to the mean direction.

For the incoming wave angle of -60^o in Figure 19 (e), energy increases appear from -72^o to -50^o and from -26^o to 0^o, while a significant energy drop is produced from -50^o to -26^o. In Figure 19 (d), the black curve is positioned in the left sector for wave angles greater than -57^o to -50^o, in the top sector for wave angles from -50^o to -30^o and in the right sector for wave angles from -30^o to 0^o.

Using subplot (e) of Figure 17, 18 and 19, the wave height is higher if the integral of the difference in directional spectra is positive. Thus, for the incoming wave angle is 0^o (red dashed lines) in Figure 17 (e), the area of the positive energy variation between with and without ridges almost cancels out with the area of the negative variation for the location on the ridge crest. The positive variation from -60^o to -30^o is caused by waves transfered from closer to the mean incoming wave direction with higher associated energy, as shown in subplot (b). The negative variation from -30^o to 0^o is induced by wave energy transfered from larger angles relative to the mean incoming wave direction. Due to the energy increase canceling the energy decrease, the wave height stays the same. For the location on the ridge zero-crossing to the left of the crest in Figure 18 (e), the majority of the energy fluctuation is in the negative side. In correspondence to subplot (b), this is due to waves refracted from larger angles relative to the mean incoming wave angle and, thus, carrying lower associated energy and generating lower wave heights. For the location on the ridge zero-crossing to the right of the crest in Figure 19 (e), the area of the positive energy variation is larger than the area of the negative variation leading to longer wave heights. In other words, the wave height is higher on the right side of the ridge crest and lower on the left side of the ridge crest.

For the incoming wave angle of -60^o (green dashed lines), the pattern is the opposite. On the ridge crest (Figure 17 (e)), the increasing energy caused by waves refracted from smaller angles relative to the mean incoming wave angles still cancels

out with the energy loss generated by waves with lower associated energy, which is transferred from incoming waves with larger angles relative to the mean incoming wave angle. Since the energy increasing part is equal to energy decreasing part, the wave height remains the same. On the ridge zero-crossing to the left of the crest (Figure 18 (e)), the positive energy variation is much larger, which corresponds to the energy increasing below the green dashed line in subplot (d) and results in the highest wave height. On the ridge zero-crossing to the right of the crest (Figure 19 (e)), there are more negative instead of positive energy variations, which can also be explained correspondingly by subplot (d). For waves with an incoming mean angle of -60^o, higher wave heights are on the left side of the ridge crests, while lower wave heights are on the right.

For the incoming wave angle of -30^o (blue dashed lines), there are larger areas in the positive energy variation than in the negative variation for the location on the ridge crest (Figure 17 (e)) and on the ridge zero-crossing to the right side of the crest (Figure 19 (e)). However, the total area is the largest on the ridge crest, which corresponds to highest wave height on the ridge crest.

In conclusion, higher wave heights are shown on the left side of the ridge crest when the incoming wave angle is greater than the angle of ridges. In contrast, higher wave heights are presented on the right side of the ridge crest when incoming wave angle is smaller than the angle of ridges. In essence, the waves originating from close to the mean directions with more energy tend to refract and concentrate on the opposite side of the ridge crest leading to bigger wave heights. The reverse ray-tracing technique is extremely useful in explaining the wave height distribution through its connection to the energy spectrum variation.

3.4 Wave breaking analysis

This section explores wave breaking patterns resulting from the influence of the ridge field, including the method for identifying wave-breaking locations, the distribution of breaking wave heights and the analysis with the energy spectrum.

When the fraction of breakers (corresponds to Q_b in SWAN) first reaches 0.2% for a cross-shore section, that location is marked as a breaker point. Applied to the entire domain for each cross-shore section, the locations of breakers are linked as an alongshore varying breaker line. In Figure 20, this method is shown to be effective by displaying the breaker extraction results for four distinct cross-shore sections. The red dots marking the breaking location catch the transition points between prebreaking and breaking quite successfully, as shown by the wave height variations.

Based on the breaking locations, the alongshore variations of the breaking wave height and wave direction are shown in Figure 21. The wave height has mean values of 4.2 m, 4 m, 4 m and 3.3 m for the incoming angles of 0^o, -30^o, 30^o and -60^o. This implies that the incoming wave angle in addition to the ridges modify the magnitude of the breaking wave properties. Furthermore, the waves break further inshore for the incoming wave angle of -60^o, due to the smaller waves from the energy leakage problem for large incoming wave angles. Due to refraction, the mean wave directions in breaking sections are smaller than their corresponding incoming wave angles, except for 0^o. In terms of the fluctuation pattern, -60^o and -30^o have the most significant variations. As before, it is seen that peak wave heights for the incoming wave angle of -60^o are shifted to the left compared with incoming wave angle of -30^o. Also, the highest breaking wave heights for incoming wave angle of 0^o are shifted to the right, whereas wave height pattern for incoming wave angle as 30^o is the opposite to -30^o and has the mildest fluctuation.

Because the breaking wave height pattern has a similar distribution such that higher wave heights appear at different locations according to the mean incoming wave

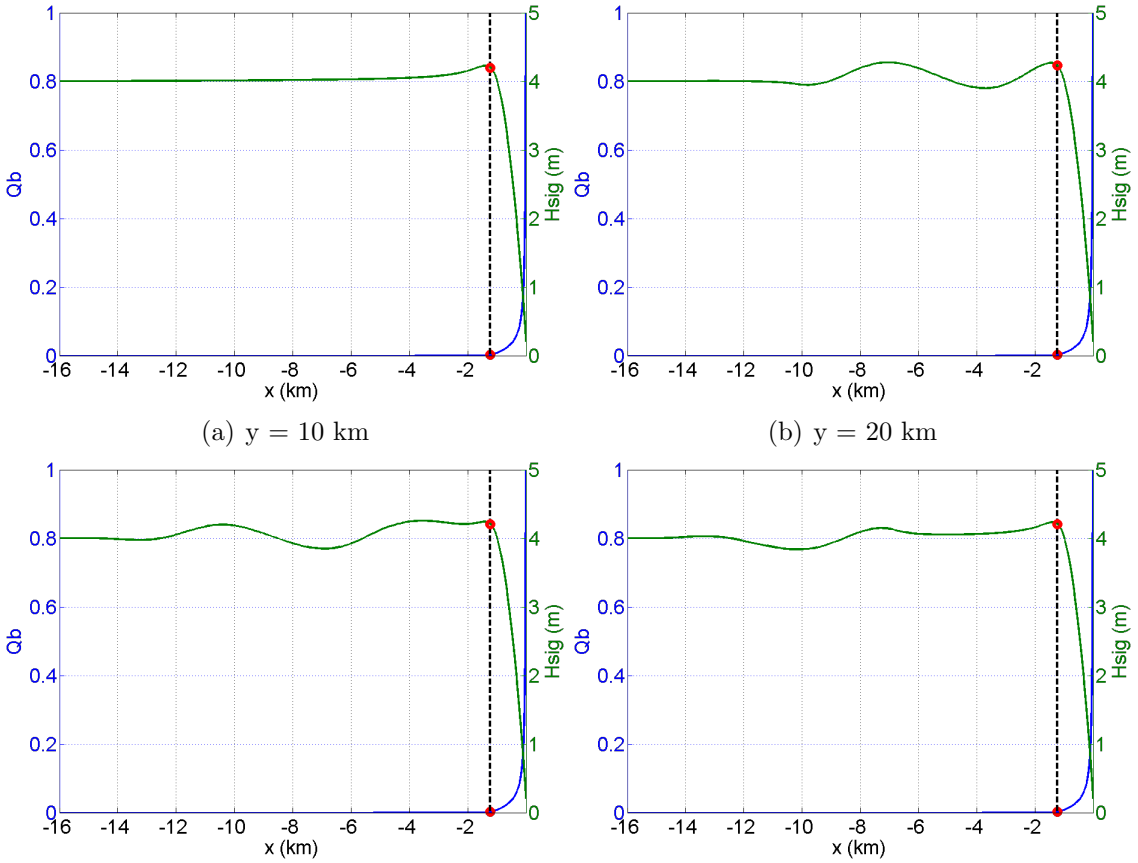

(a) y = 10 km (b) y = 20 km

(c) y = 30 km (d) y = 40 km

Figure 20: Identification of the wave-breaking point on four cross-shore section ($\theta = 0^o$). The fraction of breaking waves (Q_b) (blue) and wave height (green) for the cross-shore sections. Red dots and black dash lines show the location and the corresponding wave properties at breaking condition ($Q_b = 0.2\%$). Cross-shore sections include (a) y = 10 km; (b) y = 20 km; (c) y = 30 km; (d) y = 40 km.

angles, the energy spectrum analysis is repeated here. The first column of Figure 22 shows the directional energy spectrum along the breaking section for incoming wave angles varying from -60^o to 30^o. The second column presents the difference in the directional energy spectra between the with and without ridges cases. Again, the ridges create strong variations except for the incoming wave angle of 30^o. In this case, the energy variation is insignificant due to the incoming wave angle essentially being perpendicular to the ridges. The variation patterns for incoming wave angles of -60^o and 0^o are basically opposite to each other. When the incoming wave angle is -60^o, dramatic energy decreases appear for waves with the same direction as the

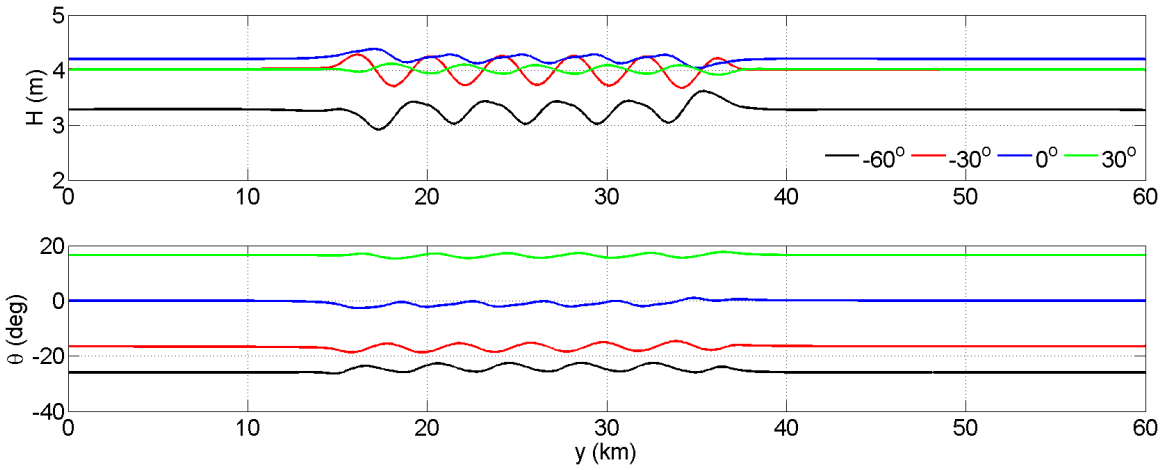

Figure 21: Wave properties for the alongshore breaker line for mean incoming wave angle of -60^o(black), -30^o(red), 0^o(blue) and 30^o(green). Panels from top to bottom are (a) wave height and (b) wave direction.

angle of ridges. In contrast, energy increases enormously for the same angle, when the incoming wave angle is 0^o. These large changes in energy are centered on the ridge crests but are balanced by energy increases/decreases in directions near shore normal. Hence the wave height on the ridge crest remains almost unchanged. However, these patterns are not symmetric about the ridge crest and the areas of increasing energy are skewed to the left for -60^o and to the right for 0^o leading to larger waves on the left side for -60^o and right side for 0^o. The pattern is symmetric about the ridge crests with increased energy associated with mean incoming angle of 30^o due to the waves being trapped on the ridges, leading to larger waves on the ridge crest.

3.5 Summary

This chapter presents the variations in the wave field induced by the shore oblique ridges. The variations in the wave field are much stronger when the predominant wave direction is along the ridges rather than perpendicular to the ridge crests. Furthermore, the local maximum of wave heights is on the opposite side of the ridge crest relative to the incoming wave direction. If the incoming wave angle is equal to the angle of ridges, the local maximum or minimum is located on top of the ridge crest

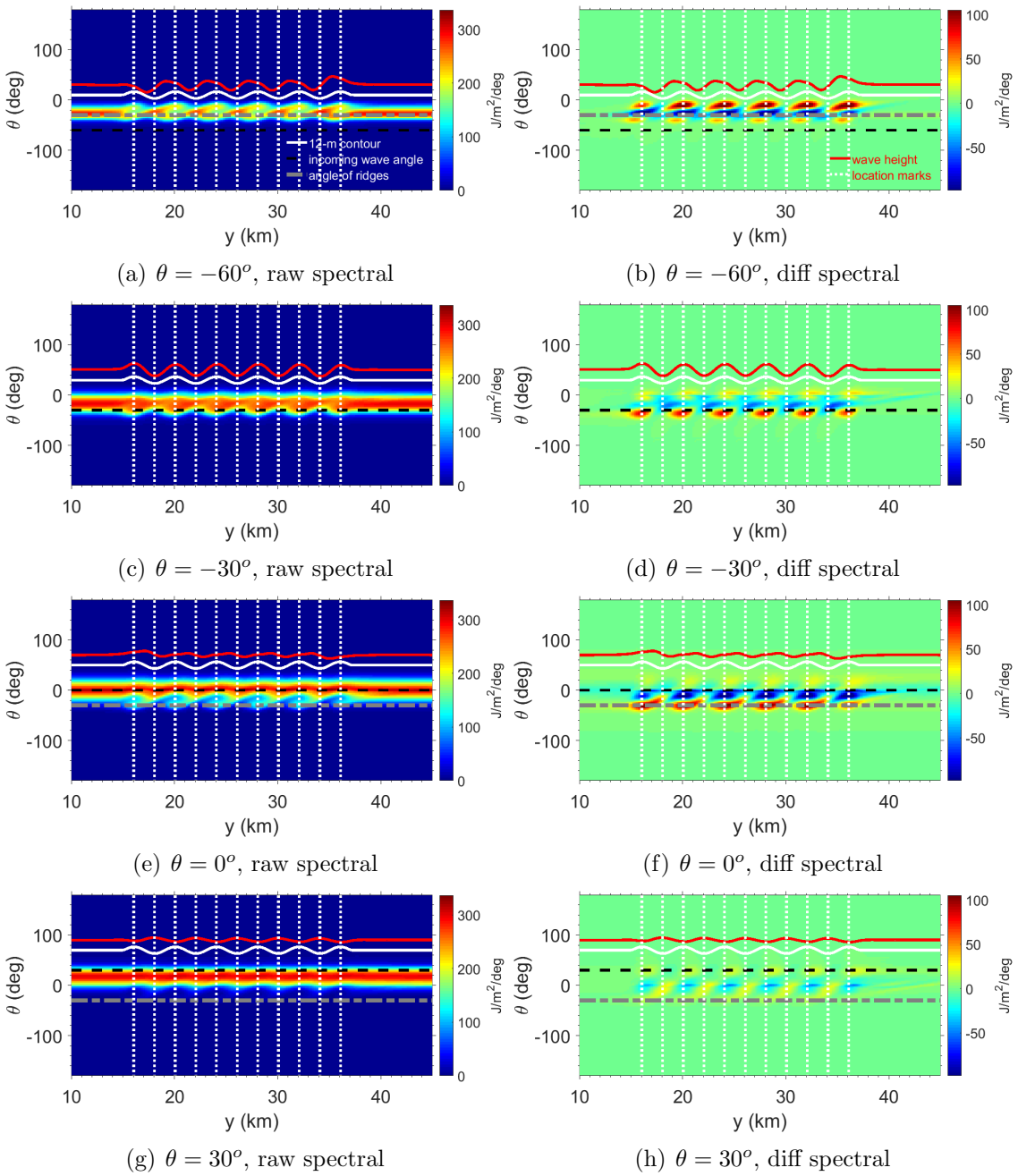

(a) $\theta = -60^o$, raw spectral

(b) $\theta = -60^o$, diff spectral

(c) $\theta = -30^o$, raw spectral

(d) $\theta = -30^o$, diff spectral

(e) $\theta = 0^o$, raw spectral

(f) $\theta = 0^o$, diff spectral

(g) $\theta = 30^o$, raw spectral

(h) $\theta = 30^o$, diff spectral

Figure 22: Directional spectra along the breaker line for mean incoming wave angles (a) $\theta = -60^o$, (c) $\theta = -30^o$, (e) $\theta = 0^o$ and (g) $\theta = 30^o$. Directional spectra with ridges minuses the one without ridges for (b) $\theta = -60^o$, (d) $\theta = -30^o$, (f) $\theta = 0^o$ and (h) $\theta = 30^o$. White lines indicate the depth variation for the cross-shore position with an alongshore averaged 12 m bottom depth. Red lines are the breaking wave heights.

or trough. By removing the effect of shoaling from the wave pattern, the dominant mechanism for the wave height patterns is likely refraction instead of shoaling, since the refraction coefficient appears to have a similar spatial distribution as the wave height pattern.

By evaluating the energy spectra and using a ray-tracing technique, it is found that the directional energy spectra usually has strong energy fluctuations for wave angles at the direction of the ridge orientation. Based on the ray-tracing analysis, the energy in the local directional spectra is strongly related to the direction for the corresponding incoming wave. The closer the direction of the corresponding incoming wave angle is to the mean wave angle, the higher the associated energy will be. For a given location, if more of the source incoming waves are close to the mean wave angle, the wave height will be bigger.

Wave breakers are identified and extracted when the fraction of breakers reaches 0.2%. Analyzing wave breaking properties along the breaker line, waves with larger incoming wave angles break further inshore due to both the refraction effect and the energy leakage. The wave height distribution shares the pattern induced by the relation between the incoming wave angles and the orientation of ridges such that higher wave heights happen on the left (right) side of the ridge crests in cases of the mean incoming wave angles greater (less) than the angle of ridges.

CHAPTER IV

ALONGSHORE SEDIMENT TRANSPORT AND SHORELINE CHANGE

Alongshore sediment transport has been attracting considerable effort in coastal engineering due to the impact of the transport on coastlines, which is the motivation for building coastal structures such as jetties and breakwaters to impede the alongshore movement of sand. Thus, this chapter presents the analysis of total alongshore sediment transport, the volumetric sediment transport rate (Check, 2004), using standard empirical equations for estimating the transport. The effect of incoming wave angles on alongshore sediment transport and the corresponding shoreline change is related back to the alongshore variation of ridge field.

4.1 Standard Methods for Alongshore Sediment Transport

A commonly used total alongshore transport equation is the Komar and Inman (1970) or so-called CERC (1984) formula given as

$$I_l = KP_l, \tag{35}$$

where I_l is the immersed-weight sediment transport rate, K is an empirical sediment transport coefficient and P_l is the alongshore component of wave energy flux given by

$$P_l = \left(ECn\cos\alpha\sin\alpha\right)_b, \tag{36}$$

in which C is the wave celerity, α is the wave angle relative to the shoreline and subscript b denotes the breakpoint. E is the wave energy density given by

$$E = \frac{1}{8}\rho g H_b^2, \tag{37}$$

where ρ is the seawater density, g is the gravity acceleration, H is the root-mean-square wave height. n is the ratio of wave group speed to wave celerity given by

$$n = \frac{1}{2}\left(1 + \frac{2kh}{\sinh 2kh}\right). \tag{38}$$

The immersed-weight sediment transport is related to the volumetric sediment transport rate as follows,

$$Q_c = \frac{I_l}{\rho(s-1)g(1-p)}, \tag{39}$$

where s is the relative density of the sediment (the ratio of the sediment density to seawater density), and p is the porosity of the bed.

The constant K has been the subject of much debate. Komar and Inman (1970) suggested a K value of 0.77, based on the studies at two different beaches, El Moreno Beach and Silver Strand Beach. Schoonees and Theron (1994) indicated K to be around 0.4. Also, studies have been focused on defining a dependence on grain size. Komar (1988) and del Valle et al. (1993) suggested that K decreases with increasing D_{50}, whereas Haas and Hanes (2004) found that K has weak dependence on grain size.

Another widely used empirical predictive formula for total alongshore transport equation is the GENESIS model, which was developed by Hanson (1987), Hanson and Kraus (1989) and Gravens et al. (1991) as follows,

$$Q_g = \left[H^2 Cn\left(a_1 \sin 2\alpha - a_2 \cos\alpha \frac{\mathrm{d}H}{\mathrm{d}y}\right)\right]_b. \tag{40}$$

The nondimensional parameters a_1 and a_2 are given by,

$$a_1 = \frac{K_1}{16\left(\frac{\rho_s}{\rho} - 1\right)(1-p)}, \tag{41}$$

$$a_2 = \frac{K_2}{8\left(\frac{\rho_s}{\rho} - 1\right)(1-p)\tan\beta}, \tag{42}$$

where K_1 and K_2 are calibration parameters, $\tan\beta$ is the average bottom slope from the shoreline to the depth of active alongshore sediment transport.

The first term in Equation 40 is the same as the CERC formula, which expresses alongshore sand transport produced by obliquely incident breaking waves. Thus, K_1 shares the same magnitude as K in CERC equation. The second term accounts for the contribution of the alongshore gradient in breaking wave height $\mathrm{d}H_b/\mathrm{d}y$ to the alongshore transport rate (Ozasa and Brampton, 1981). K_2 is typically 0.5 to 1.0 times K_1 (Hanson and Kraus, 1989).

Hanson and Kraus (1989) commented that this GENESIS model can account for shoreline change resulting from spatial and temporal gradients in alongshore sediment transport. Taking in account the alongshore gradient of the wave height, the simulation results for shoreline evolution become more realistic, especially in the vicinity of structures in the shallow water zone, where the breaking wave height is fluctuating substantially due to diffraction (Hanson and Kraus, 1989).

4.2 Sediment Transport for -30^o Ridge Angle

In order to analyze the pattern of alongshore sediment transport and identify if there is a relation to the incoming wave angles relative to the ridge orientation as stated in the previous chapter, the ridge angle of the synthetic bathymetry is continued to be -30^o in this section. The empirical coefficients, K and K_1 are equal to 0.77 Komar and Inman (1970) and K_2 is equal to 0.8 times K_1 (Hanson and Kraus, 1989) in this chapter .

The alongshore sediment transport is calculated by the two empirical methods for the incoming wave angles from -68^o to 44^o (Figure 23). As shown in both of the subplots, when waves are coming from the southeast directions (negative angles), the alongshore sediment is transported westward (negative transport). In contrast, when waves are from the southwest directions (positive angles), the alongshore sediment transport is in the eastward direction (positive transport). Only when the waves are from shore normal does the sediment transport vary between eastward and westward

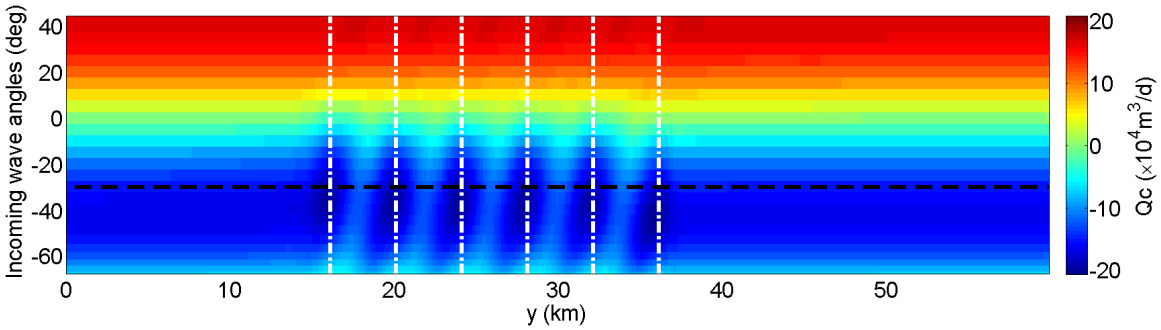

(a) Q_c

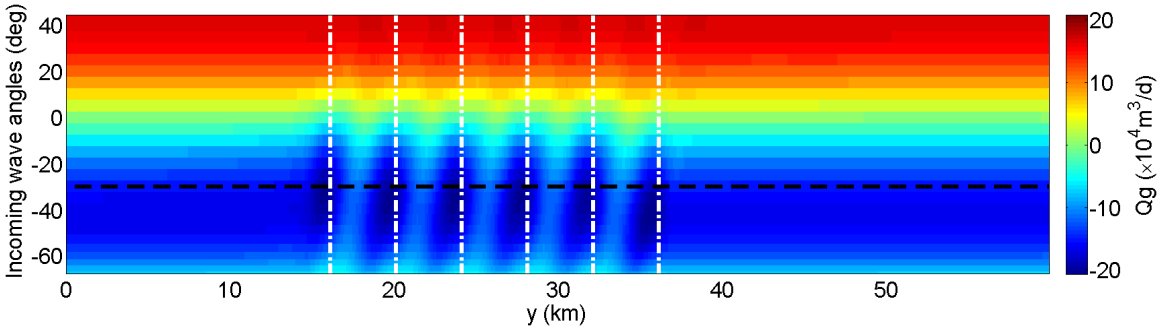

(b) Q_g

Figure 23: Alongshore sediment transport by (a) CERC (Q_c) and (b) GENESIS (Q_g) for the mean incoming wave angles from -68^o to 44^o. Positive (negative) incoming angles represent waves from the southwest (southeast). Black dash line is the angle of the ridges. White dot dash lines indicate the alongshore locations of the ridge crests along the averaged 12-m seabed topography.

directions.

The alongshore sediment transport has stronger variations when it is driven westward by the breaking waves. When it is transported eastward, the variation is much weaker. With the locations of ridge crests marked by the white dot dash lines, with troughs falling in between the white lines, it is seen that for the incoming wave angle of -30^o, the strongest (weakest) sediment transport appears on the ridge crests (troughs). For negative incoming wave angles greater than the ridge orientation, the local maximum of the alongshore sediment transport is pushed to the left side of the ridge crests. For incoming wave angles smaller than the ridge orientation, the local maximum is moved only slightly to the right side of the ridge crests. Overall, it is interesting to note that there is a slow transition of local maximum for sediment

transport to the east direction when incoming waves change from greater angles to smaller angles.

Comparing the alongshore sediment transport by CERC (subplot (a)) with GENESIS (subplot(b)), both methods yield similar results except for slightly greater variations and sharper difference produced by GENESIS. In order to understand the causes for the alongshore variability of the alongshore transport, the dominant properties in determining the pattern of sediment transport by CERC are evaluated.

In order to present the variation of sediment transport by CERC to reveal the dominant factors that account for this variation, the alongshore mean values for each incoming angle are removed from the alongshore sediment transport, the breaking wave heights and the breaking wave directions and are shown in Figure 24.

Due to the nature of this calculation process, it is necessary to clarify the meaning of negative versus positive values. Classified by the incoming wave direction, for waves from southeast (southwest), stronger sediment transport is characterized by negative (positive) values (subplot (a)). In terms of breaking wave directions (subplot (c)), for waves from southeast (southwest), larger breaking angles are negative (positive). For subplot (b), higher wave heights along breaker lines are always positive.

Based on this classification, the pattern is clear that stronger sediment transport on the left side of the ridge crests is associated with incoming wave angles greater than the ridge orientation. The migration of the local peaks to the right side of the ridge crests reduces with the smaller incoming wave angles. The alongshore sediment transport from the CERC formula is affected by both the breaking wave heights and the breaking wave directions. But how important are each of these properties in forming the sediment transport variation? The question is answered by presenting the wave heights and wave directions with the alongshore mean removed, as shown in subplots (b) and (c).

Similar to the pattern of sediment transport, the local maximum of breaking

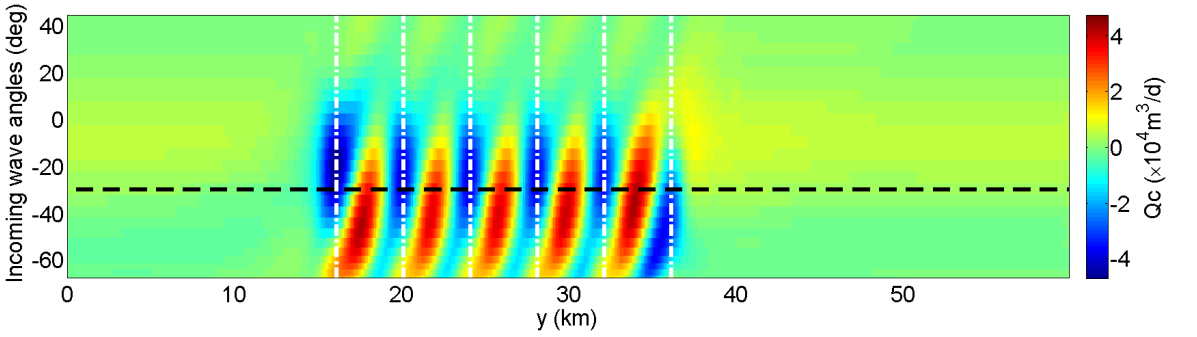

(a) Q_c

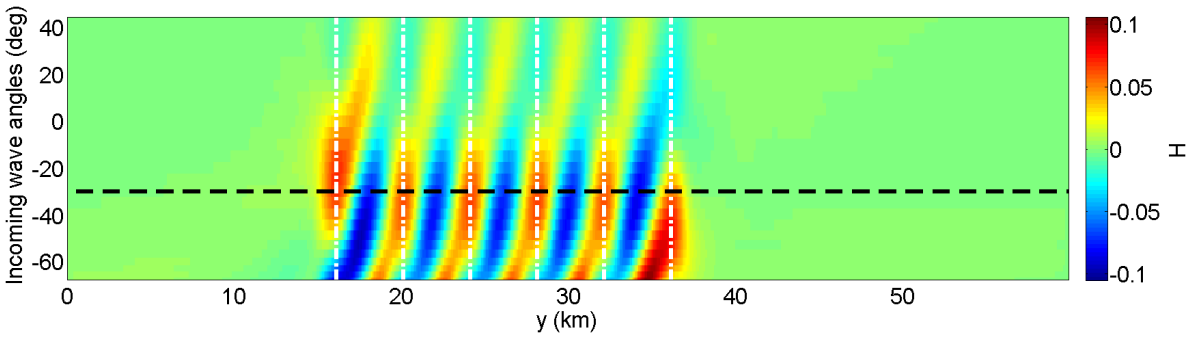

(b) H

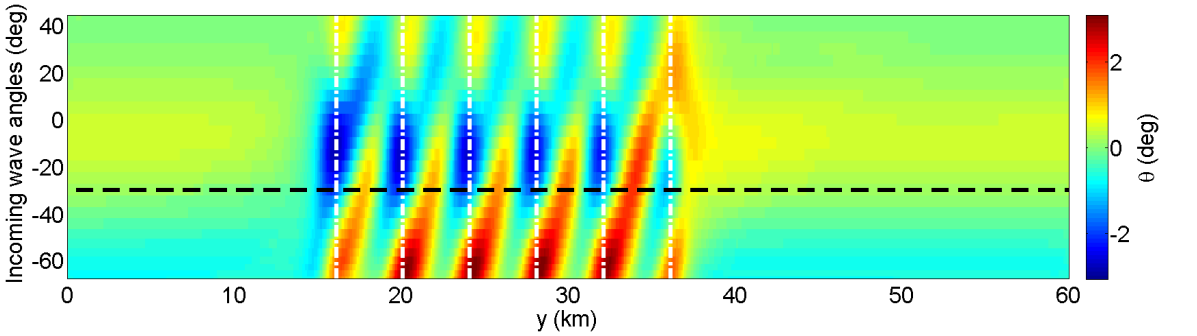

(c) θ

Figure 24: (a) Alongshore sediment transport by CERC, (b) breaking wave heights, and (c) breaking wave angles with their corresponding alongshore mean removed. Black dash line is the angle of the ridges. White dot dash lines indicate the alongshore locations of the ridge crests along the averaged 12-m seabed topography.

wave heights occurs for the incoming wave angle equal to the ridge orientation and is centered on the ridge crests, whereas the local minimum is on the troughs. The local peaks migrate from the left to the right side of the ridge crests as the incoming wave angles changes from greater to smaller than the ridge orientation. For the breaking wave directions, the larger breaking angles are on top of the ridge crests and the smaller angles are on the troughs for incoming wave angles equal to the ridge orientation. The transition of the local maximum is similar to the pattern of breaking wave heights.

Comparing the effect of breaking wave heights and breaking wave directions to the variation of sediment transport, it is seen that the breaking wave directions have stronger impact in forming the variation of sediment transport when the incoming wave angles are smaller than the ridge orientation. For these incoming angles, the movement of local minima or maxima to the east is more obvious in breaking wave directions compared with the breaking wave heights. The breaking angles are also important in forming the local minimum of sediment transport for the incoming wave angles greater than the ridge orientation. As shown in the figure, the area of smaller breaking angles is more similar to the area of weaker sediment transport. However, the breaking wave heights are critical in shaping the local maximum of sediment transport for the incoming wave angles greater than the ridge orientation. As seen in the Figure 24, the relative magnitude of the local maximum sediment transport is larger than the local maximum of wave directions and ends up strengthened by the higher breaking wave heights.

Therefore, the combination of breaking wave heights and breaking wave directions determines the variation of alongshore sediment transport. Separated by the angle of ridges, breaking wave height variations have a stronger influence at greater incoming wave angles and breaking wave angle variations have a larger impact at smaller incoming wave angles.

As stated previously, the alongshore sediment transport by GENESIS is similar to the transport by CERC formula. But there is a difference, which is caused by the alongshore gradient of breaking wave heights. To understand this difference and how the gradient of breaking wave heights modifies the sediment transport, the difference between CERC and GENESIS computed transport is presented in Figure 25 (a). When the incoming wave angles are from the southeast (southwest) directions, stronger sediment transport by GENESIS is positive (negative).

For the incoming wave angle of -30^o, stronger sediment transport by GENESIS is on the left side of the ridge crests, whereas the weaker sediment transport is on the right side of the ridge crests. This indicates that GENESIS is driving more alongshore sediment transport outwards from the ridge crest relative to the CERC transport. For the incoming wave angles greater than the ridge orientation, the stronger sediment transort by GENESIS is pushed further westwards from the left side of the ridge crests. It is pushed closer to the ridge crests for the incoming wave angles smaller than the ridge orientation.

When the incoming wave angles change from the southeast to southwest directions (positive angles), the location of stronger sediment transport by GENESIS (negative values in Figure 25 (a)) is shifted westwards to the left side of the ridge crests. As the incoming wave angles increase, the stronger GENESIS transport is moved eastwards to be closer to the ridge crests. Overall, the alongshore sediment transport by GENESIS is enhanced in the ridge troughs, increasing transport towards the ridge crests for waves coming from the west. This is in contrast to the transport when waves are approaching from the east where the enhanced transport is from the ridge crests outwards.

Figure 25 (b) presents the alongshore gradient of breaking wave heights, which is proportional to the difference between the CERC transport and GENESIS transport. Indeed, it shows the positive gradient on the left side of the ridge crests and

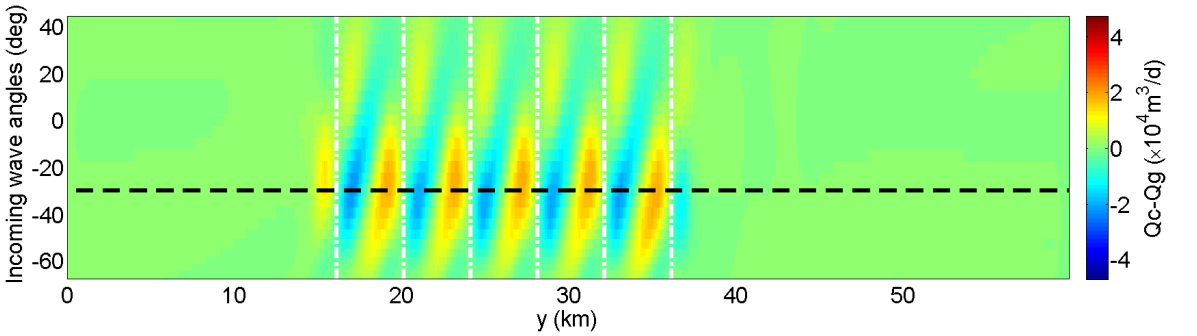

(a) $Q_c - Q_g$

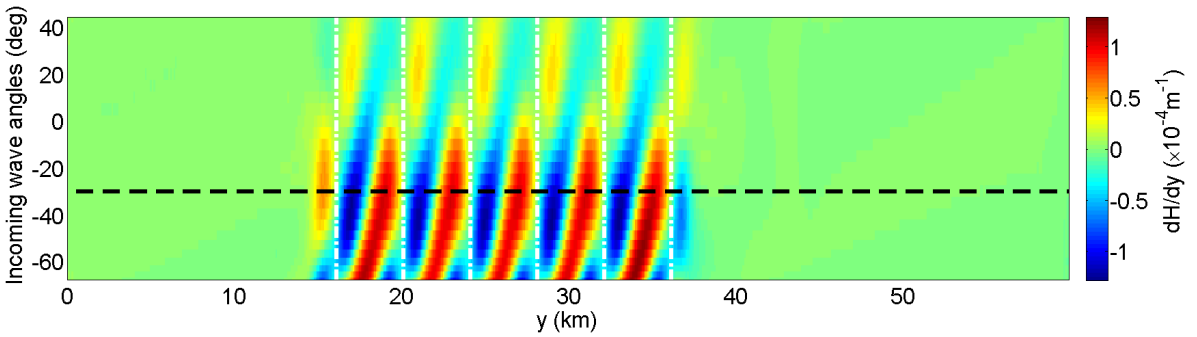

(b) dH/dy

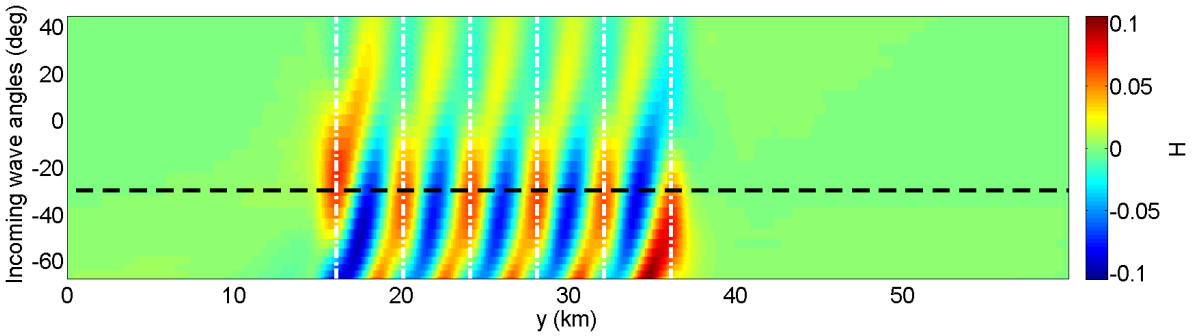

(c) H

Figure 25: (a) Alongshore sediment transport difference between CERC and GENESIS, (b) alongshore gradients of breaking wave heights, (c) breaking wave heights with their corresponding alongshore mean removed. Black dash line is the angle of the ridges. White dot dash lines indicate the alongshore locations of the ridge crests along the averaged 12-m seabed topography.

the negative gradient to the right side of the ridge crests for incoming waves from east, whereas the pattern is reversed for waves from the west. However, for waves approaching with angles much larger than the ridge orientation, the positive gradient migrates westward until it is nearly on the right side of the ridge crest. Looking at the wave height distribution in Figure 25 (c), it is clear that for waves from directions greater than the ridge orientation, higher breaking wave heights on the left side of ridge crests generate the positive alongshore gradient in wave height, enhancing transport toward the west relative to the CERC transport. For waves from directions smaller than the ridge orientation but from southeast, higher breaking wave heights on the ridge crests migrate to the right side of the crests as the incoming wave angles decrease. This breaking wave patterns enhance transport towards the west on the left side of the ridges and to the east on the right side of the ridges. For waves from the southwest, higher breaking wave heights appear on the troughs, which induces stronger transport towards the ridge crests.

Overall, although there is a difference between CERC and GENESIS, the difference is in the order of 0.1 compared with the alongshore sediment transport by CERC equation in Figure 24 (a) and, thus, CERC by itself is capable of capturing the major features of alongshore sediment transport induced by breaking wave heights and wave directions. Consequently, sediment transport by CERC is the approach used for analyzing the sediment transport and the shoreline response for the Fire Island scenario in the next section.

4.3 Alongshore Sediment Transport for Fire Island

In order to identify the effect of incoming wave angles on Fire Island sediment transport, the ridge orientation is set to be -60^o in the following two sections. Figure 26 presents the mean (first column) and standard deviation (second column) of wave properties along the breaker lines as a function of the mean incoming angle.

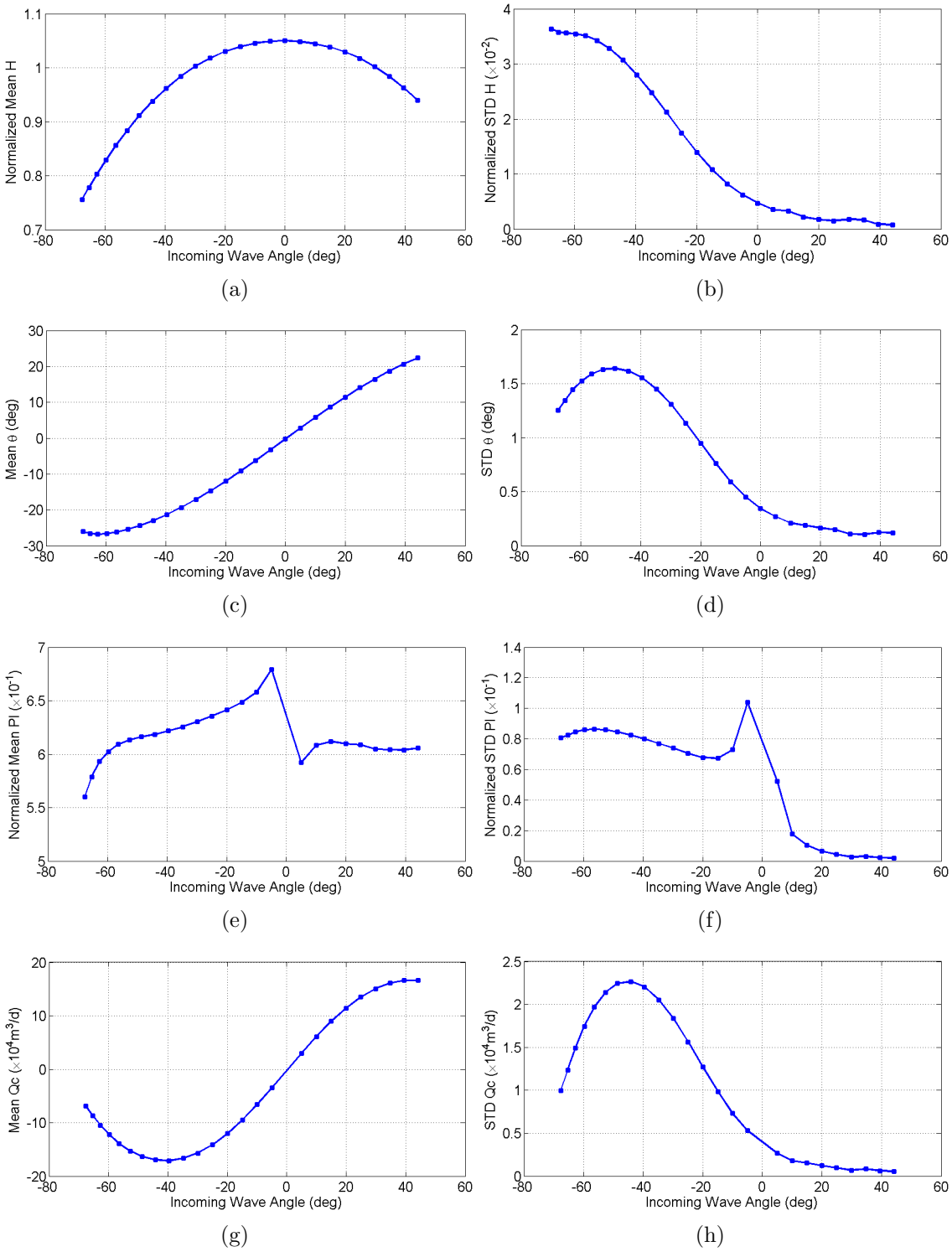

Figure 26: Different properties as a function of incoming wave angle. (a) normalized mean wave heights, (b) normalized STD wave heights, (c) mean wave angles, (d) STD wave angles, (e) normalized mean alongshore wave power, (f) normalized STD alongshore wave power, (g) mean sediment tranport by CERC, and (h) STD sediment transport by CERC

These wave properties include wave height, wave direction, alongshore wave power and alongshore sediment transport by the CERC formula. To minimize the effect of the spectral leakage, the wave heights and alongshore wave powers are normalized by the mean wave heights and the mean wave power 200 m from the offshore boundary. Also, due to the energy leakage effect, the actual incoming wave angles are different from the specified wave directions at the south boundary. Thus, the mean wave angles 200 m from the south boundary are used as the incoming angles.

As seen in Figure 26 (a), the normalized mean wave height is largest for normal incident waves ($\theta = 0^o$). For incoming wave angles from -30^o to 30^o, the normalized mean wave heights are above 1. For incoming wave angles beyond this range, the values are less than 1. Within the range of -30^o to 30^o, the shoaling effect dominates and causes the wave height to increase and be higher than the offshore wave heights. Outside that range, the refraction greatly affects the wave propagation such that the breaking wave heights are lower than the offshore wave heights.

In Figure 26 (b), the normalized STD wave heights show a trend of increasing alongshore standard deviations as the incoming wave angles vary from 45^o to -68^o. As shown in this figure (and similar to the previous chapter in which the ridge angle is -30^o), the strongest variation is near the orientation of ridges, which is -60^o. The magnitude of the largest STD is somewhat modest at only 3.5% of the offshore wave height.

In Figure 26 (c), the alongshore average wave directions are increasing with increasing incoming wave angles on both the positive and negative directions essentially following Snell's Law. More interestingly, in Figure 26 (d), the trend of the alongshore STD wave directions is similar to the wave heights, except for the peak shifted to -50^o. This peak is still close to the ridge orientation, although the energy leakage may play a role in shifting the peak slightly. The magnitude of the angle variation is fairly weak around 1.7^o.

Since the alongshore mean wave power is also normalized by the alongshore mean 200 m from the offshore boundary, the resulting pattern is the most intriguing as shown in Figure 26 (e). For the negative angles, the normalized mean wave power is larger for smaller wave angles. For the positive angles, the normalized mean wave power is increasing for smaller angles up to 15^o, and then remains fairly constant. The ridge field certainly plays a role in affecting the mean longshore wave power. For the positive angles where the ridges have less of an effect, the normalized wave power is nearly a constant. Upon closer inspection, the mean wave height is fairly symmetric between positive and negative angles, whereas the mean wave angles are slightly larger for the negative angles. This produces the higher longshore wave power for the negative angles. For example, for the mean incoming wave angles of $\pm 40^o$, the mean breaking angle from the -40^o mean incoming angle has a slightly larger magnitude than from the 40^o mean incoming angle. However, the normalized mean breaking wave heights do not have a magnitude difference for the mean incoming wave angles of $\pm 40^o$. Thus, it is the slightly larger magnitude of breaking directions that generates the higher normalized wave powers for negative angles.

In Figure 26 (f), the normalized STD of the alongshore wave power is much larger for negative angles with a strong spike at -5^o. For the small angles, the offshore alongshore wave power is minimal, which causes the dramatic increase in the normalized STD of the alongshore wave power.

In Figure 26 (g), the alongshore mean sediment transport by CERC formula is similar in magnitude for both westward and eastward transport. The peak sediment transport for negative incoming angles is around -40^o. For large angles, the decrease in wave height is more significant than the increase in angle. The alongshore STD sediment transport (Figure 26 (h)) has a similar shape as the alongshore STD of wave directions such that the peak is also centered close to -50^o.

4.4 Shoreline Response for Fire Island

The governing equation for the rate of change of shoreline position, assuming all shoreline change is driven by the standard shoreline continuity equation (i.e. Komar (1998)) is

$$\frac{\partial s}{\partial t} = -\frac{1}{h_*}\frac{\partial Q_l}{\partial y}, \tag{43}$$

in which s is the shoreline position (positive is accretion and negative is erosion), and h_* is the profile depth which equals to the closure depth d_c plus the beach berm height d_b (Hanson and Kraus, 1989). The appropriate values of h_* have been under debate for many years. In this project, h_* is taken to be 20 m.

In Figure 27, the alongshore variation of shoreline change rate as a function of incoming wave angles is presented. It is seen that for waves from the southeast directions (negative angles), the regions of shoreline accretion appear on the left side of the ridge crests, whereas the erosion is on the right. The local maximum of shoreline accretion or erosion is centered around -50^o, which is near the ridge orientation. The difference between the incoming angle containing the local maximum and the ridge orientation is possibly caused by the energy leakage in the extreme angles. It is also shown that there is a slow migration of shoreline accretion to the east towards the ridge crests as incoming waves approach shore normal. The region of accretion switches to the right side of the ridge crests, while erosion is on the left for incoming wave angles less than -10^o and from the west (positive angles). However, the variation of shoreline change rate for waves from the southeast is stronger than the shoreline variation for waves from the southwest.

Figure 28 presents the STD of the rate of shoreline change as a function of incoming wave angles. As seen in this figure, the shoreline change rate STD peaks around -50^o at a little more than 0.8 m/d, whereas the variation for the waves from the west is less than about 0.1 m. Since the dominant wave directions in Fire Island are from the southeast according to the analysis in Chapter 2, the greater change rate STD

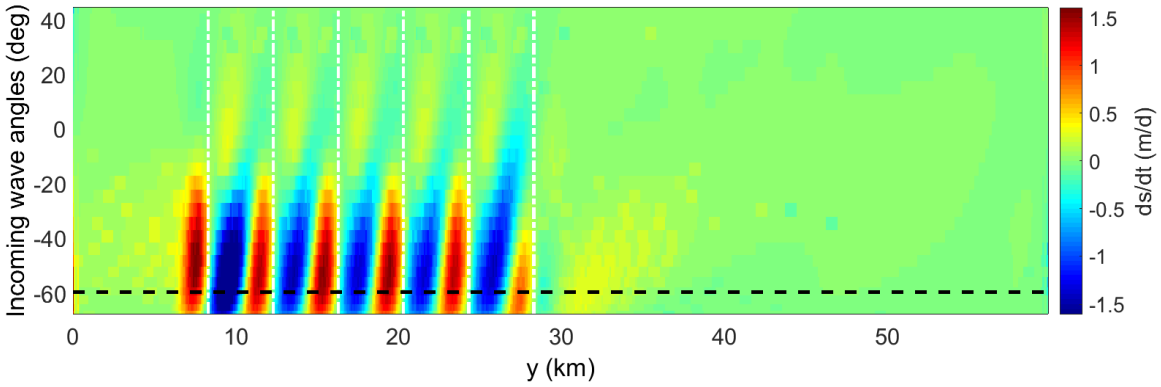

Figure 27: Alongshore variation of shoreline change rates for incoming wave angles from -68^o to 44^o. Black dash line is the angle of the ridges. White dot dash lines indicate the alongshore locations of the ridge crests along the averaged 12-m seabed topography.

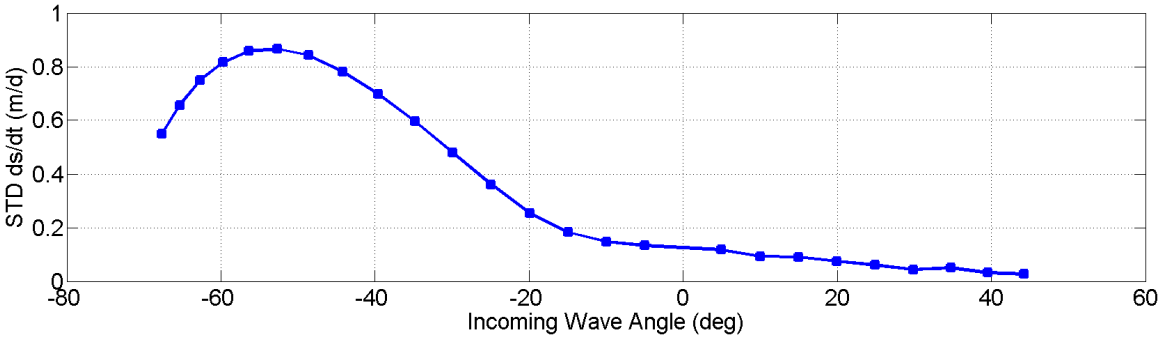

Figure 28: STD of the shoreline change rates for incoming wave angles from -68^o to 44^o.

at negative incoming angles is more relevant to the expected shoreline change rate patterns on Fire Island.

Overall, the pattern still holds that the variation of a wave property is stronger if the incoming wave angle is closer to the ridge orientation. And for waves with incoming from angles greater (smaller) than the ridge orientation, the stronger variation is pushed to the left (right) relative to the location of stronger variation in the case of incoming wave angle equal to ridge orientation.

4.5 Summary

In this chapter, alongshore sediment transport is calculated based on two commonly used empirical equations: the CERC and GENESIS equations. The difference of the sediment transport by these two methods is caused by the alongshore gradient of breaking wave heights. Overall, it is seen that GENESIS yields results which are consistent with the CERC formula, however the wave height gradients do modify the transport, albeit less than the variability induced by the ridges for the CERC equation. Therefore, the CERC formula is targeted as the major method in calculating sediment transport.

As seen with the wave properties, the sediment transport is related to the orientation of ridges as well as the incoming wave angles such that the local maximum of sediment transport is pushed to the left (right) side of the ridge crests for incoming wave angles greater (smaller) than the angle of ridges. This pattern is determined under the combination effect of breaking wave heights and breaking wave directions. Breaking wave directions have stronger impact on the sediment transport for incoming wave angles smaller than the ridge orientation; breaking wave heights, on the other hand, have stronger effect on sediment transport for incoming angles greater than the ridge orientation.

In terms of the effect of incoming wave angles on wave properties and sediment transport for Fire Island where the ridge orientation is -60^o, refraction dominates the magnitude of wave properties in the extreme angles whereas shoaling increases the wave height in the smaller angles. The fluctuation in the sediment transport is stronger in the negative directions than in the positive directions with the peak centered around -50^o, close to the angle of ridges, -60^o.

The standard deviation of shoreline change rate as a function of incoming wave angles presents an increasing rate of shoreline fluctuation in the negative directions with a peak also centered around -50^o. The shoreline change rate of Fire Island

follows a similar pattern that the stronger shoreline change rate is associated with the incoming wave angles closer to the ridge orientation. For incoming wave angles smaller than the ridge orientation, the local maximum of shoreline change rate is pushed slightly to the right relative to the locations of local maximum when the incoming wave angle is equal to the ridge orientation.

CHAPTER V

SENSITIVITY ANALYSIS

This chapter presents a sensitivity analysis on relevant parameters to evaluate the robustness of the conclusions in the previous chapters. These scenarios include smaller waves with a shorter period on the offshore south boundary, activating the dissipation caused by bottom friction and applying a different incoming directional spreading.

5.1 Smaller Waves with Shorter Period

As indicated in the last section of chapter 2, waves as large as 4 m occur less frequently compared to 2 m waves or 1 m waves, which also have a wider range of directions and typically shorter periods such as 9 s. Therefore, the wave conditions at the offshore south boundary are switched from a wave height of 4 m and a period of 12 s to a wave height of 2 m and a period of 9 s. The purpose of implementing these wave conditions at the offshore south boundary is to test if the pattern of higher waves and linkage to the directional difference between the ridge orientation and the mean incoming wave direction still holds. In addition, the wave breaking condition and associated shoreline change is also compared between the two different offshore wave conditions.

The distribution of wave heights for these conditions is similar to the distribution for a 4-m wave height and a 12-s period. The ridge orientation is set to be -30^o so that the results of spectral analysis are comparable with results from chapter 3. Figure 29 presents the transformation of directional spectra along the middle cross-shore section of the domain under the condition of smaller waves with a shorter period. The mean incoming wave angles are -60^o, -30^o and 0^o. Focusing on the topography (white line) and wave height variation (red line) with their alongshore-mean removed,

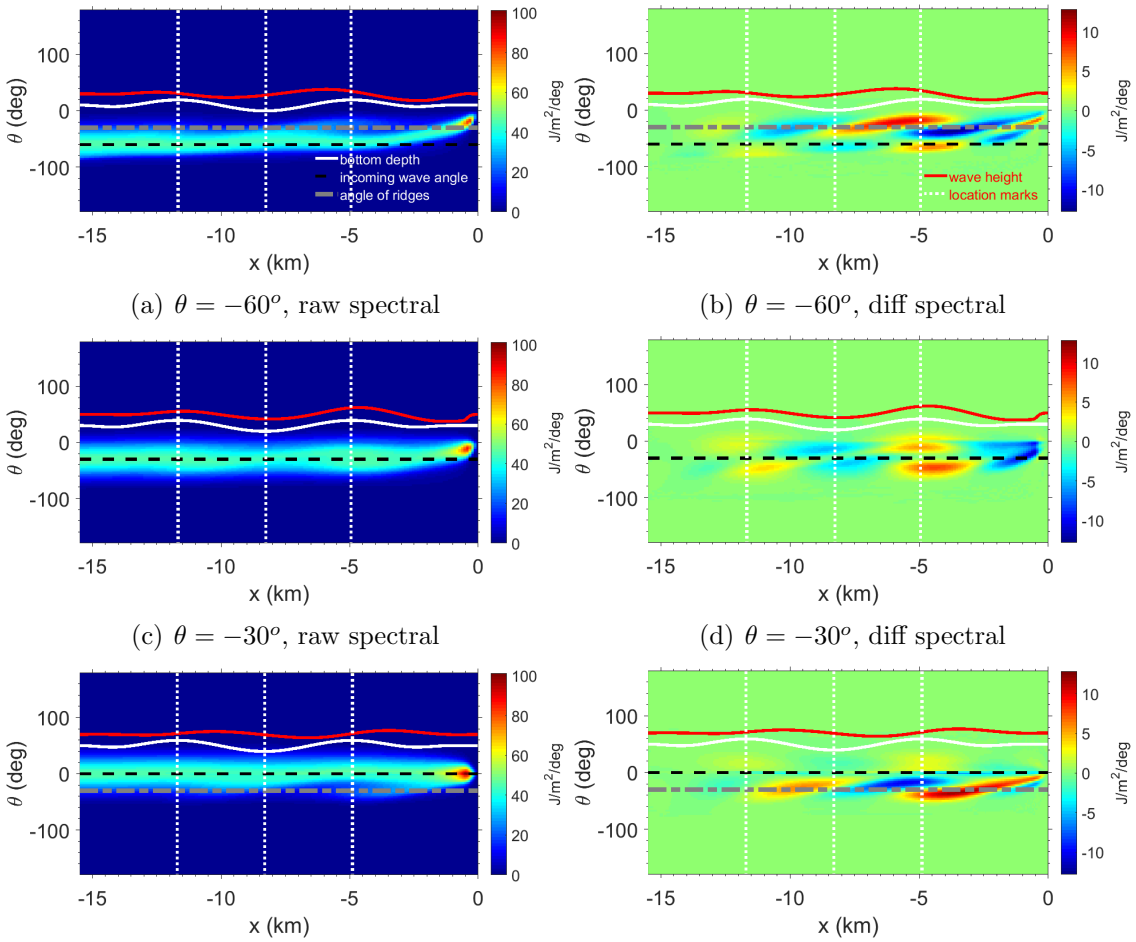

(a) $\theta = -60^o$, raw spectral

(b) $\theta = -60^o$, diff spectral

(c) $\theta = -30^o$, raw spectral

(d) $\theta = -30^o$, diff spectral

(e) $\theta = 0^o$, raw spectral

(f) $\theta = 0^o$, diff spectral

Figure 29: Directional spectra as a function of cross-shore distance along the middle line of the domain (y = 30 km) with mean incoming wave angles (a) $\theta = -60^o$, (c) $\theta = -30^o$ and (e) $\theta = 0^o$. Spectral differences calculated by directional spectra with ridges minus without ridges are shown in (b) $\theta = -60^o$, (d) $\theta = -30^o$ and (f) $\theta = 0^o$. Wave height variation (red) and bathymetric variation (white) are removed by their alongshore mean values.

it is seen that when the mean incoming waves are from southeast but with a more oblique direction than the ridge orientation -60^o (Figure 29 (a)-(b)), wave heights are higher on the left side of the ridge crests. In contrast, when the mean incoming waves are from a normal direction to the shoreline (or a direction smaller than the ridge orientation) as shown in Figure 29 (e)-(f), higher wave heights are on the right side of the ridge crests. When the mean incoming wave angle is equal to the ridge orientation (Figure 29 (c)-(d)), the local maximum of wave heights happens almost on top of the ridge crests.

Focusing on the transformation of directional spectra, it is seen that strong energy fluctuation is associated with the ridge orientation. When the mean incoming wave angle is -60^o, a direction greater than the ridge orientation, increased energy density is maximum on the left side at the ridges around x = - 6 km. Also, negative energy variation is seen to be strong around x = - 4 km on the right side of the ridges. In short, the energy variations correspond closely to the same patterns for the wave height variations. When the mean incoming wave angle is 0^o, the spectral variation is reversed matching the wave height pattern. When the mean incoming wave angle is -30^o, the direction equal to the ridge orientation, the energy density increases across almost the entire span of directional spectra on the ridge crests at x = -5 km, the same area where wave heights are higher. Similarly the energy density decreases across the full range of directions in the ridge troughs.

Comparing to the larger waves in Chapter 3, the pattern of wave propagation and spectral transformation for the smaller waves is highly consistent in pattern but not in magnitude. The magnitude of directional spectra for the larger wave condition can reach to 300 $J/m^2/deg$ along the middle cross-shore section, whereas the magnitude for smaller waves can only reach to 100 $J/m^2/deg$. In terms of the magnitude of the variations, the former wave condition can produce variations up to ± 80 $J/m^2/deg$, whereas the latter can only produce variations up ± 10 $J/m^2/deg$.

In order to investigate the effect of incoming wave angles on wave breaking properties, alongshore sediment transport and shoreline change, the ridge orientation is switched back to -60^o to simulate the Fire Island situation and compare the two different offshore wave conditions. Figure 30 presents the mean (first column) and standard deviation (second column) of breaking wave heights, breaking wave directions, alongshore sediment transport as a function of the mean incoming angles. The breaking wave heights are normalized by the mean wave heights in order to minimize the effect of the spectral leakage. The bottom panel shows the standard deviation of shoreline change rate as a function of the mean incoming angles.

As shown in Figure 30 (a), although the smaller waves propagating in the domain produce lower corresponding breaking wave heights, the normalized breaking wave heights are almost identical to normalized breaking wave heights generated by the larger waves. Under both offshore wave conditions, the mean breaking wave heights are highest when waves propagate from the direction normal to the shoreline and the effect of refraction is the weakest. As the direction of incidence become increasingly oblique, breaking wave heights decrease with increasing effect from refraction.

As presented in Figure 30 (b), the magnitude of STD wave heights is smaller for the smaller waves compared to the larger waves. This decrease in wave height variation is more significant for smaller waves from the southeast (negative) directions. When waves are from the southwest (positive) directions, the difference in wave height variation between smaller and larger waves is much less. Overall, the trend of the wave height variation stays the same for both offshore wave conditions such that the variation of wave heights is stronger for waves from southeast directions compared with waves from southwest directions. This is because waves from the southeast directions, directions closer to the ridge orientation, tend to be strongly affected by the bathymetric variation. The overall reduction in variability for smaller waves is caused by the reduction in refraction by the ridges due to the shorter wave period.

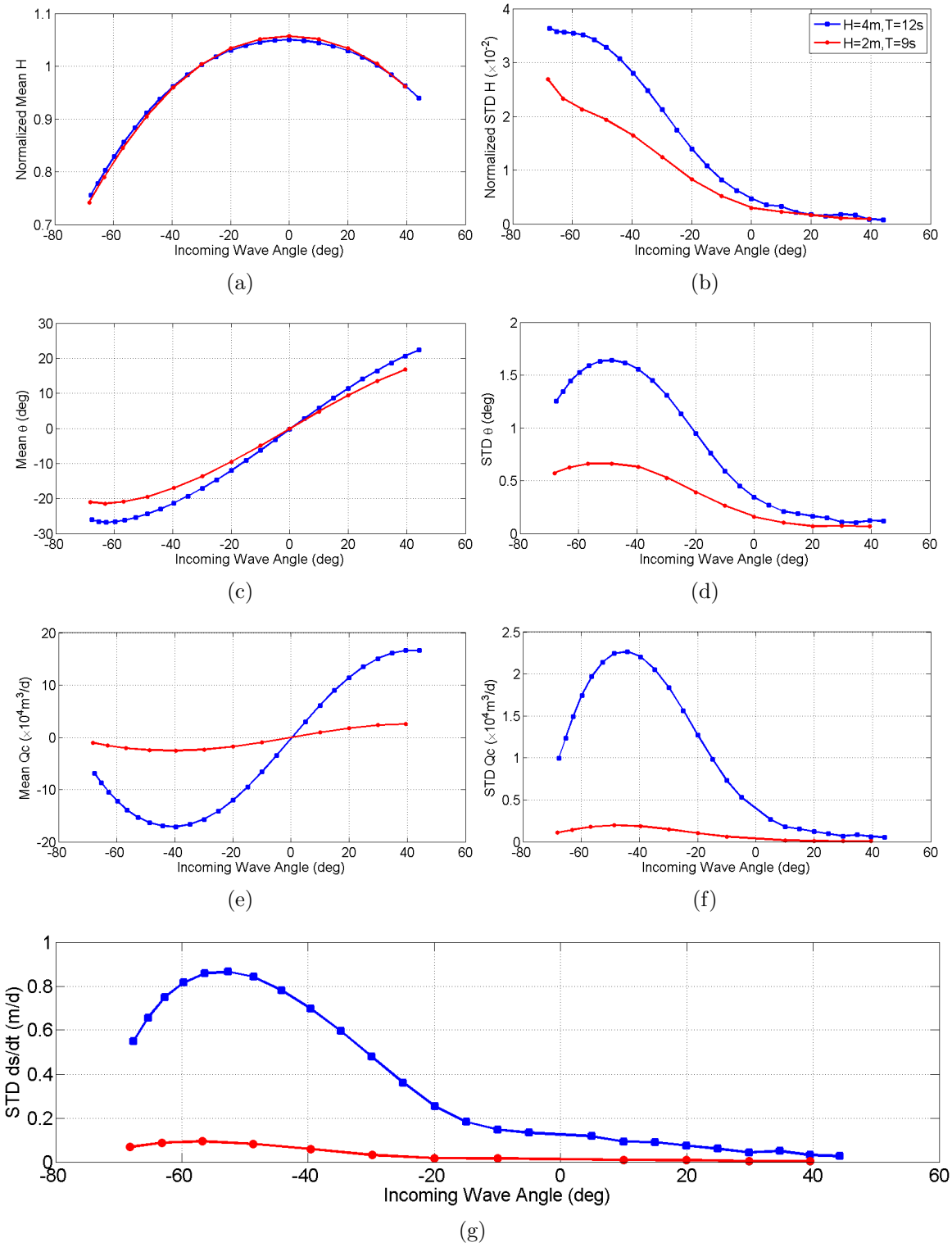

Figure 30: Different properties as a function of mean incoming wave angle. (a) normalized mean breaking wave heights, (b) normalized STD breaking wave heights, (c) mean breaking wave angles, (d) STD breaking wave angles, (e) mean sediment transport by CERC, (f) STD sediment transport by CERC, and (g) STD of the shoreline change rates.

In Figure 30 (c), smaller waves have smaller breaking angles. Although shorter waves have less effect from refraction, these waves also propagate with a smaller wave height and, thus, break at locations closer to shore, causing the breaking angles to decrease.

In Figure 30 (d), the pattern of higher variation in breaking wave angles for waves from southeast (negative) directions and lower variation for waves from southwest (positive) directions is similar for both the 4-m waves and the 2-m waves. The difference is that the magnitude of the variation is much smaller for the 2-m waves. This reduction in magnitude is dramatically significant for the 2-m waves from southeast directions and the peak is flatten out into a fairly wide range of incoming wave angles.

With the much smaller breaking wave heights and breaking directions, the alongshore sediment transport for the 2-m waves is much smaller compared to the transport of the 4-m waves (Figure 29 (e)). This is because the alongshore sediment transport from the CERC equation grows as a power function of breaking wave heights. The consistent part is that for waves from southeast (negative) directions, the alongshore sediment is transported westward (negative), whereas for waves from southwest (positive) directions, the alongshore sediment transport is eastward (positive).

Similarly, the magnitude of the variation of the alongshore sediment transport as well as the shoreline change rate is also dramatically smaller for the 2-m waves with similar sensitivity to the wave direction (Figure 30 (f)-(g)). For the waves from the southeast directions, the variation magnitude is the most significant, which implies that waves from southeast strongly affect the shoreline change rate at Fire Island with larger waves having more of in effect.

In conclusion, smaller waves generate a similar process of spectral transformation and wave propagation resulting in similar patterns of shoreline changes, albeit with much less magnitudes.

5.2 Bottom Friction

All applications so far have been conducted without bottom friction for the purpose of investigating wave refraction and shoaling caused by the bathymetric variations. However, dissipation induced by bottom friction becomes an important wave-bottom interaction as waves propagate into shallow water and the orbital motions of water particles can reach to the bottom, causing the wave heights to decrease prior to wave breaking. Therefore, in this section, the dissipation caused by bottom friction is incorporated as another term in the wave action balance equation to investigate the effect of bottom friction and the variation in wave transformation. The forcing term induced by the bottom friction is expressed by equation (5), in which the bottom friction coefficient C_b is derived using Madsen et al. (1988)'s formulation. Detail formulation for the bottom friction coefficient and the associated application in SWAN is available in Booij et al. (2000). Basically when Madsen et al. (1988)'s formulation is selected, the only input parameter is the bottom roughness length scale, K_N. In this section, K_N is chosen to be the default value, 0.05. With or without friction, the wave conditions at the offshore south boundary are set to have a 4-m wave height and a 12-s wave period. The ridge orientation is -60^o.

In Figure 31, the wave heights and wave directions are presented along the middle cross-shore section of the domain for both bottom friction included and excluded. The incoming wave angle is -30^o to avoid the leakage problem for the more oblique incidence waves. In Figure 31 (a), when bottom friction is not included, waves start to propagate with a 4-m wave height at the offshore boundary, fluctuate between increasing and decreasing wave heights, and break when reaching the threshold for wave breaking. The wave height is generally fluctuating before breaking around 4 m. However, when bottom friction is included, wave heights are generally decreasing although still fluctuating due to the ridges. Because waves are continuously dissipated during propagation, the wave heights are smaller and they break further inshore.

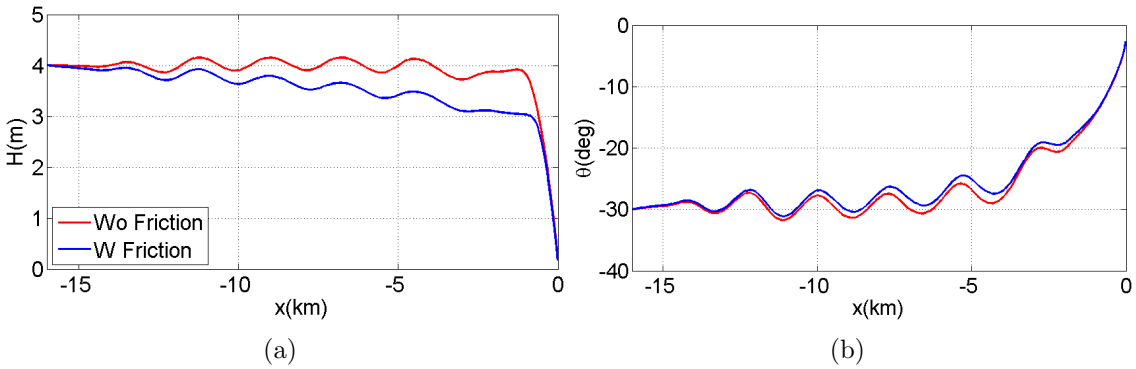

(a) (b)

Figure 31: Cross-shore sections at y = 30 km for bottom friction excluded (red) and included (blue) of (a) wave height and (b) wave direction.

In Figure 31 (b), with or without bottom friction, waves start from an offshore direction of -30^o, propagate and refract to a smaller angle relative to shore normal, and finally become perpendicular to the shoreline. The difference in wave directions for bottom friction included or excluded is small.

In order to further evaluate the effect of bottom friction, the mean (first column) and standard deviation (second column) of breaking wave heights, breaking wave directions, and alongshore sediment transport are presented in Figure 32. The breaking wave heights are normalized and standard deviation of shoreline change rate is presented at the bottom.

As shown in Figure 32 (a), the alongshore mean breaking wave heights become much smaller when bottom friction is activated. Whether the incoming waves are from southeast or southwest, the magnitude of decrease in normalized mean wave heights is nearly the same. This indicates that a strong decrease in wave heights is introduced by bottom friction.

As shown in Figure 32 (b), with or without bottom friction, the variation of wave heights is stronger when waves are from southeast and weaker when waves are from southwest. The difference is that, when bottom friction is activated, the variation of wave heights decreases for all incoming directions. This decrease is more significant when waves are from southeast. This indicates that bottom friction reduces the

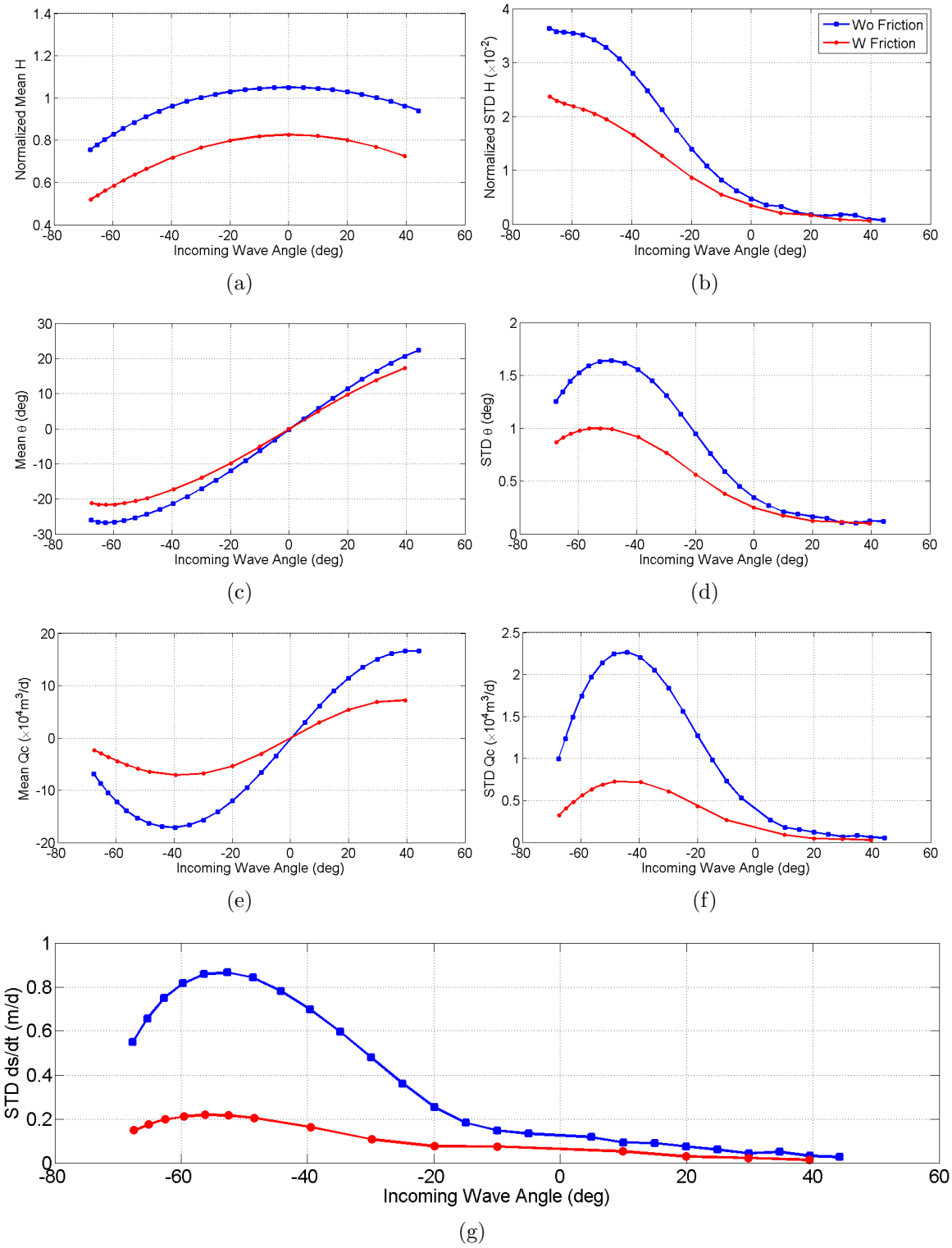

Figure 32: Different properties as a function of mean incoming wave angle. (a) normalized mean breaking wave heights, (b) normalized STD breaking wave heights, (c) mean breaking wave angles, (d) STD breaking wave angles, (e) mean sediment transport by CERC, (f) STD sediment transport by CERC, and (g) STD of the shoreline change rates.

alongshore variation of wave heights.

In Figure 32 (c), with or without bottom friction, the breaking wave directions are larger for waves with more oblique incoming angles. The effect of bottom friction on the breaking angles is through the reduction in wave heights, which causes waves to propagate further inshore before breaking. Therefore, when bottom friction is included, the breaking wave directions are smaller.

In Figure 32 (d), although under both conditions the variation of breaking directions is stronger for waves from southeast (negative directions), this variation becomes smaller when bottom friction is included. The decrease is more significant for waves from southeast.

In Figure 32 (e), alongshore sediment transport reaches a maximum for the incoming directions of $\pm 40^o$. When bottom friction is included, there is a reduction in the mean alongshore sediment transport, which results from the combination of smaller breaking wave heights and directions.

As shown in both Figure 32 (f) and (g), bottom friction dramatically decreases the variation in alongshore sediment transport and in shoreline change rate, although the dependence on incoming wave direction remains the same.

In summary, although the overall pattern is similar whether bottom friction is included or not, the magnitudes of the variations of breaking wave properties, alongshore sediment transport and shoreline change rate become smaller.

5.3 Directional Spreading

For the spectral wave model, parameters such as directional spreading (the one-sided directional width of the spectrum in SWAN) can be quite important and generate distinctive spectral transformation patterns. Thus, it is necessary to evaluate the effect of spectra with a different directional spreading. The new directional spreading is 10^o in this section as opposed to 20^o in the previous chapters. The ridge orientation

is -60^o.

Figure 33 presents the mean (first column) and standard deviation (second column) of breaking wave heights, breaking wave directions, alongshore sediment transport for directional spreading of 20^o and 10^o. The breaking wave heights are normalized and standard deviation of shoreline change rate is presented at the bottom.

As seen in Figure 33 (a), when the directional spreading is 10^o instead of 20^o, the alongshore averaged breaking wave heights increase for a wide range of incoming directions. For waves from an oblique angle greater than -60^o, the breaking wave heights for the two different directional spreadings are the same.

From Figure 33 (c), it is seen that when directional spreading is smaller, the breaking wave directions increase. The increase becomes more significant when the incoming waves are from a more oblique angle.

Due to the higher breaking wave heights and larger breaking directions, the alongshore sediment transport also increases as shown in Figure 33 (e). Similar to the breaking wave directions pattern, the increase in alongshore sediment transport is more obvious for more oblique waves.

As for the variation (Figure 33 (b), (d) and (f)), it is intriguing to note that, comparing the directional spreading of 10^o to 20^o, the variations in breaking wave heights, breaking wave directions and alongshore sediment transport are larger for waves from angles more oblique than -30^o. Furthermore, the variations are smaller compared with the directional spreading of 20^o for incoming wave directions smaller than -30^o. However, this decrease becomes insignificant for waves from the southwest.

A similar pattern is shown in the variation of shoreline change rate in Figure 33 (g). The exception is that, within the range of -20^o and 0^o, the shoreline change rate for the directional spreading of 10^o is higher compared with the directional spreading of 20^o.

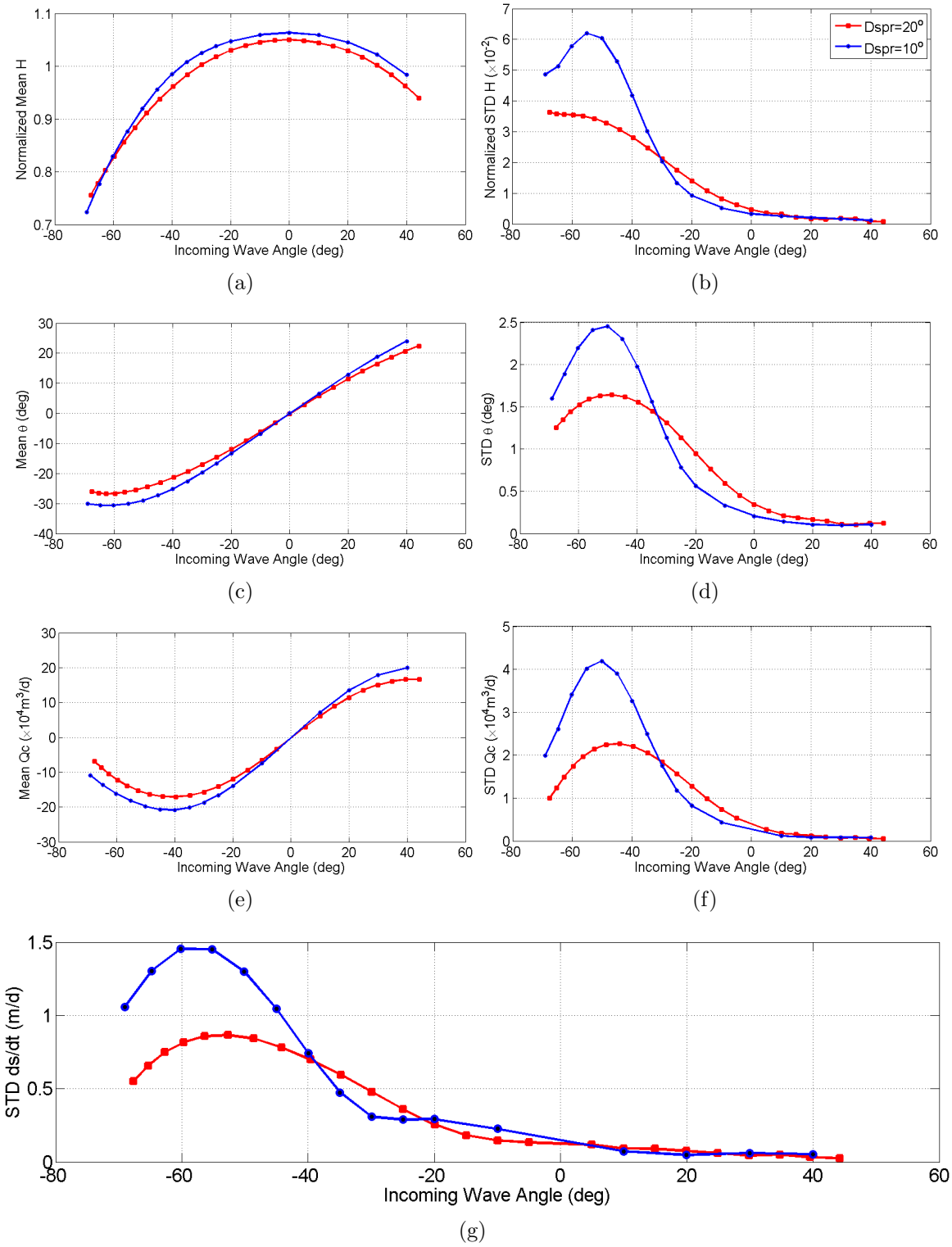

Figure 33: Different properties as a function of mean incoming wave angle. (a) normalized mean breaking wave heights, (b) normalized STD breaking wave heights, (c) mean breaking wave angles, (d) STD breaking wave angles, (e) mean sediment transport by CERC, (f) STD sediment transport by CERC, and (g) STD of the shoreline change rates.

Given the quite distinctive pattern described above, a spectral analysis is necessary for understanding the effect of directional spreading and the explaining the variation in wave properties. The spectral evolution along the middle cross-shore section of the domain is needed for both directional spreading of 10^o and 20^o. The chosen incoming wave directions are -50^o, -20^o and 30^o, corresponding to the highest increase, decrease and a typical angle from the southwest, respectively.

Figure 34 presents the directional spectra for directional spreading of 10^o and 20^o for the incoming wave direction of -50^o. When the directional spreading is 10^o (Figure 34 (a)), the directional spectrum is narrow banded near the offshore boundary. As waves propagate over the ridge field, the directional spectrum is spread over a broader range compared with its initial state. The broadening and narrowing pattern over the ridges is highly consistent between the two cases (Figure 34 (b)). The difference is that the directional spectrum has larger energy density magnitude for directional spreading of 10^o.

Looking at the spectra with alongshore mean removed (Figure 34 (c) and (d)), it is seen that the magnitude of the variation is stronger for the directional spreading of 10^o. This is because smaller directional spreading will have higher energy density around the mean wave angle. When the mean wave angle is close to the ridge orientation, more waves with high energy density are trapped and refracted towards the ridges and, thus, the stronger variation is generated. This stronger variation in directional spectra also produces higher wave height variations.

Consequently, the behavior behind larger variations associated with incoming directions more oblique than -30^o in Figure 33 depends on two conditions. The first is that the directional spreading is smaller. The second is that the incoming wave angle is close enough to the ridge orientation (within the span of the directional spectrum for that particular directional spreading). With these two conditions, more energetic waves are trapped and refracted towards the ridges, producing large variations in

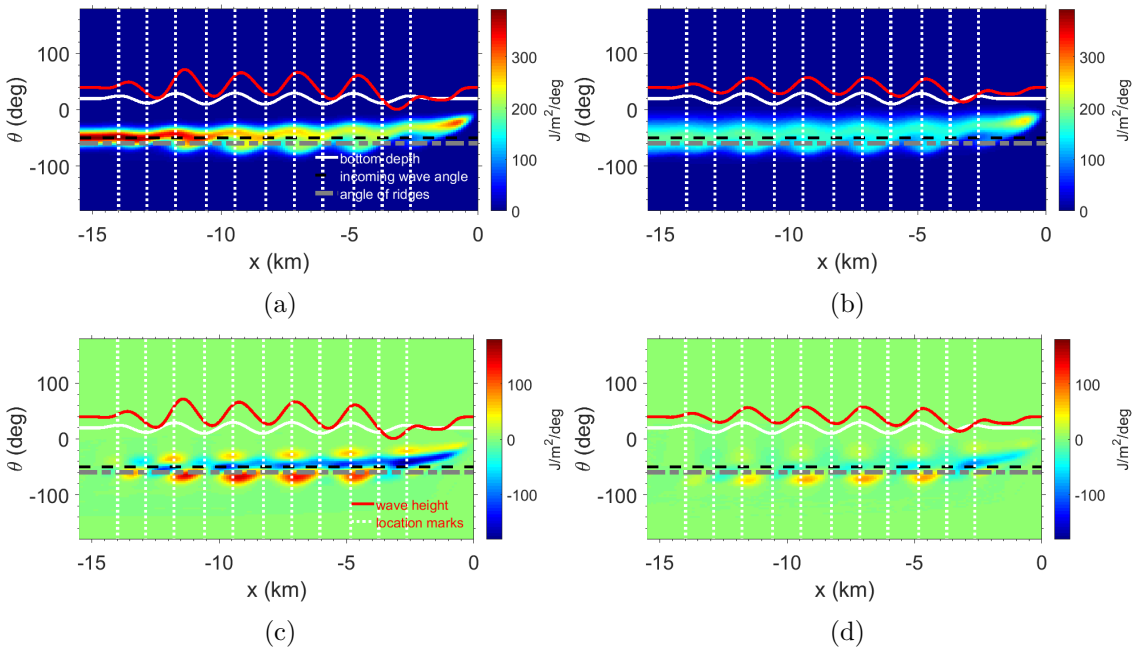

Figure 34: Directional spectra as a function of cross-shore distance along the middle line of the domain (y = 30 km) with directional spreading of (a) 10^o and (b) 20^o. Spectral differences calculated by directional spectra with ridges minuses without ridges are shown with directional spreading of (c) 10^o and (d) 20^o. Mean incoming wave angle is -50^o. Wave height variation (red) and bathymetric variation (white) are removed by their alongshore mean values.

wave properties.

Figure 35 presents the directional spectra for the incoming wave direction of -20^o. When the directional spreading is 10^o (Figure 35 (a)), the mean incoming wave angle has 40^o difference from the ridge orientation. Therefore, energetic waves are no longer affected by the ridges. The evolution of directional spectra caused by ridges is insignificant and, thus, the narrow-banded shape is maintained. However, when the directional spreading is 20^o (Figure 35 (b)), the directional spectrum has a wider directional range initially and some of the energetic waves in the spectrum are trapped around the ridge orientation.

This pattern is more obvious in Figure 35 (c) and (d). In Figure 35 (c), it is seen that the variation in directional spectra is centered around the incoming wave angle and basically no variation is captured at the ridge orientation. In contrast, in Figure

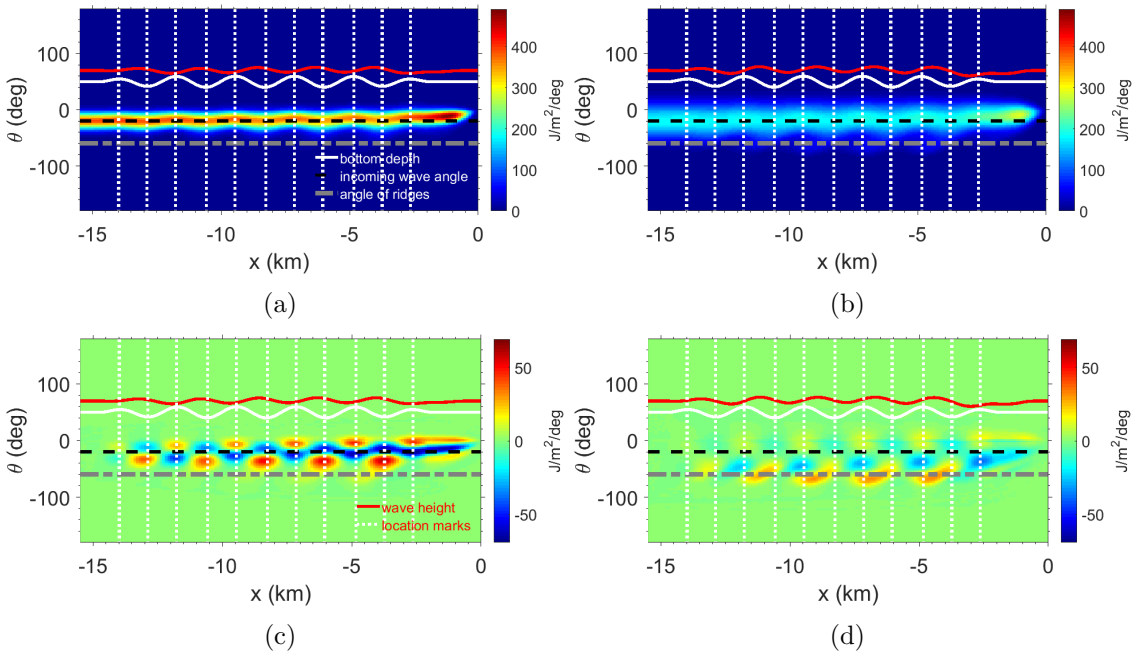

Figure 35: Directional spectra as a function of cross-shore distance along the middle line of the domain (y = 30 km) with directional spreading of (a) 10^o and (b) 20^o. Spectral differences calculated by directional spectra with ridges minuses without ridges are shown with directional spreading of (c) 10^o and (d) 20^o. Mean incoming wave angle is -20^o. Wave height variation (red) and bathymetric variation (white) are removed by their alongshore mean values.

35 (d), there is significant positive energy variation around the ridge orientation. As a result, for the directional spreading of 20^o, part of the energy is transfered to directions close to ridge orientation, causing the local maximum of wave heights to be closer to the ridge crests and the variation of wave height to be slightly higher.

This provides an explanation to the reduction in variability of wave properties for the smaller directional spreading within the range of incoming directions from -30^o to 0^o as shown in Figure 33. Directional spectra with the smaller directional spreading do not have energetic waves affected by the ridges, whereas a significant portion of the directional spectra with the larger directional spreading is still trapped around the ridge orientation, leading to more variability.

Finally, when the incoming wave angle is 30^o (Figure 36), for both directional

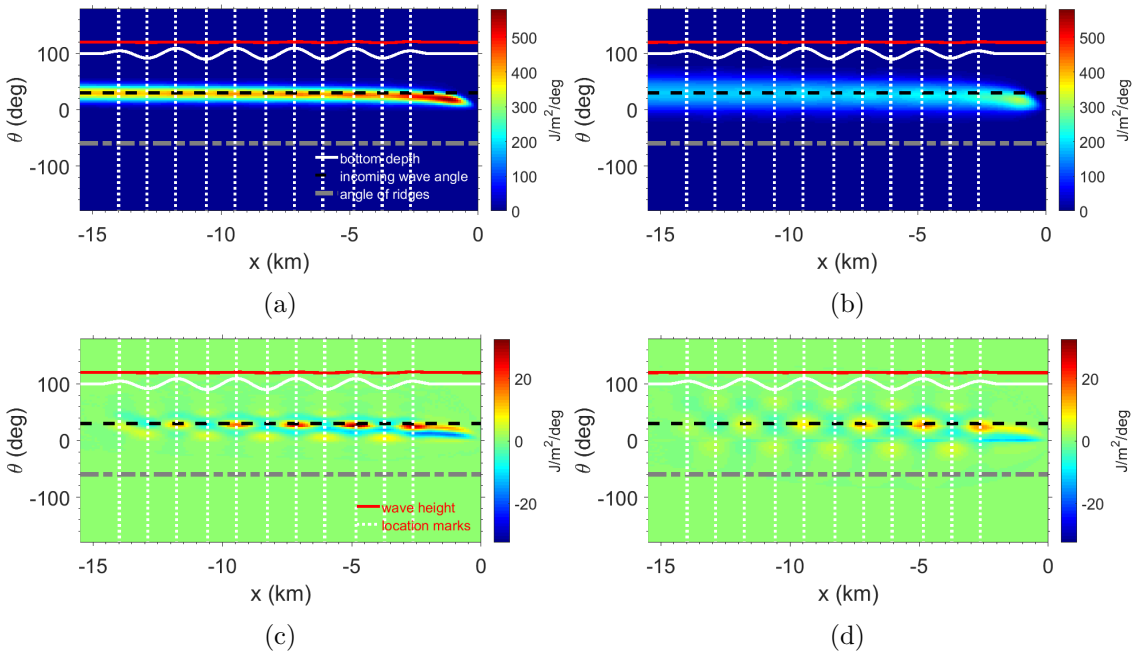

Figure 36: Directional spectra as a function of cross-shore distance along the middle line of the domain (y = 30 km) with directional spreading of (a) 10^o and (b) 20^o. Spectral differences calculated by directional spectra with ridges minuses without ridges are shown with directional spreading of (c) 10^o and (d) 20^o. Mean incoming wave angle is 30^o. Wave height variation (red) and bathymetric variation (white) are removed by their alongshore mean values.

spreadings, the energetic portions of the spectra are far away from the ridge orientation. Therefore, the directional spectra for both directional spreading of 10^o and 20^o maintain their originally narrow-banded and broad-banded shape, respectively, without the interference of ridges. The corresponding wave height variations are both small, which explains the similarity in wave properties for incoming directions greater than 20^o in Figure 33.

5.4 Summary

This chapter presents the sensitivity analysis for three different aspects of the wave field. They are to evaluate the effect of (a) a smaller wave height and a shorter period, (b) the incorporation of bottom friction, and (c) a narrow directional spreading.

It is shown that the wave height distribution is related to the relative difference

between incoming wave angles and ridge orientation, whether the waves are small or large. Higher wave heights appear on the left (right) side of the ridge crests, when incoming wave angles are larger (smaller) than the ridge orientation. Another conclusion is that smaller waves with a shorter period at the offshore boundary results in smaller breaking wave heights and, hence, less corresponding alongshore sediment transport and shoreline change rate variability.

As for the study of the incorporation of bottom friction, it is shown that bottom friction decreases the wave heights as the wave propagate shoreward, causing waves to break further inshore with smaller breaking wave heights and smaller breaking wave directions. Thus, the corresponding alongshore sediment transport and shoreline change rate are also reduced. The magnitude of variation also decreases.

When waves are propagating with a smaller directional spreading, it is seen that the variations in breaking wave heights, breaking wave directions, alongshore sediment transport and shoreline change rate are stronger (weaker) for incoming waves with a more oblique (normal) angle from the southeast directions. The waves associated with portion of the directional spectrum near the ridge orientation tend to get trapped leading to wave focusing and defocussing and hence variability in the wave properties. Therefore, the cases for the narrow directional spreading has more energy trapped when the mean direction is close to the ridge orientation. Because more energy is refracted from the directional spectra with a smaller directional spreading, the variation is stronger. In contrast, for waves from the more normal angles, less energy is trapped under the effect of ridges if the smaller directional spreading is implemented, whereas with the broad direction spreading a portion of the spectra is partially trapped by the ridges.

Overall, while the results do change in magnitude or in variation pattern depending on the aspect of wave field analyzed, the general conclusions are consistent with previous chapters.

CHAPTER VI

CONCLUSIONS

Waves, propagating across the inner continental shelf near Fire Island, NY, are dynamically interacting with its complex topography, which is characterized by a series of obliquely oriented shoreface-connected ridges. Due to the existence of these ridges, the pattern of wave transformation is profoundly modified, inducing a unique distribution of sediment transport and further influencing the bathymetric evolution, along with long and short term shoreline change. Although wave propagation and the corresponding variation of sediment transport has been under investigation for years, the effect of the shoreface-connected ridges remained unclear. In order to isolate and identify the ridges-inducing wave transformation and sediment transport pattern, these processes are investigated by utilizing the wave model SWAN, forced with realistic wave conditions, on a simplified, synthetic bathymetry replicating the scales of the shoreface-connected ridges.

The model setup, including the generation of synthetic bathymetry, the implementation of a nonuniform grid and the configuration of forcing and input, was illustrated in Chapter 2. In particular, the synthetic bathymetry is characterized by a smooth sloping bottom with a series of 2-m amplitude and 2-km width ridges oriented 60^o in the counterclockwise direction. The grid is a constant of 100 m in the alongshore direction and nonuniform with an increasing resolution from 100 m to 10 m from the offshore boundary to the shoreline. By investigating the historic wave data from the NDBC buoy 44094 and buoy 44025, it is shown that waves, especially large waves, happened more frequently from the southeast direction.

In Chapter 3, the effect of ridges on wave transformation was analyzed extensively. The variations in the wave field are much stronger when the predominant wave direction is along the ridges rather than perpendicular to the ridge crests, which is explained by the stronger bathymetric gradient along the direction of ridges. Furthermore, a reverse ray-tracing technique is utilized to trace the origin of waves inside the domain back to where they start to propagate. By using this ray-tracing technique and evaluating the energy spectra, it is shown that the variations in the energy spectra are caused by the relative angle between the mean incoming wave direction and ridge orientation.

For the energy spectrum at the offshore boundary, the highest energy is associated with the mean incoming wave angle. When the mean incoming wave angles are close to the ridge orientation, more energy can be trapped. If the origin of waves has a direction further away from the mean incoming wave angles, low energy carried by these incoming waves can be transfered to the particular location. Since the spectrum is composed of energy carried by waves from the entire span of directions, if, for a certain location inside the domain, more waves are refracted from an incoming direction containing high (low) energy, the resulting wave heights will be increasing (decreasing).

Thus, it is seen that ridges trap waves that are within $\pm 15^o$ of the direction of ridges. More importantly, the local maximum of wave heights are produced on the opposite side of the ridge crest relative to the incoming wave direction, since more energy are trapped on the left (right) side of ridges when the mean incoming waves are from a direction more oblique (normal) than the ridge orientation.

In Chapter 4, the effect of ridges on alongshore sediment transport and shoreline response was investigated using empirical CERC and GENESIS equations and the continuity equation governing shoreline change. The GENESIS equation yields results which are consistent with the CERC equation, however the wave height gradients do

modify the transport, albeit less than the variability induced by the ridges for the CERC equation.

Similar to the pattern of wave properties, the behaviors of the alongshore sediment transport as well as the shoreline change are also related to the difference between the orientation of ridges and the mean incoming wave angles. Firstly, the stronger variation of the alongshore sediment transport and shoreline change is associated with the mean incoming wave angles close to the ridge orientation. Secondly, the local maximum of alongshore sediment transport is on the left (right) side of the ridge crests for mean incoming wave angles greater (smaller) than the angle of ridges.

Although the overall alongshore distribution of breaking wave heights and breaking wave directions is consistent with the alongshore sediment transport, their effect on the alongshore sediment transport depends on the mean incoming angles. Separated by the ridge orientation, the breaking wave heights have stronger influence on alongshore sediment transport with more oblique incoming wave directions and the breaking wave directions have larger impact on more normal incoming directions. All together, the pattern of alongshore sediment transport is determined by the distribution of breaking wave heights and breaking wave directions. The magnitude of the shoreline change is stronger for incoming waves from the southeast, which also has a higher recurrence frequency and a higher associated wave height in the nearshore region of Fire Island. Thus, if the predominant waves are from southwest, there is minimal shoreline change.

In Chapter 5, a sensitivity analysis was presented on relevant parameters to evaluate the robustness of the conclusions in the previous chapters. These parameters include implementing smaller incoming wave heights with a shorter period, activating the dissipation caused by bottom friction and applying a different incoming directional spreading. For the first and second sensitivity tests, results indicate that the patterns

of wave properties, alongshore sediment transport and shoreline response are consistent with the conclusions from the previous chapters, only with smaller magnitude caused by the reduction of variability due to the smaller incoming wave condition and dissipation through bottom friction, respectively.

For the third sensitivity test, the incoming spectrum has a narrower directional spreading. If the total energy is a constant at the beginning of wave propagation, a narrower directional spreading will result in higher energy associated with the mean incoming wave angle. Therefore, when the mean incoming wave direction is close to the ridge orientation, more energy is trapped around the ridges causing stronger wave variation. Also, the broader directional spreading will interact with the ridges for a greater range of mean incoming wave directions. So there is a small range in which waves are still affected and trapped around the ridge orientation for the broader directional spreading, while they are no longer under the effect of ridges if a narrower directional spreading is implemented for the same mean incoming directions. As a result, the variability of wave properties is reduced when the incoming waves with a narrow directional spreading has little energy in the directions within $\pm 15^o$ of the ridge orientation. Overall, although the differences exist, the conclusion from the previous chapters are still applicable for the range of values for these parameters.

The unique contributions of this research are:

- The effect of shoreface-connected ridges on wave transformation, alongshore sediment transport and shoreline changes is identified through a simplified and synthetic bathymetry without the interference of external forcing and noisy and complex topographic variation.

- Ridges are capable of amplifying the alongshore variation of wave properties if incoming waves are from the directions close to the ridge orientation. This amplified variation is accompanied with corresponding changes in energy spectra.

- Shoreline change is sensitive to the incoming wave directions such that the magnitude is higher for incoming waves from southeast.

Additional research that can be done to improve the results of this study is to perform the same types of analysis on the SWAN and ROMS coupled model, where currents are included and interacting with waves. When currents induced by alongshore pressure gradients are included, it is important to analyze whether the alongshore pattern of sediment transport matches the results from CERC or GENESIS equations. Furthermore, using the guidance from the present work on the effect of ridges to evaluate the results on the realistic Fire Island bathymetry from numerical simulations will be made easier. It may also be useful to analyze other coasts containing similar shoreface-connected ridges in their adjacent continental shelf.

REFERENCES

Abbott, M., Damsgaard, A., and Rodenhuis, G. System 21,jupiter(a design system for two-dimensional nearly-horizontal flows). *Journal of Hydraulic Research*, 11(1): 1–28, 1973.

Allen, J. and LaBash, C. Measuring shoreline change on fire island. *Maritimes*, 39 (1):13–16, 1997.

Allersma, E. Mud on the oceanic shelf off guiana. In *Symposium on Investigations and Resources of the Caribbean Sea and Adjacent Regions, UNESCO, Paris*, pages 193–203, 1971.

Battjes, J. and Janssen, J. Energy loss and set-up due to breaking of random waves. *Coastal Engineering Proceedings*, 1(16), 1978.

Batton, B. Morphologic typologies and sediment budget for the ocean shoreline of long island, new york. stony brook, new york: State university of new york at stony brook. *Marine Sciences Research Center, Ph. D. dissertation, 116p*, 2003.

Beji, S. and Battjes, J. Experimental investigation of wave propagation over a bar. *Coastal Engineering*, 19(1):151–162, 1993.

Beji, S. and Battjes, J. Numerical simulation of nonlinear wave propagation over a bar. *Coastal Engineering*, 23(1):1–16, 1994.

Belibassakis, K., Athanassoulis, G., Gerostathis, T. P., and Katsardi, V. Transformation of wave conditions in nearshore and coastal areas by a 3d coupled-mode wave model. In *15th International Congress of the International Maritime Association of the Mediterranean, IMAM 2013*, 2013.

Blake, E. S., Kimberlain, T. B., Berg, R. J., Cangialosi, J., and Beven II, J. L. Tropical cyclone report: Hurricane sandy. *National Hurricane Center*, 12:1–10, 2013.

Booij, N., Ris, R., and Holthuijsen, L. H. A third-generation wave model for coastal regions: 1. model description and validation. *Journal of Geophysical Research: Oceans (1978–2012)*, 104(C4):7649–7666, 1999.

Booij, N., Haagsma, I., Kieftenburg, A., and Holthijsen, L. Swan technical manual, 2000.

Bouws, E. and Komen, G. On the balance between growth and dissipation in an extreme depth-limited wind-sea in the southern north sea. *Journal of Physical Oceanography*, 13(9):1653–1658, 1983.

Buonaiuto Jr, F. S., Slattery, M., and Bokuniewicz, H. J. Wave modeling of long island coastal waters. *Journal of Coastal Research*, 27(3):470–477, 2011.

Burgers, G. A guide to the nedwam wave model. 1990.

Byrne, R. J. Field occurrences of induced multiple gravity waves. *Journal of Geophysical Research*, 74(10):2590–2596, 1969.

Cardone, V., Pierson, W., Ward, E., et al. Hindcasting the directional spectra of hurricane generated waves. In *Offshore Technology Conference*. Offshore Technology Conference, 1975.

CERC. Shore protection manual. *Army Engineer Waterways Experiment Station, Vicksburg, MS. 2v*, pages 37–53, 1984.

CETN, I. Coastal engineering technical note. 1994.

Check, L. A. Analysis of longshore sediment transport on beaches, 2004.

Christensen, E. D. *Turbulence in breaking waves-A numerical investigation*. PhD thesis, Technical University of DenmarkDanmarks Tekniske Universitet, Department of Hydrodynamics and Water ResocurcesStrømningsmekanik og Vandressourcer, 1998.

Clancy, R., Kaitala, J., and Zambresky, L. The fleet numerical oceanography center global spectral ocean wave model. *Bulletin of the American Meteorological Society*, 67(5):498–512, 1986.

Collins, J. I. Prediction of shallow-water spectra. *Journal of Geophysical Research*, 77(15):2693–2707, 1972.

Dalrymple, R. A. and Dean, R. G. *Water wave mechanics for engineers and scientists*. Prentice-Hall, 1991.

Dattatri, J., Raman, H., and Shankar, N. J. Performance characteristics of submerged breakwaters. *Coastal Engineering Proceedings*, 1(16), 1978.

del Valle, R., Medina, R., and Losada, M. A. Dependence of coefficient k on grain size. *Journal of waterway, port, coastal, and ocean engineering*, 119(5):568–574, 1993.

Drouin, A. and Ouellet, Y. Experimental study of immersed plates used as breakwaters. *Coastal Engineering Proceedings*, 1(21), 1988.

Duane, D. B., Field, M. E., Meisburger, E. P., Swift, D. J., and Williams, S. J. Linear shoals on the atlantic inner continental shelf, florida to long island. *IN: SHELF SEDIMENT TRANSPORT: PROCESS AND PATTERN*, 1972.

Eldeberky, Y. *Nonlinear transformation of wave spectra in the nearshore*. TU Delft, Delft University of Technology, 1996.

Eldeberky, Y. and Battjes, J. Parameterization of triad interactions in wave energy models. 1995.

Elgar, S., Guza, R., Raubenheimer, B., Herbers, T., and Gallagher, E. L. Spectral evolution of shoaling and breaking waves on a barred beach. *Journal of Geophysical Research: Oceans (1978–2012)*, 102(C7):15797–15805, 1997.

Eshleman, J. L., Barnard, P. L., Erikson, L. H., and Hanes, D. M. Coupling alongshore variations in wave energy to beach morphologic change using the swan wave model at ocean beach, san francisco, ca. In *10th International Workshop on Wave Hindcasting and Forecasting (Oahu, Hawaii), Paper F*, volume 4, page 20p, 2007.

Ewing, J. A numerical wave prediction method for the north atlantic ocean. *Deutsche Hydrografische Zeitschrift*, 24(6):241–261, 1971.

Gravens, M. B. Periodic shoreline morphology, fire island, new york. Technical report, DTIC Document, 1999.

Gravens, M. B., Kraus, N. C., and Hanson, H. Gensis: Generalized model for simulating shoreline change. report 2. workbook and system user's manual. Technical report, DTIC Document, 1991.

Group, T. W. The wam model-a third generation ocean wave prediction model. *Journal of Physical Oceanography*, 18(12):1775–1810, 1988.

Haas, K. A. and Hanes, D. M. Process based modeling of total longshore sediment transport. *Journal of Coastal Research*, pages 853–861, 2004.

Hanson, H. Genesis- a generalized shoreline change numerical model for engineering use. *Report no. 1007*, pages 1–27, 1987.

Hanson, H. and Kraus, N. C. Genesis: Generalized model for simulating shoreline change. report 1. technical reference. Technical report, DTIC Document, 1989.

Hapke, C. J., Lentz, E. E., Gayes, P. T., McCoy, C. A., Hehre, R., Schwab, W. C., and Williams, S. J. A review of sediment budget imbalances along fire island, new york: can nearshore geologic framework and patterns of shoreline change explain the deficit? *Journal of Coastal Research*, pages 510–522, 2010.

Hasselmann, K. On the non-linear energy transfer in a gravity-wave spectrum. *J. Fluid Mech*, 12(15):481–500, 1962.

Hasselmann, K. On the spectral dissipation of ocean waves due to white capping. *Boundary-Layer Meteorology*, 6(1-2):107–127, 1974.

Hasselmann, K., Barnett, T., Bouws, E., Carlson, H., Cartwright, D., Enke, K., Ewing, J., Gienapp, H., Hasselmann, D., Kruseman, P., et al. Measurements of wind-wave growth and swell decay during the joint north sea wave project (jonswap). Technical report, Deutches Hydrographisches Institut, 1973.

Hasselmann, S. and Hasselmann, K. Computations and parametrizations of the nonlinear energy transfer in a gravity-wave spectrum. i: A new method for efficient computations of the exact nonlinear transfer integral. *Journal of Physical Oceanography*, 15(11):1369–1377, 1985.

Hayes, M. O. and Nairn, R. B. Natural maintenance of sand ridges and linear shoals on the us gulf and atlantic continental shelves and the potential impacts of dredging. *Journal of Coastal Research*, pages 138–148, 2004.

Hoogendoorn, E. L. and Dalrymple, R. W. Morphology, lateral migration, and internal structures of shoreface-connected ridges, sable island bank, nova scotia, canada. *Geology*, 14(5):400–403, 1986.

Houbolt, J. Recent sediments in the southern bight of the north sea. *Geologie en mijnbouw*, 47(4):245–273, 1968.

Hubertz, J. M. *User's guide to the Wave Information Studies (WIS) wave model, Version 2.0*, volume 27. US Army Engineer Waterways Experiment Station, 1992.

Hughes, S. A. and Jensen, R. E. A user's guide to shalwv: Numerical model for simulation of shallow-water wave growth, propagation, and decay. Technical report, DTIC Document, 1986.

Jabbari, M. H., Ghadimi, P., Sayehbani, M., and Reisinezhad, A. A unique finite element modeling of the periodic wave transformation over sloping and barred beaches by beji and nadaoka's extended boussinesq equations. *The Scientific World Journal*, 2013, 2013.

Janssen, P. A. Wave-induced stress and the drag of air flow over sea waves. *Journal of Physical Oceanography*, 19(6):745–754, 1989.

Janssen, P. A. Quasi-linear theory of wind-wave generation applied to wave forecasting. *Journal of Physical Oceanography*, 21(11):1631–1642, 1991.

Johnson, J. W., Fuchs, R. A., and Morison, J. R. The damping action of submerged breakwaters. *Eos, Transactions American Geophysical Union*, 32(5):704–718, 1951.

Kamath, A., Bihs, H., Chella, M. A., and Arntsen, Ø. A. Cfd simulations of wave propagation and shoaling over a submerged bar. *Aquatic Procedia*, 4:308–316, 2015.

Kana, T. W. A mesoscale sediment budget for long island, new york. *Marine Geology*, 126(1):87–110, 1995.

Kana, T. W., Rosati, J. D., and Traynum, S. B. Lack of evidence for onshore sediment transport from deep water at decadal time scales: Fire island, new york. *Journal of Coastal Research*, pages 61–75, 2011.

Kojima, H., Ijima, T., and Yoshida, A. Decomposition and interception of long waves by a submerged horizontal plate. *Coastal Engineering Proceedings*, 1(22), 1990.

Komar, P. D. Environmental controls on littoral sand transport. *Coastal Engineering Proceedings*, 1(21), 1988.

Komar, P. D. *Beach processes and sedimentation*. Prentice-Hall, 1998.

Komar, P. D. and Inman, D. L. Longshore sand transport on beaches. *Journal of geophysical research*, 75(30):5914–5927, 1970.

Komen, G., Hasselmann, K., and Hasselmann, K. On the existence of a fully developed wind-sea spectrum. *Journal of physical oceanography*, 14(8):1271–1285, 1984.

Leatherman, S. Geomorphic and stratigraphic analysis of fire island, ny. *Marine Geology*, 126:143–159, 1985.

Lin, J.-G. An improvement of wave refraction-diffraction effect in swan. *Journal of Marine Science and Technology*, 21(2):198–208, 2013.

Madsen, O. S., Poon, Y.-K., and Graber, H. C. Spectral wave attenuation by bottom friction: theory. *Coastal Engineering Proceedings*, 1(21), 1988.

Madsen, P. A. and Sørensen, O. R. A new form of the boussinesq equations with improved linear dispersion characteristics. part 2. a slowly-varying bathymetry. *Coastal engineering*, 18(3):183–204, 1992.

Madsen, P. A., Murray, R., and Sørensen, O. R. A new form of the boussinesq equations with improved linear dispersion characteristics. *Coastal engineering*, 15 (4):371–388, 1991.

Masselink, G. Field investigation of wave propagation over a bar and the consequent generation of secondary waves. *Coastal Engineering*, 33(1):1–9, 1998.

McClennan, C. E. and McMaster, R. L. Probable holocene transgressive effects on the geomorphic features of the continental shelf off new jersey, united states. 1971.

McCormack, C. and Toscano, M. Origin of the barrier system of long island, new york. *Northeastern Geology*, 3:230–234, 1981.

Miles, J. W. On the generation of surface waves by shear flows. *Journal of Fluid Mechanics*, 3(02):185–204, 1957.

Mortlock, T., Goodwin, I., Turner, I., et al. Nearshore swan model sensitivities to measured and modelled offshore wave scenarios at an embayed beach compartment, nsw, australia. *Australian Journal of Civil Engineering*, 12(1):67, 2014.

Okamoto, T., Fortes, C., and Neves, M. Evaluation of nonlinear numerical model performance on the wave propagation over a bar-trough profile beach. *Journal of Coastal Research*, pages 1020–1024, 2009.

Ozasa, H. and Brampton, A. Mathematical modelling of beaches backed by seawalls. *Coastal Engineering*, 4:47–63, 1981.

Phillips, O. On the dynamics of unsteady gravity waves of finite amplitude part 1. the elementary interactions. *Journal of Fluid Mechanics*, 9(02):193–217, 1960.

Phillips, O. M. On the generation of waves by turbulent wind. *Journal of fluid mechanics*, 2(05):417–445, 1957.

Pierson, W., Neuman, G., and James, R. Observing and forecasting oceanwaves by means of wave spectra and statistics, us navy hydrographic office pub, 1955.

Pierson, W. J. The spectral ocean wave model (sowm), a northern hemisphere computer model for specifying and forecasting ocean wave spectra. Technical report, DTIC Document, 1982.

Resio, D. T. Full boltzmann discrete spectral wave model, implementation and nondimensional tests. Technical report, DTIC Document, 1993.

Resio, D. T., Pihl, J. H., Tracy, B. A., and Vincent, C. L. Nonlinear energy fluxes and the finite depth equilibrium range in wave spectra. *Journal of Geophysical Research: Oceans (1978–2012)*, 106(C4):6985–7000, 2001.

Roland, A. Development of {WWM II}: Spectral wave modelling on unstructured meshes. 2008.

Rosati, J. D., Gravens, M. B., and Smith, W. G. Regional sediment budget for fire island to montauk point, new york, usa. Technical report, DTIC Document, 1999.

Schaper, H. and Sielke, W. A numerical solution of boussinesq type wave equations. *Coastal Engineering Proceedings*, 1(19), 1984.

Schoonees, J. and Theron, A. Accuracy and applicability of the spm longshore transport formula. *Coastal Engineering Proceedings*, 1(24), 1994.

Schwab, W. C., Thieler, E. R., Allen, J. R., Foster, D. S., Swift, B. A., and Denny, J. F. Influence of inner-continental shelf geologic framework on the evolution and behavior of the barrier-island system between fire island inlet and shinnecock inlet, long island, new york. *Journal of Coastal Research*, pages 408–422, 2000.

Schwab, W. C., Baldwin, W. E., Hapke, C. J., Lentz, E. E., Gayes, P. T., Denny, J. F., List, J. H., and Warner, J. C. Geologic evidence for onshore sediment transport from the inner continental shelf: Fire island, new york. *Journal of Coastal Research*, 29(3):526–544, 2013.

Sénéchal, N., Bonneton, P., and Dupuis, H. Field experiment on secondary wave generation on a barred beach and the consequent evolution of energy dissipation on the beach face. *Coastal Engineering*, 46(3):233–247, 2002.

Smith, P. and Veatch, A. Atlantic submarine valleys of the united states and the congo submarine valley. 1939.

Sverdrup, H. U. and Munk, W. H. Wind, sea, and swell: theory of relations for forecasting. 1947.

Swift, D. J. and Moslow, T. F. Holocene transgression in south-central long island, new york: discussion. *Journal of Sedimentary Research*, 52(3), 1982.

Swift, D. J., Holliday, B., Avignone, N., and Shideler, G. Anatomy of a shore face ridge system, false cape, virginia. *Marine Geology*, 12(1):59–84, 1972.

Swift, D. J., Parker, G., Lanfredi, N. W., Perillo, G., and Figge, K. Shoreface-connected sand ridges on american and european shelves: a comparison. *Estuarine and Coastal Marine Science*, 7(3):257–273, 1978.

Thornton, E. B., Guza, R., et al. Transformation of wave height distribution. *J. Geophys. Res*, 88(10):5925–5938, 1983.

Tolman, H. L. The numerical model {WAVEWATCH}: a third generation model for hindcasting of wind waves on tides in shelf seas. 1989.

Tolman, H. L. Effects of numerics on the physics in a third-generation wind-wave model. *Journal of physical Oceanography*, 22(10):1095–1111, 1992.

Urien, C. M. and Ewing, M. Recent sediments and environment of southern brazil, uruguay, buenos aires, and rio negro continental shelf. In *The geology of continental margins*, pages 157–177. Springer, 1974.

Van de Meene, J., Boersma, J., and Terwindt, J. Sedimentary structures of combined flow deposits from the shoreface-connected ridges along the central dutch coast. *Marine Geology*, 131(3):151–175, 1996.

Van der Westhuysen, A. J. *Advances in the spectral modelling of wind waves in the nearshore*. TU Delft, Delft University of Technology, 2007.

Van der Westhuysen, A. J. and Tolman, T. Quasi-stationary wavewatch iii for the nearshore. In *Proc. 12th Int. Workshop on Wave Hindcasting and Forecasting, Hawaii*, 2011.

van Vledder, G. P. and Bottema, M. Improved modelling of nonlinear four-wave interactions in shallow water. In *COASTAL ENGINEERING CONFERENCE*, volume 1, pages 459–471. World Scientific, 2002.

Vis-Star, N. C., De Swart, H., and Calvete, D. Effect of wave-topography interactions on the formation of sand ridges on the shelf. *Journal of Geophysical Research: Oceans (1978–2012)*, 112(C6), 2007.

Warner, J. C., List, J. H., Schwab, W. C., Voulgaris, G., Armstrong, B., and Marshall, N. Inner-shelf circulation and sediment dynamics on a series of shoreface-connected ridges offshore of fire island, ny. *Ocean Dynamics*, 64(12):1767–1781, 2014.

Williams, S. J. Geomorphology, shallow subbottom structure, and sediments of the atlantic inner continental shelf off long island, new york. Technical report, DTIC Document, 1976.

Williams, S. J. and Meisburger, E. P. Sand sources for the transgressive barrier coast of long island, new york: evidence for landward transport of shelf sediments. In *Coastal Sediments' 87, Proceedings of a Specialty Conference on Advances in Understanding of Coastal Sediment Processes.*, volume 2, pages 1517–1532, 1987.

Witting, J. M. A unified model for the evolution nonlinear water waves. *Journal of Computational Physics*, 56(2):203–236, 1984.

Wolff, M. P. Evidence for onshore sand transfer along the south shore of long island, new york, and its implications against the bruun rule. *Northeastern Geology*, 4(1): 10–16, 1982.

Young, I. R. A shallow water spectral wave model. *Journal of Geophysical Research: Oceans (1978–2012)*, 93(C5):5113–5129, 1988.